PHYSICAL FOAMING BEHAVIOR AT THE INTERFACE OF POLYMER BLENDS

- Foaming Mechanism and its Application -

Pengjian Gong

2013

Contents

Chapter 1

GENERAL INTRODUCTION

1.1 Fundamentals of Foaming

1.1.1 Polymeric foams

Polymeric foams are the materials made of plastic matrix with pores inside. They consist of two phases: one is gas phase which forms the pores and the other is homopolymer or polymer blends or polymer composites which form the matrix.[1] By incorporating pores in polymer matrix, a number of advantages can be obtained in polymeric foams: low density, excellent strength/weight ratio, superior insulating abilities, energy absorbing performance, sound attenuation, etc. [2] The microscopic foam morphology is characterized by cell size, cell density, cell wall thickness, and open- and/or closed-cell structure; the macroscopic foam property is characterized by foam density, mechanical strength, thermal and electrical conductivity, etc.[3] According to the properties of forged polymeric foams, the corresponding applications can be versatile. For example, closed-cell foams have better effective insulation capabilities for either heat or electricity, while open-cell foams have a higher absorptive capacity for water and moisture, a higher permeability to gas and vapor, and a better ability to absorb and damp sound, thus they are more suitable for car seating, furniture, bedding and acoustical insulation.[4] As for the mechanical strength, it depends on the foam density, cell wall thickness, open- and/or closed-cell structure and intrinsic property of polymer matrix.[5] To

obtain flexible foams, low foam density, thin cell wall thickness, open-cell structure and soft polymer matrix are preferred, and vice verse. The major applications for flexible foams are carpet underlay, furniture, bedding, textile, gasketing, shoes, etc. and the rigid foams are mainly used in building and construction, appliances, transportation, floating, food and drink containers, etc.[6]

1.1.2 Microcellular foams

The common methods to induce bubbles in a matrix are volatilization of organic solvents, decomposition of additives, frothing of foams, mechanical mixing, etc., and they are suitable to prepare foams with a broad range of densities, relatively large cell size and low cell density.[7,8,4] Among them, the foam density is a key factor to determine the mechanical strength, while the cell size has considerable influence on thermal conductivity coefficience, both of which then determine the applications of those foams.[9,10] In order to generate bubbles in polymer matrix without losing too much mechanical strength, Professor Suh in Massachusetts Institute of Technology (MIT) introduced a new concept to prepare microcellular polymeric foams with cell size less than 10μm by phase separation, where supercritical fluids were utilized.[11,12] The reason is that supercritical fluid has the diffusivity as fast as gas and the density as large as liquid.[13] As a consequence, one can dissolve large amount of supercritical fluid in polymer matrix (large density) at relatively short time (fast diffusivity). It is commonly acknowledged that surface tension in a supercritical fluid is zero because there is no phase boundary between gas and liquid.[14] However, one should keep it in mind that the surface tension of polymer in a supercritical fluid is not zero and it is one of the most important parameters

which affects bubble nucleation.[15,16] Among the supercritical fluids, carbon dioxide (CO_2) and nitrogen (N_2) are the extensively used physical foaming agents to prepare microcellular polymeric foams; because the critical conditions of CO_2 and N_2 are just 304.1 K, 7.38 MPa and 126.2 K, 3.4 MPa, respectively.[17,18]

1.1.3 Foaming process

The preparation of microcellular polymeric foams consists of four stages: (1) dissolving physical foaming agent in polymer matrix; (2) inducing supersaturation and then bubble nucleation; (3) inducing bubble growth; (4) solidifying the polymer matrix. The schematic graph is shown in Figure 1.1. In stage 1, gas molecules can diffuse into the free volume of amorphous polymer matrix.[19] In the case of crystalline phase, the macromolecular chains are tightly packed in the form of lamella, gas molecules are blocked outside.[20] Along with dissolving more gas molecules, the free volume of polymer matrix increases and the corresponding glass transition temperature (T_g) decreases.[21] When the chemical potential of gas molecules in polymer matrix is equal to that in the supercritical fluids, the system reaches saturation state. After that, either temperature or pressure quenching can be applied to induce supersaturation, where the chemical potential of gas molecules in polymer matrix is larger than that in the environment and therefore those molecules tend to diffuse out from the polymer matrix.[22,23] If the free energy of bubble nucleation is compensated by the fluctuation of concentration, the critical bubble nuclei are generated and large amount of bubble nucleation occurs. Afterwards, most gas molecules prefer diffusing into the existed bubbles instead of inducing new bubble nuclei, and the pressure difference keeps increasing to expand the

bubbles. The work of volume expansion then compensates the work of surface tension and the work of biaxial elongational flow. Compared with bubble nucleation where surface tension is the major factor, the elasticity and viscosity of polymer matrix during foaming are the main factors to bubble growth. To induce large cell size, high foaming temperature (over T_g) is commonly applied to decrease the elasticity/viscosity of polymer matrix from 10^8 to 10^5 Pa. Along with gas molecules diffusing out, the reduced T_g is recovered, the elasticity/viscosity increases to 10^7 Pa and subsequently the polymeric foams are solidified. If the polymer matrix is still very soft after cells impinge on each other, the thinning behavior of biaxial elongational flow at the cell wall will finally lead to cell coalescence, which results in large cell size and low cell density.[24] It is also noted from Figure 1.1 that the polymeric foams prepared by phase separation usually have dense skin layers; because the CO_2 at the skin layer tends to diffuse out instead of nucleation.[25]

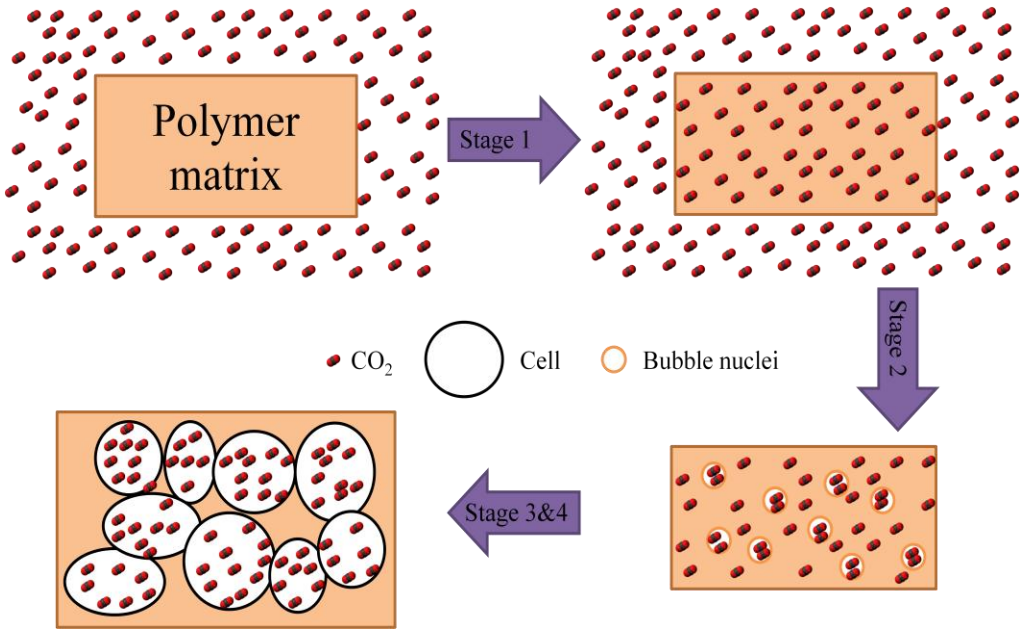

Figure 1.1 Schematic graph of four stages in the preparation of microcellular polymeric foams

1.1.4 Classical bubble nucleation theory

Figure 1.2 illustrates the change of phases in the process of bubble nucleation, which is induced by pressure quench. In stage 1 as indicated in Figure 1.1, the polymer-gas mixture is at **Point A**, where only one phase exists. The solubility of CO_2 or N_2 in polymer matrix is normally less than 20 wt%.[26,27] Therefore, **Point A** is always at the left side of this graph. When pressure quench is applied to induce supersaturation, **Point A** first moves to **Point B** at *Binodal* curve where polymer-gas mixture becomes unstable and bubble nucleation tends to occur. However, from the kinetic point of view, nucleation takes so long time that it actually hasn't occurred yet. By further decreasing the pressure to **Point C** at *Metastable* curve, supersaturation cannot maintain its state anymore and nucleation occurs drastically. No matter how fast the pressure decreases, **Point E** at *Spinodal* curve is inaccessible; because the supersaturation degree decreases simultaneously when bubble nucleation occurs. In the end, it shifts to **Point D** at *Metastable* curve again and then bubble nucleation ceases. In Figure 1.2, it has to be paid attention that *Binodal* and *Spinodal* curves have theoretical foundation while *Metastable* curve is empirical.[28]

The concept of critical nuclei radius, r^*, is the basis of Classical Bubble Nucleation Theory.[29] After crossing *Binodal* curve, the unstable characteristic of polymer-gas mixture leads to the fluctuation of gas concentration. However, the radii of most gas clusters are smaller than r^* and finally those clusters disappear. It can be seen from Figure 1.3 that the energy decreases with decreasing bubble radius when $r < r^*$. After crossing *Metastable* curve, a large number of gas clusters acquire enough energy to

overcome the barrier, ΔG^*, and then the energy decreases with increasing bubble radius. After crossing ΔG^*, bubble nucleation and bubble growth will occur spontaneously.

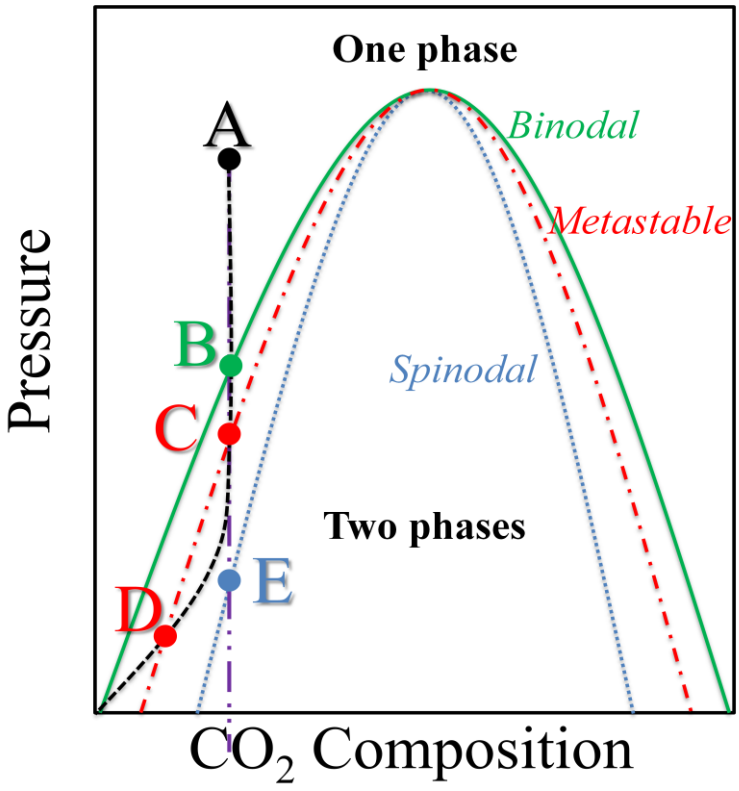

Figure 1.2 Phase diagram of polymer-gas system

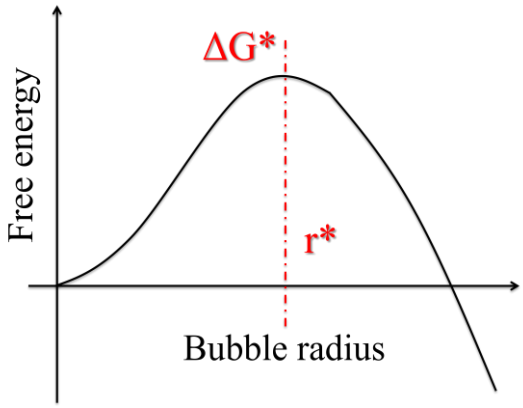

Figure 1.3 Energy required for the formation of a bubble as a function of bubble radius

In the case of homogeneous bubble nucleation, ΔG^* is expressed by the follow equation:[28]

$$\Delta G^* = \frac{16\pi\gamma^3}{3\Delta P^2} \quad (1)$$

γ is the surface tension between polymer and blowing agent, ΔP is the pressure difference between internal and external pressures.

The homogeneous bubble nucleation rate is then expressed by: [28]

$$J = C\exp[\frac{-\Delta G^*}{kT}] = C\exp[\frac{-16\pi\gamma^3}{3kT\Delta P^2}] \quad (2)$$

where C is the preexponential factor and T is the environmental temperature.

As for heterogeneous bubble nucleation, ΔG^* is expressed by the follow equations: [28]

$$\Delta G^* = \frac{16\pi\gamma_A^3 F}{3\Delta P^2} \quad (3)$$

where

$$F = \frac{1}{4\gamma_A^3}\left[\gamma_A^3\left(2-3m_A+m_A^3\right)+\gamma_B^3\left(2-3m_B+m_B^3\right)\right] \quad (4)$$

$$m_A = \cos\theta = \frac{\gamma_A^2+\gamma_{AB}^2-\gamma_B^2}{2\gamma_A\gamma_{AB}} \quad (5)$$

$$m_B = \cos\varphi = \frac{\gamma_B^2+\gamma_{AB}^2-\gamma_A^2}{2\gamma_B\gamma_{AB}} \quad (6)$$

γ_A, γ_B and γ_{AB} represent the surface tension between polymer A and blowing agent, polymer B and blowing agent, and the interfacial tension between polymer A and polymer B, respectively. θ and φ are the angles of γ_A with γ_{AB} and γ_B with γ_{AB}, respectively.

The heterogeneous bubble nucleation rate is then expressed by: [28]

$$J = C' \exp\left[\frac{-16\pi\gamma_A^3 F}{3kT\Delta P^2}\right] \quad (7)$$

where *C'* is the preexponential factor.

1.2 Fundamentals of Polymer Blends

1.2.1 Phase morphology

Polymer blending is to mix two or more existing polymers physically. Comparing with polymerization of new polymers, blending is a cost-effective way to provide new materials with excellent mechanical properties from each component.[30] When a polymer blend is miscible, the following thermodynamic rules have to be complied:[31]

$$\Delta G_{mix} = \Delta H_{mix} - T\Delta S_{mix} < 0 \tag{8}$$

and

$$\left(\frac{\partial^2 \Delta G_{mix}}{\partial \phi_i^2} \right)_{T,P} > 0 \tag{9}$$

where ΔG_{mix}, ΔH_{mix} and ΔS_{mix} are the Gibbs energy, enthalpy and entropy of the blend system, respectively. ϕ_i is the volume fraction of component *i*.

By applying Flory-Huggins relationship for ΔG_{mix}, it leads to the condition of the stability:[31]

$$\frac{1}{N_1\phi_1} + \frac{1}{N_2\phi_2} - 2\chi_{12} \geq 0 \tag{10}$$

where N_1 and N_2 are the numbers of segments of polymers 1 and 2, respectively. χ_{12} is the interaction parameter between polymers 1 and 2. In the case of polymers with large molecular weight, N_1 and N_2 are very large and hence the miscibility is directly controlled by the enthalpy of mixing, namely the interaction parameter of χ_{12}.

For most polymer pairs with weak interactions, the positive value of χ_{12} indicates a very poor miscibility.[32] Compared with the group of immiscible polymer blends, the

group of miscible polymer blends is quite small.[33,34] Therefore, heterogeneous polymer blends can be obtained with sea-island (major component is sea, i.e., matrix, and minor component is island, i.e., domain), or co-continuous phase morphology (both components penetrate into the other phase to form a network structure) as shown in Figure 1.4.[35]

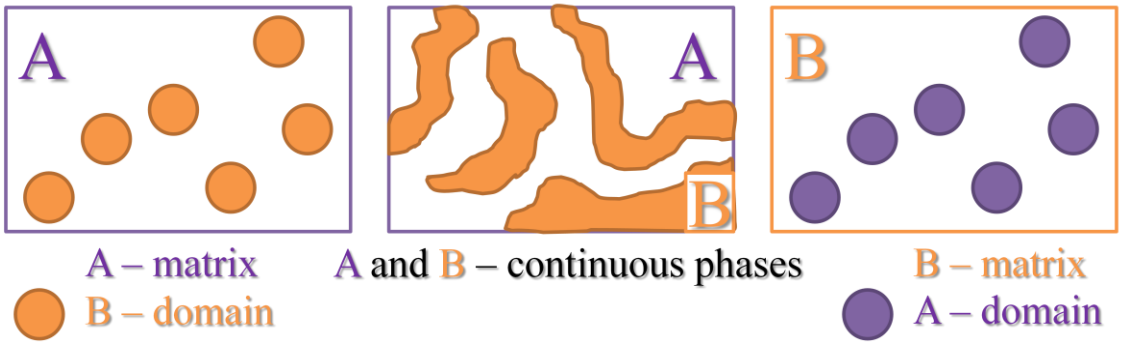

Figure 1.4 Phase morphology of polymer blends

Unlike liquid-liquid system, the relaxation behavior of macromolecular chains determines that phase morphology of polymer-polymer system is thermodynamic dependent. As a consequence, the processing method has a great influence on phase structure. There are four methods which are frequently used for the preparation of polymer blends: (1) melt mixing, (2) solution blending, (3) latex mixing and (4) interpenetrating polymer networks (IPN).[36,37,38,39] Among them, melt mixing is highly commercialized because any kinds of polymer blends can be prepared by single- or twin-screw extruders. However, the other three methods all have their own disadvantages.[31] For instance, the blend components have to either be dissolved in the same solvent (solution blending), have latex forms (latex mixing), or one blend component has to be swollen by the monomer of the other component (IPN). When melt mixing is applied to

prepare polymer blends with a sea-island morphology, the dispersion of domain is a function of capillary number, *Ca*, and viscosity ratio, λ:[40]

$$Ca = \frac{\eta_m \dot{\gamma} d}{2\gamma_{12}} \tag{11}$$

$$\lambda = \frac{\eta_d}{\eta_m} \tag{12}$$

where η_m and η_d are the viscosities of matrix and domains, respectively. $\dot{\gamma}$ is the shear rate, *d* is the diameter of the domain, and γ_{12} is the interfacial tension between matrix *1* and domain *2*. *Ca* represents the competition between the flow stresses, which deform and break domains, and the interfacial tension, which resists the deformation. Furthermore, when λ is close to one, the droplet deformation and breakup is most promoted. As a result, small interfacial tension, large matrix viscosity and λ as close as 1, are favored to have better domain dispersion. Better dispersion in this thesis means that domain size is more uniform and smaller and domains are more evenly distributed in the continuous phase.

1.2.2 Reactive blending

For incompatible polymer blends, the interfacial tension is very large and the domain dispersion is very bad. With large domain size and weak interfacial adhesion, the obtained polymer blends fail to possess good mechanical properties and are ready to fracture. In order to improve the mechanical properties, compatibilizers, which have excellent affinities with both phases, are commonly introduced to selectively locate at the interface between domain and matrix, as shown in Figure 1.5.[41] By covering domain with copolymer, it suppressed domain aggregation and increased interfacial adhesion.[42]

However, the polymerization process for a copolymer with two distinct segments is difficult and the amount required for compatibilization is relatively large, since only a small fraction of added copolymer can locate at the interface. Consequently, reactive blending is a convenient method to directly generate copolymers at the interface.[43]

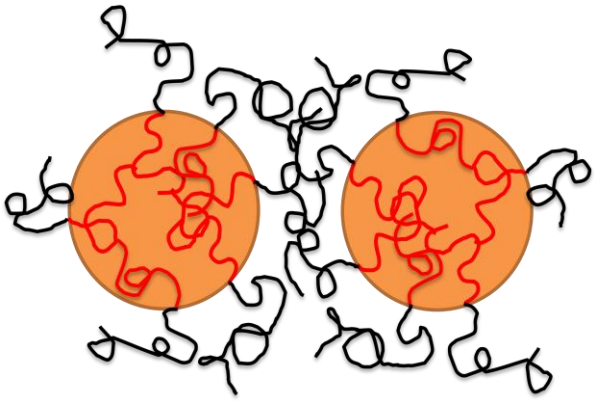

Figure 1.5 Schematic view of copolymer at the interface

To induce reaction between two polymers in the process of melt mixing, functional groups have to be incorporated into molecular chains. Thus, the polymers capable of reactive blending can be classified into eight categories. Each category has one type of functional group, including maleic anhydride, carboxylic acid, groups capable of interchange reactions, primary and secondary amines, hydroxyl groups, heterocyclic groups, groups capable of ionic interactions, etc.[40] With those versatile functional groups, there are mainly four reaction types: addition and/or substitution, interchange reaction, ring-opening reaction, and ionic bonding. When the side chain has functional group, graft copolymer is generated. Addition or ionic bonding to the backbone also produces graft copolymer. Nevertheless, block copolymers are formed by substitution and interchange reaction at the backbone, addition at the chain ends, or ring-opening reaction. The

generated graft or block copolymers subsequently facilitate the miscibility at the interface of polymer blends by decreasing interfacial tension, increasing interfacial adhesion, hindering domain aggregation and promoting domain dispersion.

In order to clarify the relationship between interfacial properties and blend morphology, the binary polymer-polymer interaction energy, *B*, is introduced to replace the Flory-Huggins parameter, χ_{12}. The Gibbs free energy for mixing a unit volume of monodisperse polymers *A* and *B*, Δg_{mix} is then expressed by the following equation:[44]

$$\Delta g_{mix} = B\phi_A\phi_B + RT\left[\frac{\rho_A\phi_A \ln\phi_A}{M_A} + \frac{\rho_B\phi_B \ln\phi_B}{M_B}\right] \qquad (13)$$

where *R* is the gas constant; *T* is the absolute temperature; ρ_i, ϕ_i and M_i are the density, volume fraction and molecular weight of component *i*, respectively. In this equation, *B* is an excess free energy term in which the heat of mixing plus other noncombinatorial effects are included.

The Flory-Huggins parameter, χ_{12}, is then expressed by:[44]

$$\chi_{12} = \frac{BV_{ref}}{RT} \qquad (14)$$

where V_{ref} is a reference volume that is usually taken as the molar volume of one of the repeat units in the system.

When the third derivative of Δg_{mix} with respect to the composition equals to 0, that is the critical conditions of temperature and blend composition, the balance at the phase boundary between energetics and entropic contributions to mixing is achieved. $B_{critical}$ is then described by the following equation: [44]

$$B_{critical} = \frac{RT}{2}\left(\sqrt{\frac{\rho_A}{\left(\bar{M}_w\right)_A}} + \sqrt{\frac{\rho_B}{\left(\bar{M}_w\right)_B}}\right)^2 \tag{15}$$

where $\left(\bar{M}_w\right)_i$ is the weight average molecular weight. For polymers, $\left(\bar{M}_w\right)_i$ is usually very large, and hence $B_{critical}$ is positive and quite close to 0. From equation (15), it can be seen that only the polymer blends with an energetic contribution (B) less than $B_{critical}$ are miscible.

The interfacial adhesion is related with the thickness of interface, δ, which is expressed by the following equation: [44]

$$\delta = \sqrt{\frac{2RT}{B}\left(\beta_A^2 + \beta_B^2\right)} \tag{16}$$

and the interfacial tension, γ_{12}, is then expressed by the following equation: [44]

$$\gamma_{12} = \sqrt{\frac{RTB}{2}}\left(\beta_A + \beta_B\right)\left[1 + \frac{1}{3}\frac{\left(\beta_A - \beta_B\right)^2}{\left(\beta_A + \beta_B\right)^2}\right] \tag{17}$$

where β_i is related to the dimension of the polymer coil as follows:

$$\beta_i = \sqrt{\frac{\rho_i}{6}}\left(\left\langle \gamma_i^2 \right\rangle / M_i\right)^{1/2} \tag{18}$$

where $\left\langle \gamma_i^2 \right\rangle$ is the mean-square unperturbed end-to-end chain distance and M_i is the molecular weight.

From Eqs. (16) and (17), it is noted that both interfacial thickness and interfacial tension are functions of polymer-polymer interaction energy. When the interfacial properties are modified either by adding copolymers or reactive blending, it would decrease the polymer-polymer interaction energy. Therefore the interfacial adhesion is

strengthened by larger interfacial thickness, while the domain dispersion is facilitated by smaller interfacial tension.

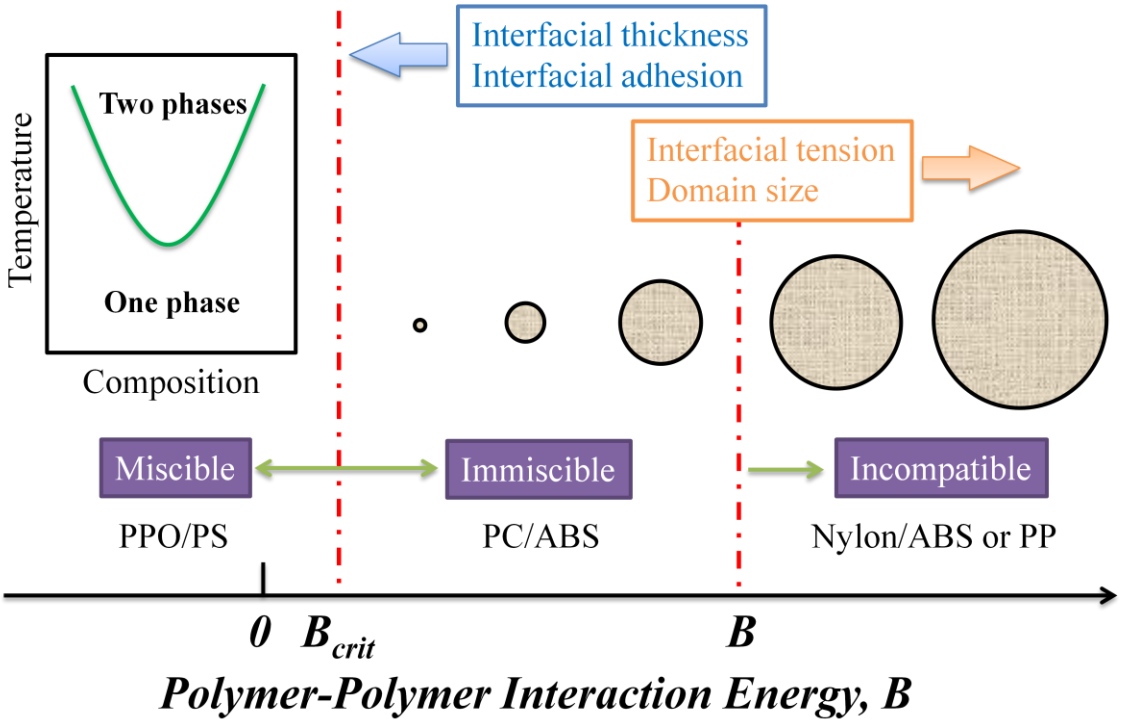

Figure 1.6 Illustration of the role of polymer-polymer interaction energy on blend structure and properties.[44]

The schematic graph which illustrates the role of polymer-polymer interaction energy on blend structure and properties is shown in Figure 1.6. For instance, the interfacial tensions of Nylon/ Acrylonitrile butadiene styrene (ABS) or Polypropylene (PP) blends are very large, which lead to large domain size. The mechanical properties are greatly deteriorated due to the bad interfacial adhesion and polymer blend of this kind is considered as incompatible.[45,46] To have better performance, compatibilizer is required to decrease polymer-polymer interaction energy and hence to increase the interfacial

thickness. In the case of Polycarbonate (PC)/ABS blend, the interfacial tension is relatively small compared with Nylon/ABS blend and hence PC/ABS blend has better dispersed domains and mechanical strength. [47, 48] However, the polymer-polymer interaction energy of PC/ABS blend is still much larger than $B_{critical}$, which leads to immiscible blend. As for Poly(2,6-dimethyl-1,4-phenylene oxide) (PPO)/Polystyrene (PS) blend, the polymer-polymer interaction energy and interfacial tension are 0, the interfacial thickness is infinite, the phase boundary disappears and consequently the blend is miscible.[49]

1.2.3 Interfacial properties

From the macroscopic point of view, the definition of surface tension is the energy required to create a unit area of surface.[50] The schematic graph is shown in Figure 1.7. In the case of homogeneous bulk phase, two surfaces are created when the bulk phase is cleaved and the energy (W) which is required to cleave the bulk phase is twice of the surface tension (γ_A). As for heterogeneous bulk phase, two surfaces have distinct surface tensions (γ_A and γ_B) after the interface is cleaved. Moreover, the energy (W_{AB}), which is required to cleave the interface, is smaller than the sum of surface tensions (γ_A + γ_B). This difference is then defined as the intrinsic energy stored in an interface, i.e., interfacial tension (γ_{AB}). Consequently, larger surface tension requires larger cleavage energy. In contrast, polymer blends with larger interfacial tension require less energy to cleave the interface.[51]

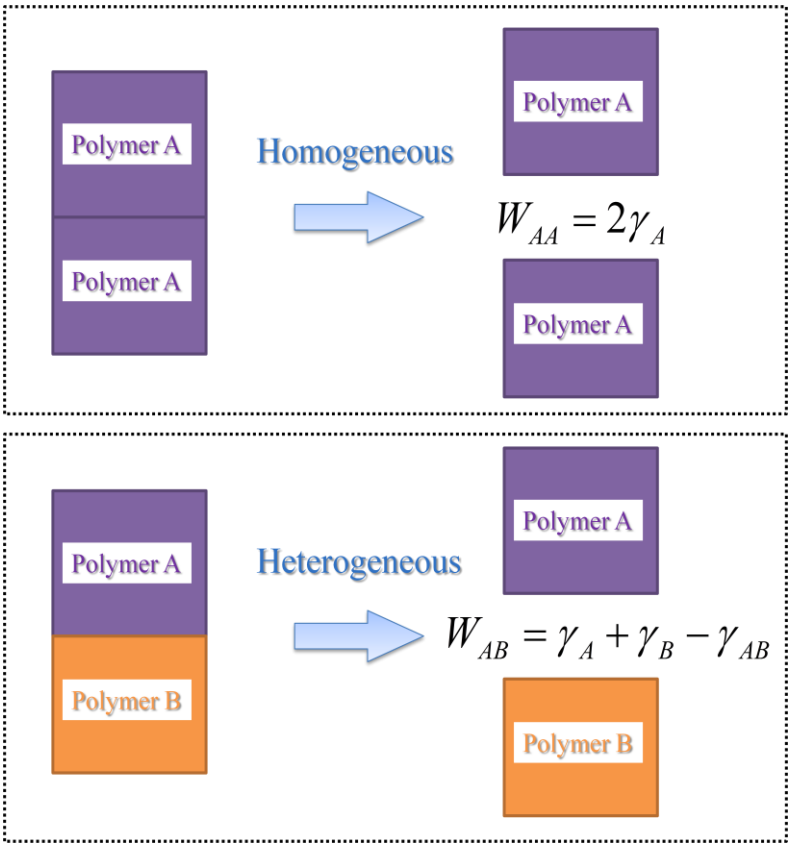

Figure 1.7 Schematic graph of cleavage of bulk polymer and interface

From the microscopic point of view, the force field in a homogeneous bulk phase is isotropic and therefore no net energy is expended in reversibly transporting the matter within a bulk. However, the force field in the interfacial (surface) zone is heterogeneous, having a gradient perpendicular to the interfacial (surface) boundary and hence a net energy is required to create an interface (surface) by transporting the matter from the bulk phase to the interfacial (surface) zone. The reversible work required to create a unit interfacial (surface) area is subsequently the interfacial (surface) tension.[52] When we go through one bulk phase to the other, the composition gradient region, i.e., interface, has certain thickness, normally less than 0.1 μm.[53,54] It can be seen from Figure 1.8 that an incompatible polymer blend has a very clear interface; because the composition gradient

is very sharp and therefore the interfacial thickness is very small. Due to the thin interface, the incompatible polymer blend has weak interfacial adhesion and bad mechanical performance, and copolymers have to be introduced to increase the thickness of interface.[55] It is also noted from Figure 1.8 that the slop of composition gradient is low and the interface is blurred in the case of compatible but immiscible polymer blend.

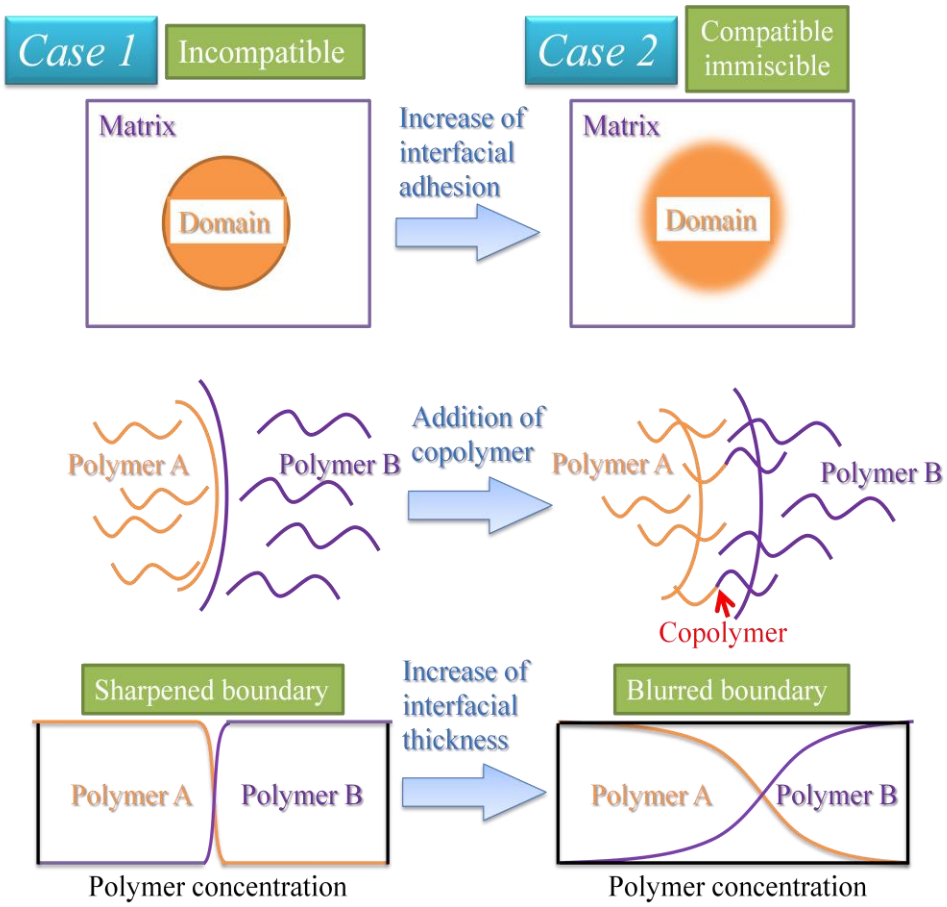

Figure 1.8 Schematic graphs of interfacial properties (interfacial adhesion, interfacial thickness) with the addition of copolymers. Case 1 is incompatible polymer blend and Case 2 is compatible and immiscible polymer blend.

1.3 Foaming behavior of Polymer Blends

1.3.1 Relationship between blend morphology and foam morphology

It is commonly acknowledged that foam morphologies like foam density, cell size, cell density, cell wall thickness, open- and/or closed-cell structure, bimodal-cell structure, are basically related with bubble nucleation, bubble growth and cell coalescence. Each foaming system has its distinct foaming behavior and hence leads to its specific foam morphology. As described above in the section of 1.1.1, the foam applications are determined by the foam morphologies. In order to tailor the foam morphologies, the addition of inorganic fillers or second polymer phases is frequently applied to control the bubble nucleation, bubble growth or cell coalescence.[56,57,58,59] Compared with inorganic fillers, polymer blends are superior due to their versatile blend morphologies and corresponding blend properties.[60] Especially immiscible polymer blends, the blend properties, like domain size, interfacial area, interfacial tension, interfacial adhesion, gas solubility, gas diffusivity, rheology, crystallization and glass transition, can be adjusted and modified to produce desired polymeric foams. The overall strategic flow from blend properties, to foaming process and finally to foam applications is shown in Figure 1.9. According to this strategic flow, one can easily understand the relationship of blend morphology and foam morphology.

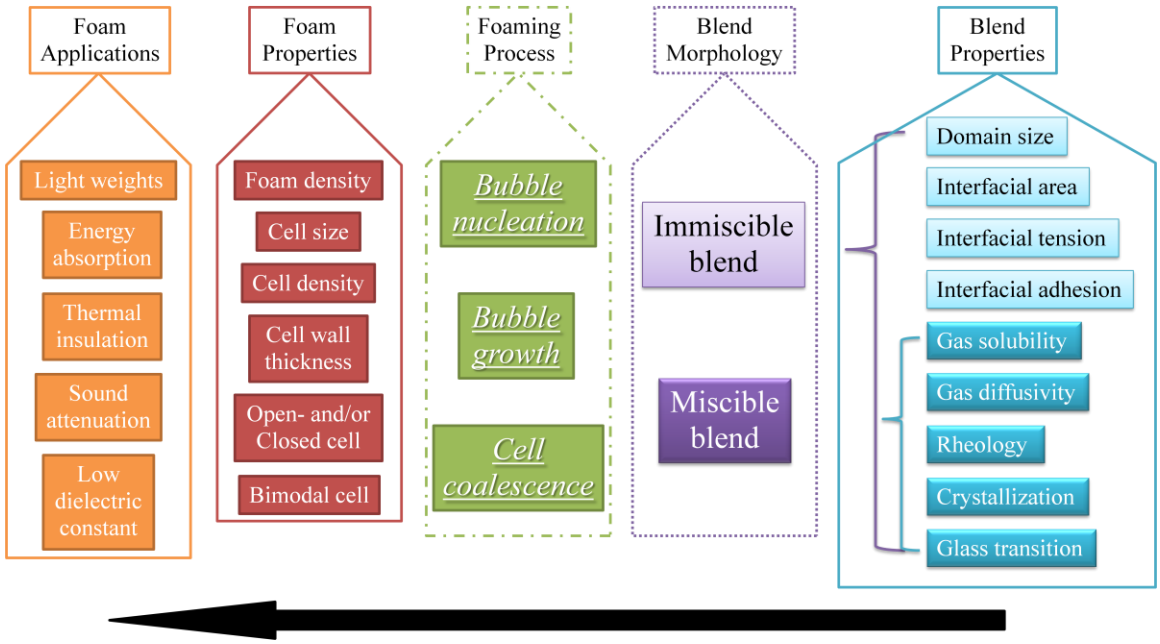

Figure 1.9 Strategic flow from blend properties to foam applications for exploiting the polymer blend foams

1.3.2 Bubble nucleation in polymer blends

From Eqs. (2) and (7), it is noticed that exponential term of heterogeneous bubble nucleation rate is much smaller than that of homogeneous bubble nucleation rate. Therefore, the energy required for heterogeneous bubble nucleation is lower than homogeneous bubble nucleation, and correspondingly higher cell density is induced by heterogeneous bubble nucleation. Blending second polymer phase with one polymer matrix will generate interfacial area where large numbers of active sites are ready for heterogeneous bubble nucleation. Doroudiani and Huang, respectively, reported the increased cell density of PP/ Polyethylene (PE) blend foams in which PP was the matrix and PE was the domain.[61,62] Heterogeneous bubble nucleation was then induced at the interface between PP matrix and PE domains. Instead of using PP as matrix, Sharudin et

al. considered using PP as a bubble nucleating agent and investigated the effect of the interface between polymers on bubble nucleation using PP/PS and PP/ Poly(methyl methacrylate) (PMMA) blends as example systems.[63] They conducted visual observation experiments, which revealed that the dispersed PP domains acted as bubble nucleating agents due to the incompatible interface between PP and PS as well as PMMA. During foam extrusion process of pure low-density Polyethylene (LDPE), microcellular foams could not be produced due to the high activation energy for bubble nucleation. Therefore, Park et al. blended PS with LDPE to induce heterogeneous bubble nucleation, which increased the cell density.[64]

When bubble nucleation is capable to occur both in domain and matrix, bimodal cellular structure can be prepared by inducing first bubble nucleation at one phase and then second bubble nucleation at the other phase. Kohlhoff et al. prepared PMMA/PS blend which contained highly dispersed, cross-linked PMMA-rich domains in the PS matrix by in-situ polymerization.[65] After foaming by CO_2, the time lag between first and second bubble nucleation led to bimodal cellular structure of 10-30 μm cells surrounding 200-400 μm cells.

Apart from immiscible polymer blends, appropriate miscible polymer blends can also induce high cell density by increasing the gas solubility. Krause et al. reported the open nanoporous morphologies of Polysulfone (PSU)/Polyimide (PI) blend foams.[66] The solubility of CO_2 in homogeneous PSU/PI blend was a function of PI weigh percentage in the blend. When CO_2 solubility exceeded a threshold value by tuning the blend composition, cell density increased abruptly and cell size decreased from micrometer to sub-micrometer. However, most miscible polymer blends have little effects on bubble

nucleation even though CO_2 solubility is slightly increased. One can have a glance at the equation (2), the preexponential term will be increased by increasing gas solubility. Compared with an increase of 10% in exponential term, an increase of over 100% in preexponential term is necessary to have same degree of effect on bubble nucleation rate.[28] As a result, immiscible polymer blends with large interfacial area, i.e., large amount of active sites, are favored to induce high cell density.

1.3.3 Bubble growth in polymer blends

After bubble nucleation, the gases in bubbles have to overcome the viscoelastic properties of polymer matrix and then expand the bubbles to larger sizes. The modification of viscoelastic properties of matrix, or viscoelastic contrast between domain and matrix, can effectively constrain bubble growth. When Styrene-ethylene/Butylene-styrene (SEBS) was foamed by CO_2, low elasticity of SEBS resulted in large cell size and fast CO_2 diffusivity subsequently led to foam shrinkage. Sharudin et al. then blended SEBS with thermoplastic polymers, like PS and PP, to slow down CO_2 diffusion and stabilize the cells.[67] So long as the foaming temperature was lower than the T_g of PS or the melting temperature (T_m) of PP, fine cell properties were obtained with optimum elasticity.

Furthermore, the strategy of constraining bubble growth is employed to prepare polymer blend foams with nanometer cells. Otsuka et al. prepared PMMA/PS blends, which contained dispersed nanoscale PMMA domains, by polymerizing Methyl methacrylate (MMA) monomers in a PS matrix.[68] When CO_2 foaming was conducted at fast depressurization rate and low foaming temperature, nanocell blend foam was

obtained. In this process, the dispersed nanoscale PMMA domains were in rubbery state due to large CO_2 solubility while PS matrix was still in glassy state. The elasticity of PS matrix was 10^8 Pa, almost 10^3 times as large as the elasticity of PMMA domains, 10^5 Pa. After bubble nucleation in PMMA domains, bubble growth was then greatly suppressed by the hard PS matrix. If foaming temperature was close to the T_g of PS matrix, The elasticity of PS matrix was not enough to constrain bubble growth and consequently microcell blend foams were obtained.

Besides nanocell blend foams, the characteristic of hard/soft inhomogeneity in the matrix attributes to cell opening as well.[69] The hard regions still retained the overall cellular structure to avoid cell coalescence.[70] Cell opening can either be initiated by tearing the soft regions or induced by debonding hard region from soft region. Lee et al. incorporated secondary blowing agent to further plasticize soft regions so that the stiffness contrast between hard and soft regions in the polymer matrix was intensified.[71] Kohlhoff et al. prepared Polylactic acid (PLA)-based blends where interpenetrating polymer networks supported the overall cellular structure and monomers acted as cell opening agents.[72] This strategy is suitable to produce open-cell foams with large open-cell contents and large cell size. Both these two strategies of bubble growth suppression (nanocells etc.) and interface separation (open cells etc.) utilize the viscoelastic contrast between domain and matrix, but the location of bubble nucleation whether in domain or in matrix distinguishes which mechanism is dominant.

As for miscible polymer blends, the inhibition of crystallization behavior is one advantage to prepare blend foams with uniform cells. The foaming morphology of semi-crystalline polymer is usually not uniform and the range of foaming temperature is very

narrow, sometimes only 5°C. Below T_m, the existence of crystalline lamellas decreases CO_2 solubility and suppresses bubble growth. Over T_m, the elasticity of polymer is too low to control bubble growth. Therefore, the inhibition of crystallization behavior is preferred by blending two miscible polymer components. It is the different chemical structure between two polymer components that attributes to amorphous polymer blend. Poly(vinylidene fluoride) (PVDF) was originally highly crystalline polymer. Since PMMA was miscible with PVDF, the obtained PVDF/PMMA blend was then amorphous. Siripurapu et al. reported that PVDF/PMMA blend foam with uniform cell sizes and high cell density was subsequently generated by increasing CO_2 solubility and suppressing crystallization.[73]

1.3.4 Cell coalescence in polymer blends

The biaxial elongational flow in the process of bubble growth thins the cell wall. When cell wall thickness is not large enough to maintain the cell structure, cell coalescence occurs. Consequently, cell density is decreased and cell size is increased. In order to stabilize the cells during bubble growth, Li et al. studied the dynamics of bubble growth by numerical simulation.[74] It was found that stability during bubble growth was facilitated by moderate strain hardening characteristics and elastic properties of the polymers. Then, Liao et al. prepared miscible Poly(3-hydroxybutyrate-co-3-hydroxyvalerate) (PHBV)/Cellulose acetate butyrate (CAB) blends with high melt viscosity. Consequently, foams with more uniform cell size distribution and better homogeneity of cellular morphology were obtained.[75] Besides increasing the overall viscosity of the polymer matrix, strain hardening behavior only imposes an effect on the

cell wall. Spitael et al. added long-chain branched PP to linear PP to induce strain hardening behavior in the process of bubble growth.[76] This resulted in abrupt rise of cell wall viscosity and then suppressed cell coalescence.

1.4 Objective of This Work

Nowadays, large amount of researches have been done related with foaming behavior of polymer blends. Researchers have made full use of miscellaneous blend morphologies to produce desired polymer blend foams. However, one can notice from Figure 1.9 that the interfacial properties are key factors to control the blend morphology. In order to increase the dispersibility of the minor phase, i.e., more interfacial area available for heterogeneous bubble nucleation, compatibilizers are often used in polymer blends to modify the interfacial properties. With decreasing interfacial tension, the effectiveness of heterogeneous bubble nucleation may be affected as well. From the view point of classical bubble nucleation theory, large interfacial tension is favored to induce heterogeneous bubble nucleation. If this is true, there will be an optimum interfacial tension, which is small enough to increase interfacial area, but is still large enough to decrease the energy required for bubble nucleation. Actually several authors have reported the foaming behavior of polymer blends with modified interface and their results are contradictive: large interfacial area sometimes induces high cell density, but sometimes has no effect.[77,78,79,80] The contradictive result implies that further study is required to understand the complicate effect of interfacial tension on bubble nucleation. At the same time, in the process of bubble growth, only surface tension and elasticity of polymer matrix are considered to be responsible for bubble growth. However, one can notice from Figure 1.7 that the energy required to separate the interface at the initial stage of bubble growth is a combination of surface and interfacial tension. Moreover, it can be seen from Figure 1.8 that interface between two polymer phases is strengthened by the diffusion of molecular chains and has certain thickness. This feature of interface implies

that further study is required as well concerning the effect of interfacial adhesion on bubble growth.

In chapter 2, two amorphous polymers, PMMA and Bisphenol A polycarbonate (PC) were selected to prepare compatible and immiscible PMMA/PC blends. The interfacial properties between PC domains and PMMA matrix can be easily tailored by reactive blending, during which graft copolymer was generated. The blend properties, like domain size and domain density, were subsequently controlled by the interfacial tension. In the end, the number of bubbles per unit interfacial area and the number of bubbles per unit number of domains were evaluated to clarify the effect of interfacial tension on bubble nucleation.

In chapter 3, semicrystalline Polyethylene terephthalate (PET) was used as domain and PC was used as matrix in PET/PC blends. The interfacial properties between PET domains and PC matrix can be easily tailored by transesterification reaction, during which block copolymer was generated. Due to the effectiveness of block copolymer, the immiscible PET/PC blends became partially and eventually totally miscible by the transesterification reaction. In the end, the surface morphology of PET domains after foaming and the cell wall morphology were observed to clarify the effect of interfacial adhesion on bubble growth.

The ultimate objective of polymer blend foaming is to produce desired polymeric foams with distinct foam morphology by controlling bubble nucleation and bubble growth at the interface. With the knowledge obtained from chapters 2 and 3, functional PET/PC blend foams were discussed in the following chapters 4 and 5. In chapter 4, the open-cell characteristic of PC foams was illustrated in advance. Biaxial elongational flow

in the process of bubble growth led to dilatational deformation and subsequently nanoporous structure appeared on the cell wall. When the cell wall thickness was smaller than a certain value, open-cell PC foams with 100% open-cell ratio would be achieved. However, the obtained open-cell PC foams had large cell size and low cell density. In chapter 5, heterogeneous bubble nucleation was then employed by foaming PET/PC blends to increase the cell density. Due to the nanoporous structure on the cell wall, cell coalescence occurred and this behavior greatly reduced the cell density. Consequently, interfacial adhesion was utilized to generate fibril structure so as to enhance bubble nucleation. In the end, open-cell PET/PC blend foams with small cell size, large cell density and large open-cell ratio were obtained.

Finally in chapter 6, all results in this dissertation are summarized.

1.5 References

1 Lee, S.T.; Ramesh, N.S. *Polymeric Foams: Mechanisms and Materials*. **2004**, CRC Press.

2 Lee, S.T.; Park, C.B.; Ramesh, N.S. *Polymeric Foams: Science and Technology*. **2007**, CRC Press.

3 Lee, S.T. *Foam Extrusion: Principles and Practice*. **2000**, CRC Press.

4 Klempner, D.; Frisch, K.C. *Handbook of Polymeric Foams and Foam Technology*. **1991**, Oxford University Press.

5 Meinecke, E.A.; Clark, R.C. *Mechanical Properties of Polymeric Foams*. **1973**, Technomic Pub. Co.

6 Eaves, D. *Handbook of Polymer Foams*. **2004**, Rapra Technology Limited.

7 Tuladhar, T.R.; Mackley, M.R. *Chem. Eng. Sci.* **2004**, 59, 5997-6014.

8 Han, C.; Kim, Y.; Malhotra, K.D. *J. Appl. Polym. Sci.* **1976**, 20, 1583-1595.

9 Kumar, V.; VanderWel, M.; Weller, J.; Seeler, K.A. *J. Eng. Mater. Technol.* **1994**, 116, 439-445.

10 Almanza, O.A.; Rodriguez-Perez, M.A.; De Saja, J.A. *J. Polym. Sci., Part B: Polym. Phys.* **2000**, 38, 993-1004.

11 Mooney, D.J.; Baldwin, D.F.; Suh, N.P.; Vacanti, J.P.; Langer, R. *Biomaterials*. **1996**, 17, 1417-1422.

12 Baldwin, D.F.; Shimbo, M.; Suh, N.P. *J. Eng. Mater. Technol.* **1995**, 117, 62-74.

13 Kiran, E.; Debenedetti, P.G.; Peters, C.J. *Supercritical Fluids: Fundamentals and Applications*. **1994**, Kluwer Academic Publishers.

14 Russick, E.M.; Adkins, C.L.J.; Dyck, C.W. *ACS Symposium Series*. **1997**, 670, 255-269.

15 Tsivintzelis, I.; Angelopoulou, A.G.; Panayiotou, C. *Polymer*. **2007**, 48, 5928-5939.

16 Park, H.; Park, C.B.; Tzoganakis, C.; Tan, K.H.; Chen, P. *Ind. Eng. Chem. Res.* **2006**, 45, 1650-1658.

17 Di Maio, E.; Mensitieri, G.; Iannace, S.; Nicolais, L.; Li, W.; Flumerfelt, R.W. *Polym. Eng. Sci.* **2005**, 45, 432-441.

18 Belinsky, M.R. *Supercritical Fluids*. **2010**, Nova Science Publishers.

19 Bonavoglia, B.; Storti, G.; Morbidelli, M.; Rajendran, A.; Mazzotti, M. *J. Polym. Sci., Part B: Polym. Phys.* **2006**, 44, 1531-1546.

20 Bonavoglia, B.; Storti, G.; Morbidelli, M. *Ind. Eng. Chem. Res.* **2006**, 45, 1183-1200.

21 Bos, A.; Punt, I.G.M.; Wessling, M.; Strathmann, H. *J. Membr. Sci.* **1999**, 155, 67-78.

22 Sun, X.; Liu, H.; Li, G.; Liao, X.; He, J. *J. Appl. Polym. Sci.* **2004**, 93, 163-171.

23 Park, C.B.; Baldwin, D.F.; Suh, N.P. *Polym. Eng. Sci.* **1995**, 35, 432-440.

24 Park, C.B.; Behravesh, A.H.; Venter, R.D. *Polym. Eng. Sci.* **1998**, 38, 1812-1823.

25 Solorzano, E.; Antunes, M.; Saiz-Arroyo, C.; Rodriguez-Perez, M.A.; Velasco, J.I.; de Saja, J.A. *J. Appl. Polym. Sci.* **2012**, 125, 1059-1067.

26 Li, G.; Li, H.; Turng, L.S.; Gong, S.; Zhang, C. *Fluid Phase Equilib.* **2006**, 246, 158-166.

27 Areerat, S.; Funami, E.; Hayata, Y.; Nakagawa, D.; Ohshima, M. *Polym. Eng. Sci.* **2004**, 44, 1915-1924.

28 Hartland, S. *Surface and Interfacial Tension: Measurement, Theory, and Applications*. **2004**, Marcel Dekker, Inc.

29 Han, J.H.; Han, C.D. *J. Polym. Sci., Part B: Polym. Phys.* **1990**, 28, 743-761.

30 Utracki, L.A. *Polymer Blends Handbook*. **2002**, Kluwer Academic Publishers.

31 Mark, H.F. *Encyclopedia of Polymer Science and Technology*. **2005**, John Wiley & Sons, Inc.

32 Lee, J.H.; Ruegg, M.L.; Balsara, N.P.; Zhu, Y.; Gido, S.P.; Krishnamoorti, R.; Kim, M. *Macromolecules.* **2003**, 36, 6357-6458.

33 Lutz, T.R.; He, Y.; Ediger, M.D.; Cao, H.; Lin, G.; Jones, A.A. *Macromolecules.* **2003**, 36, 1724-1730.

34 Pathak, J.A.; Colby, R.H.; Kamath, S.Y.; Kumar, S.K.; Stadler, R. *Macromolecules.* **1998**, 31, 8988-8997.

35 Lee, J.K.; Han, C.D. *Polymer*. **1999**, 40, 2521-2536.

36 Ivan, F.; Josef, K.; Michael, S. *J. Elastomers Plast.* **1996**, 28, 106-139.

37 Nilsson, S.; Bernasik, A.; Budkowski, A.; Moons, E. *Macromolecules.* **2007**, 40, 8291-8301.

38 Winnik, M.A.; Feng, J. *J. Coat. Technol.* **1996**, 68, 39-50.

39 Patel, V.R.; Amiji, M.M. *Pharm. Res.* **1996**, 13, 588-593.

40 Baker, W.E.; Scott, C.E.; Hu, G.H. *Reactive Polymer Blending*. **2001**, Hanser Gardner Publications, Inc.

41 Legros, A.; Carreau, P.J.; Favis, B.B.; Michel, A. *Polymer*. **1994**, 35, 758-764.

42 Lee, P.; Kuo, W.; Chang, F. *Polymer*. **1994**, 35, 5641-5650.

43 Pernot, H.; Baumert, M.; Court, F.; Leibler, L. *Nature Materials.* **2002**, 1, 54-58.

44 Paul, D.R.; Bucknall, C.B. *Polymer Blends Volume1: Formulation*. **2000**, John Wiley & Sons, Inc.

45 Triacca, V.J.; Ziaee, S.; Barlow, J.W.; Keskkula, H.; Paul, D.R. *Polymer.* **1991**, 32, 1401-1413.

46 Wong, S.; Mai, Y. *Polymer.* **1998**, 40, 1553-1566.

47 Greco, R.; Sorrentino, A. *Adv. Polym. Tech.* **1994**, 13, 249-258.

48 Greco, R.; Astarita, M.F.; Dong, L.; Sorrentino, A. *Adv. Polym. Tech.* **1994**, 13, 259-274.

49 Fekete, E.; Foldes, E.; Damsits, F.; Pukanszky, B. *Polym. Bull.* **2000**, 44, 363-370.

50 http://en.wikipedia.org/wiki/Surface_tension

51 http://en.wikipedia.org/wiki/Adhesion

52 Wu, S. *Polymer Interface and Adhesion.* **1982**, Marcel Dekker, Inc.

53 Yukioka, S.; Inoue, T. *Polymer*. **1994**, 35, 1182-1186.

54 Farinha, J.P.S.; Vorobyova, O.; Winnik, M.A. *Macromolecules*. **2000**, 33, 5863-5873.

55 Dedecker, K.; Groeninckx, G.; Inoue, T. *Polymer*. **1998**, 39, 5001-5010.

56 Okamoto, M.; Nam, P.H.; Maiti, P.; Kotaka, T.; Nakayama, T.; Takada, M.; Ohshima, M.; Usuki, A.; Hasagawa, N.; Okamoto, H. *Nano Lett.* **2001**, 1, 503-505.

57 Shen, J.; Zeng, C.; Lee, L.J. *Polymer*. **2005**, 46, 5218-5224.

58 Lee, M.; Tzoganakis, C.; Park, C.B. *Polym. Eng. Sci.* **1998**, 38, 1112-1120.

59 Rachtanapun, P.; Selke, S.E.M.; Matuana, L.M. *J. Appl. Polym. Sci.* **2003**, 88, 2842-2850.

60 Harrats, C.; Thomas, S.; Groeninckx, G. *Micro- and Nanostructured Multiphase Polymer Blend Systems: Phase Morphology and Interfaces*. **2005**, CRC Press.

61 Doroudiani, S.; Park, C.B.; Kortschot, M.T. *Polym. Eng. Sci.* **1998**, 38, 1205-1215.

62 Huang, H.; Wang, J. *J. Appl. Polym. Sci.* **2007**, 106, 505-513.

63 Sharudin, R.W.; Nabil, A.; Taki, K.; Ohshima, M. *J. Appl. Polym. Sci.* **2010**, 119, 1042-1051.

64 Park, C.B.; Lee, P.C.; Wang, J.; Padareva, V. *Cell. Polym*. **2006**, 25, 1-18.

65 Kohlhoff, D.; Nabil, A.; Ohshima, M. *Polym. Adv. Technol.* **2012**, 23, 1350-1356.

66 Krause, B.; Diekmann, K.; van der Vegt, N.F.A.; Wessling, M. *Macromolecules*. **2002**, 35, 1738-1745.

67 Sharudin, R.W.; Ohshima, M. *J. Appl. Polym. Sci.* **2012**, 128, 2245-2254.

68 Otsuka, T.; Taki, K.; Ohshima, M. *Macromol. Mater. Eng.* **2008**, 293, 78-82.

69 Lee, P.C.; Wang, J.; Park, C.B. *Ind. Eng. Chem. Res.* **2006**, 45, 175-181.

70 Park, C.B.; Padareva, V.; Lee, P.C.; Naguib, H.E. *J. Polym. Eng.* **2005**, 25, 239-260.

71 Lee, P.C.; Naguib, H.E.; Park, C.B.; Wang, J. *Polym. Eng. Sci.* **2005**, 45, 1445-1451.

72 Kohlhoff, D.; Ohshima, M. *Macromol. Mater. Eng.* **2011**, 296, 770-777.

73 Siripurapu, S.; Gay, Y.J.; Royer, J.R.; DeSimone, J.M.; Spontak, R.J.; Khan, S.A. *Polymer*. **2002**, 43, 5511-5520.

74. Li, Y.; Yao, Z.; Chen, Z.; Cao, K.; Qiu, S.; Zhu, F.; Zeng, C.; Huang, Z. *Chem. Eng. Sci.* **2011**, 66, 3656-3665.

75 Liao, Q.; Tsui, A.; Billington, S.; Frank, C.W. *Polym. Eng. Sci.* **2012**, 52, 1495-1508.

76 Spitael, P.; Macosko, C.W. *Polym. Eng. Sci.* **2004**, 44, 2090-2100.

77 Siripurapu, S.; DeSimone, J.M.; Khan, S.A.; Spontak, R.J. *Macromolecules*. **2005**, 38, 2271-2280.

78 Spitael, P.; Macosko, C.W.; McClurg, R.B. *Macromolecules*. **2004**, 37, 6874-6882.

79 Zhai, W.; Wang, H.; Yu, J.; Dong, J.; He, J. *J. Polym. Sci., Part B: Polym. Phys.* **2008**, 46, 1641-1651.

80 Ruckdaschel, H.; Sandler, J.K.W.; Altstadt, V.; Retting, C.; Schmalz, H.; Abetz, V.; Muller, A.H.E. *Polymer*. **2006**, 47, 2772-2790.

Chapter 2

BUBBLE NUCLEATION AT THE INTERFACE

2.1 Introduction

Polymeric foams are found in virtually every aspect of our daily lives, and they are used in a wide variety of applications, such as cushioning for furniture, food trays, packaging, thermal insulation materials, and in shock and sound attenuation materials.[1] The cell morphology of the foams, which is characterized by the cell density, cell size, and open and/or closed-cell structures, is selected based on the applications.[2] The desired cell morphology in the foams is prepared by selecting appropriate polymers, additives, fillers, processing schemes and tuning the processing conditions.

In polymer foaming processes, bubble nucleating agents such as talc or clay are often used to enhance the bubble nucleation and to improve the uniformity of the cell morphology. The nucleating agent increases heterogeneity in the polymer matrix and provides bubble nucleation sites with low activation energies where homogeneous bubble nucleation is significantly suppressed while heterogeneous bubble nucleation is enhanced.[3,4] The interfacial tension between the polymer matrix and the nucleating agent predominately determines the heterogeneous bubble nucleation and growth behaviors. Differences in the diffusivity and solubility of the foaming agent in the blend polymer could also be key factors for the heterogeneous nucleation of bubbles when disperse polymeric domains are used as bubble nucleating agents during the foaming of polymer blends.

A number of studies have been conducted on polymer blend foams where a minor polymer phase was used as a bubble nucleating agent and the relationship of the nucleation and growth of bubbles with the interfacial properties of the blended polymers was investigated. Sharudin et al. considered using a high interfacial tension polymer as a bubble nucleating agent and investigated the effect of the interfacial tension between polymers on bubble nucleation using PP/PS and PP/PMMA blends as example systems, where PP was used as a nucleating agent.[5] They conducted visual observation experiments, which revealed that the disperse PP domain acted as a bubble nucleating agent due to the higher interfacial tension between PP and PS as well as PMMA. During foam extrusion processes of pure LDPE, microcellular foams could not be produced due to the high activation energy for bubble nucleation. Therefore, Park et al. blended PS with LDPE to induce heterogeneous bubble nucleation, which increased the cell density.[6] In addition to the immiscible polymer blends, block copolymer micelles were also investigated as an effective bubble nucleating agent. Siripurapu et al. reported that the cell density was significantly increased by adding CO_2-philic copolymers, PMMA-g-poly (dimethylsiloxane) (PDMS) and/or PMMA-b-poly (fluorooctyl methacrylate) (PFOMA), to a PMMA matrix.[7] However, Spitael et al. observed that the micelles formed by PS-b-poly (ethylene propylene) (PEP) and/or PS-b-PMMA diblocks were not effective as bubble nucleating agents in a PS matrix.[8] It appears that the role of copolymer micelles is still ambiguous.

Compatibilizers are often used in polymer blends and composites to modify the interfacial properties and to increase the dispersibility of the minor phase in the matrix. Zhai et al. investigated the foaming behavior of PP/PS blends in which the PS-g-PP

copolymer was used as a compatibilizer.[9] The authors reported that PS-g-PP copolymers with longer PS graft chains could improve the compatibility, and the copolymers decreased the domain size and lowered the CO_2 diffusion coefficient. The reduction of the domain size could increase the cell density. Ruckdaschel et al. reported a similar result in their foaming of Poly(2,6-dimethyl-1,4-phenylene ether) (PPE)/Poly(styrene-co-acrylonitrile) (SAN) blends, in which the increase in the interfacial compatibility of the minor phase polymer could improve the dispersibility of the domains and increase the cell density.[10]

Reactive blending was conducted using diblock or graft copolymers to improve the interfacial properties of the minor and matrix phases and to produce well-dispersed polymer blends. Reactive blending is a unique and effective method for preparing a copolymer that has two distinct segments, typically a block or a graft copolymer, such that the copolymer can penetrate into both the matrix and disperse phases and modify the affinity between both phases.[11] In our study of Chapter 3, reactive blending was utilized to form a PET-PC di-block copolymer, and we investigated the effects of the copolymer on the foaming behaviors of PET/PC blends. It was observed that the PET-PC diblock copolymer increased the compatibility and enhanced the interfacial affinity.

For polymer blend foaming processes, the coalescence and aggregation of disperse domains results in less interfacial area and leads to a reduction in the number of bubble nucleation sites. Therefore, it is desirable to prevent the coalescence and aggregation of bubble nucleating agents, i.e., disperse polymer domains, and to uniformly disperse these nucleating agents as much as possible. To increase the dispersibility of the nucleating agents, the interfacial properties of the nucleating agents are modified and the

heterogeneity of the nucleating agents is reduced through modifications of their surfaces or interfaces. These modifications might depress the heterogeneous bubble nucleation rate because when the interfacial tension between blended polymers is less than the surface tensions between the polymers and foaming gas, the energy required for bubble nucleation at the interface becomes high. This competitive effect of surface (interface) modification of bubble nucleating agents, i.e., minor polymer phase, has not yet been quantitatively investigated, although several studies have been reported on successful improvements of the cellular structure by controlling the affinity of the disperse domain with the use of compatibilizers, as mentioned above.

In this study, the CO_2 foaming behavior of a polymer blend, PMMA/PC blend, with a compatibilizer was investigated to determine the effect of interfacial tension between disperse and matrix polymers on bubble nucleation. The copolymer was produced in the PMMA/PC blend through reactive blending and was used as the compatibilizer. PMMA/PC blends have been extensively studied, particularly in terms of the miscibility of the blend.[12,13,14,15,16] The thermal degradation of PMMA occurs at approximately 240°C and produces macro-radicals, which could react with the molecular chains of PC to form a graft copolymer in the PMMA/PC blend. The graft copolymer subsequently increases the miscibility between the PMMA and PC phases.[17] Cole et al. reported that the adhesiveness of the PMMA-PC interface prepared by high-temperature melt blending (reactive blending) was six-times greater than that prepared by solvent blending due to the formation of the graft copolymer.[18] The authors concluded that the thermal degradation reaction provides a unique route to improve the miscibility of the system. We used a grade of PMMA where the thermal degradation temperature was low

(low-T_d PMMA) to produce the copolymer, and used the copolymer as a compatibilizer during the reactive processing of a high-thermal degradation temperature PMMA (high-T_d PMMA) and PC blend. The Palierne model was applied to calculate the interfacial tension between the domain and matrix polymers in the blend prepared through the reactive blending of PMMA/PC with the low-T_d PMMA. By observing the number density of the cell, the number density of the domain and the bubble as well as domain sizes from SEM micrographs of the blend foams, the number of bubbles per unit interfacial area and that of per unit number of domains were calculated to quantitatively determine the effect of interfacial tension on bubble nucleation.

2.2 Experimental

2.2.1 Materials

PC (Taflon A2600, M_w=32,000, Idemitsu Kosan, Japan), which had a density of 1.2 g cm^{-3} and a melt flow index of 6 g 10-min^{-1} (300°C, 1.2 kg), and a high-thermal degradation temperature PMMA (high-T_d PMMA; SUMIPEX LG, M_w=123,000, Sumitomo Chemical, Japan), which had a density of 1.18 g cm^{-3}, a melt flow index of 10 g 10-min^{-1} (230°C, 3.8 kg) and a thermal decomposition temperature, T_d, of 314°C (2% weight loss at 10°C min^{-1} in a nitrogen atmosphere), were used as the disperse domain and matrix polymers, respectively. The low-thermal degradation temperature PMMA (low-T_d, PMMA; M_w=120,000, Aldrich Chemistry, Japan), which had a T_d of 240°C (2% weight loss at 10°C min^{-1} in a nitrogen atmosphere), was used to form a copolymer and make the high-T_d PMMA compatible with PC. Isotactic PP (i-PP; Prime polymer F133A) with a 97% tacticity and a melt flow index of 3 g 10-min^{-1} (230°C, 2.16 kg) was used as a disperse polymer in a reference blend system. i-PP has a melting temperature of 167°C, and its crystallinity is 57.5%. All the polymers were used as received. The glass transition temperatures (T_g) of the low-T_d and high-T_d PMMA are 96°C and 103°C, respectively. The T_g of PC is 151°C. CO_2 (99.95% pure) (Showa-Tansan, Japan) was used as a physical foaming agent.

2.2.2 Preparation of the PMMA/PC and PMMA/PP blends

Both high-T_d and low-T_d PMMA and PC pellets were dried at 70°C in a temperature-controlled oven for at least 2 days to remove moisture before blending.

Pellets of the low-T_d PMMA and PC were first dry-mixed at three different weight ratios of low-T_d PMMA to PC, 0/100, 5/95 and 10/90. These mixtures were fed into a melt-mixer (Labo Plastomill, 4C150 Toyoseiki, Japan) to reactively blend at 240°C. The reactive blending was conducted for 30 min to ensure that the low-T_d PMMA fully reacted with the PC. The obtained samples were subsequently mixed with the high-T_d PMMA using the same melt-mixer at 240°C for 10 min to prepare the PMMA/PC blend. The PMMA/PC blends were prepared with two different weight ratios of the low-T_d and high-T_d PMMA to PC, 90/10 and 70/30. The detailed weight ratios of the low-T_d and high-T_d PMMA to PC in the blends are summarized in Table 2.1.

A high-T_d PMMA and PP blend was prepared as a reference system. The PMMA/PP blend with a 70/30 weight ratio exhibited a co-continuous phase morphology. Therefore, only the 90/10 PMMA/PP blend was prepared by melt-blending for 10 min at 220°C in the same mixer and used as the reference system.

Reactive blending and melt-blending were conducted by rotating a kneading rotor at 10 rpm for the first 2 min, and then the rotation speed was increased to 50 rpm for the remaining time. After blending, the blends were molded into the plate-shape of 35 mm in width, 60 mm in length and 1 mm in thickness using a hot compression molding machine. The copolymer, which was generated by the reaction between low-T_d PMMA and PC, was extracted using a selective solvent (acetone) for PMMA, and the soluble fraction was analyzed by infrared spectroscopy.[14]

Table 2.1 Weight ratio of PMMA/PC blends

Component	high-T_d PMMA/low-T_d PMMA/PC		
Sample No.	1	2	3
PMMA/PC 90/10	90/0/10	89.5/0.5/10	89/1/10
PMMA/PC 70/30	70/0/30	68.5/1.5/30	67/3/30

2.2.3 CO_2 foaming

All the blends were placed into a high pressure autoclave to dissolve CO_2 at 10 MPa under three different sorption and foaming temperatures, 60, 80 and 100°C. After saturating the blends with CO_2 for 22 h, the pressure in the autoclave was released within 2 s to induce foaming. The sorption time of 22 h was fixed for all experiments to ensure the same equilibrium state.

2.2.4 Measurements of PMMA/PC blends reaction

A thermogravimetric analyzer (TGA: DTG-60H, Shimadzu, Japan) was used to determine the thermal degradation temperatures of the high and low-T_d PMMA from the weight loss measured during heating. PMMA was heated from 40 to 240°C at a rate of 10°C min^{-1} and held at 240°C for 60 min. At 240°C, reactive or melt-blending occurred. The entire process was conducted under a nitrogen purge at a flow rate of 50 ml min^{-1}. A differential scanning calorimeter (DSC: Pyris 1 Perkin Elmer) was used to measure the T_g. The samples were heated from 40 to 260°C at a rate of 10°C min^{-1}, held at that temperature for 5 min and then cooled to 40°C. The 1st scan was performed to remove the thermal history, and the T_g was therefore determined from the 2nd scan. The rheological properties were measured using a rheometer (Advanced Rheometric Expansion System, ARES, TA Instruments, USA) to observe the changes in the rheological properties of the

PMMA/PP and PMMA/PC blends. Parallel plate geometry was used for the dynamic frequency sweep tests at 240°C for the PMMA/PC blends and at 220°C for the PMMA/PP blend in the frequency range of 0.01-100 rad s^{-1}. Gap of 1 mm and strains of 10-15% were applied during the measurements. A strain sweep test was also conducted to determine the strain limit for a linear viscoelastic response. The phase angle was checked at lower frequencies to avoid inaccurate data where the phase angle was too close to 90°. [19] Fourier transform infrared spectroscopy (FTIR: VERTEX 70, Bruker Optik GMBH, Germany) was used to investigate the characteristic chemical groups in the PMMA/PC blends in the range of 400-4000 cm^{-1} at a resolution of 4 cm^{-1}. The film of soluble fractions was prepared by solvent evaporation prior to the measurement.

2.2.5 Characterization of blends and foam morphology

Scanning electron microscopy (SEM) was used to observe the blend and cell morphology of the foam. The samples were frozen in liquid nitrogen to create cryogenic fractural surfaces and then coated with gold for 180 s before observation under a SEM (Tiny-SEM 1540, Technex Co. Ltd., Japan) or field emission SEM (JSM-6700F, Jeol, Japan). FESEM (JSM-6700F) images were collected at an acceleration voltage of 10 kV, a current of 5 μA and a wide distance of 8 mm. The image processing software Image J was used to calculate the disperse domain density, N_d, and the number average domain radius, $\overline{R_d}$, from the SEM micrographs.

$$\overline{R_d} = \frac{1}{c}\sum_{i}^{c} R_i \qquad (1)$$

$$N_d = \frac{\phi}{\overline{V_c}} = \frac{\phi}{\frac{4}{3c}\pi\sum_i^c R_i^3} \quad (2)$$

where R_i is the radius of the i-th domain measured from the SEM micrographs. $\overline{R_d}$ is calculated by averaging the domain radii. ϕ is the volume fraction of the disperse domain, and it is calculated from the weight ratios and densities of both polymers.

The interfacial area between the disperse domain and matrix per unit volume of blend, *S*, is calculated by:

$$S = N_d \overline{S_c} = N_d \frac{4}{c}\pi\sum_i^c R_i^2 \quad (3)$$

where $\overline{S_c}$ is the number average domain surface.

The cell density, N_f, and the number average cell radius, $\overline{R_n}$, were also calculated from the SEM micrographs. The bulk densities of the samples before and after foaming were measured using a densitometer (Mirage Electronic Densimeter MD-200S) and used for the cell density calculation. The cell density was then calculated by:[20]

$$N_f = \frac{\rho_s}{\rho_f} \times \left(\frac{n}{A}\right)^{1.5} \quad (4)$$

where *n* is the number of bubbles in a total area *A*. ρ_f and ρ_s are the densities of the foam and solid bulk, respectively.

The number of observable bubbles per unit interfacial area, D_s, and the number of observable bubbles per unit number of domains, D_d, were calculated by

$$D_s = N_f / S \quad (5)$$

$$D_d = N_f / N_d \quad (6)$$

2.3 Theory of Blend Characterization in Brief

2.3.1 Component fraction from the Fox equation

The T_g of a miscible polymer blend is estimated through the Fox equation. When this equation is applied to partially miscible polymer blends to calculate the composition of each phase, it is common to assume that the minor polymer is homogeneously infused in the major polymer phase. We applied the Fox equation to the PMMA/PC blend to estimate the weight fraction of PMMA infused in the PC domain and that of PC infused in the PMMA matrix.[21,22]

$$\frac{1}{T_g^{'}} = \frac{\omega_{PMMA}^{'}}{T_{gPMMA}} + \frac{\omega_{PC}^{'}}{T_{gPC}} \tag{7}$$

and

$$\frac{1}{T_g^{''}} = \frac{\omega_{PMMA}^{''}}{T_{gPMMA}} + \frac{\omega_{PC}^{''}}{T_{gPC}} \tag{8}$$

where $\omega_{PC}^{'}$ is the weight fraction of PC infused in the PMMA-matrix, $\omega_{PMMA}^{'}$ (:=1-$\omega_{PC}^{'}$) is the weight fraction of PMMA in the PMMA-matrix, $\omega_{PMMA}^{''}$ (:=1-$\omega_{PC}^{''}$) is the weight fraction of PMMA in the PC-domain, $\omega_{PC}^{''}$ is the PC weight fraction in the PC-domain, $T_g^{'}$ is the glass transition temperature of the PMMA-matrix, $T_g^{''}$ is the glass transition temperature of the PC-domain, T_{gPMMA} is the glass transition temperature of the pure PMMA and T_{gPC} is the glass transition temperature of the pure PC.

The weight fractions of PC in the PMMA matrix and that of PMMA in the PC domain were calculated using Eqs. (9) and (10) with the T_g data of blend and neat polymers.

$$\omega_{PC}^{'} = \frac{T_{gPC}(T_{gPMMA} - T_g^{'})}{T_g^{'}(T_{gPMMA} - T_{gPC})} \quad = 1 - \omega_{PMMA}^{'} \tag{9}$$

and

$$\omega_{PMMA}^{''} = \frac{T_{gPMMA}(T_{gPC} - T_g^{''})}{T_g^{''}(T_{gPC} - T_{gPMMA})} \quad = 1 - \omega_{PC}^{''} \tag{10}$$

Furthermore, the weight fractions of both the PC domain and the PMMA matrix could be calculated from mass balances by transforming Eqs. (9)-(10)

$$\omega^{'} = \frac{\omega_{PC} - \omega_{PC}^{''}}{\omega_{PC}^{'} - \omega_{PC}^{''}} \tag{11}$$

and

$$\omega^{''} = \frac{\omega_{PC} - \omega_{PC}^{'}}{\omega_{PC}^{''} - \omega_{PC}^{'}} \tag{12}$$

where $\omega^{'}$ is the estimated weight fraction of the PMMA matrix, $\omega^{''}$ is the estimated weight fraction of the PC domain in the blend after reactive blending, and ω_{PC} is the PC domain weight fraction (10% or 30%) in the blend before reactive blending.[21,22]

2.3.2 Estimate of interfacial tension

A sea-island structure is frequently observed in immiscible polymer blends after blending. In the blending process, the morphology evolution consists of stretching the fluid droplet into threads, the break-up of the threads into smaller droplets and the coalescence of the droplets into larger domains.[11] The ultimate domain diameter is related to the force balance, which is a function of the interfacial tension between two components, the viscosity ratio and the shear stress. Palierne has reported a theory for concentrated emulsions with a viscoelastic constituent.[23] This theory can be applied to

polymer blends, which go through dynamic shear with very small drop deformation from a spherical shape; the geometrical relaxation of the disperse domain would lead to a long relaxation process during the dynamic moduli test in the low frequency region.[24] The storage modulus at the relaxation process, i.e., the G' at the secondary plateau, is directly related to the interfacial tension between the disperse domain and the matrix.[25] The Palierne model, which accounts for the viscoelastic nature of the component phases and the particle size distribution in non-dilute emulsions, exhibits a relationship among the complex shear modulus, blend morphology and interfacial tension:[19]

$$G^* = G_m^* \left[\frac{1 + 3/2 \sum_i \frac{\phi_i E_i}{D_i}}{1 - \sum_i \frac{\phi_i E_i}{D_i}} \right] \tag{13}$$

$$E_i = 2(G_d^* - G_m^*)(19G_d^* + 16G_m^*) + \frac{48\beta_d^*\Gamma^0}{R_i^2} + \frac{32\beta_s^*(\Gamma^0 + \beta_d^*)}{R_i^2} + \frac{8\Gamma^0}{R_i}(5G_d^* + 2G_m^*) + \frac{2\beta_d^*}{R_i}(23G_d^* - 16G_m^*) + \frac{4\beta_s^*}{R_i}(13G_d^* + 8G_m^*) \tag{14}$$

and

$$D_i = (2G_d^* + 3G_m^*)(19G_d^* + 16G_m^*) + \frac{48\beta_d^*\Gamma^0}{R_i^2} + \frac{32\beta_s^*(\Gamma^0 + \beta_d^*)}{R_i^2} + \frac{40\Gamma^0}{R_i}(G_d^* + G_m^*) + \frac{2\beta_d^*}{R_i}(23G_d^* + 32G_m^*) + \frac{4\beta_s^*}{R_i}(13G_d^* + 12G_m^*) \tag{15}$$

where Γ^0 is the interfacial tension. G_d^*, G_m^* and G^* are the complex moduli of the disperse domain, matrix and emulsion in a range of frequencies, respectively. ϕ_i is the volume fraction of a domain with a radius R_i. β_d^* is the surface dilatation modulus associated with area variations, and β_s^* is the surface shear modulus attributed to the

resistance of the interface to shear deformation. Both of the complex moduli are frequency dependent.

β_d^* is usually associated with the non-uniformity of the interface, and β_s^* is associated with the resistance to shear deformation. It is assumed that, in the melt blends of this study, the interface is uniformly occupied by the copolymer such that the surface dilatation modulus can be ignored. However, due to the shear deformation resistance of the copolymer, β_s^* should be expressed by:[19]

$$\beta_s^* = \beta_s^{'} + \beta_s^{''} \tag{16}$$

for $\omega\lambda_\beta < 1$:

$$\beta_s^{'} = \beta_0 \tag{17}$$

$$\beta_s^{''} = \beta_0 \omega\lambda_\beta \tag{18}$$

for $\omega\lambda_\beta > 1$:

$$\beta_s^{'} = \beta_s^{''} = \beta_0 \sqrt{\omega\lambda_\beta} \tag{19}$$

where β_0 is a low-frequency plateau in the storage modulus for the copolymer and λ_β is a characteristic relaxation time.

ϕ_i and R_i were calculated from the SEM micrographs of the blend morphology. G_d^* and G_m^* were determined by individually measuring the complex moduli of the neat polymers. Then, Γ^0 and β_0 were determined such that the complex moduli estimated by the model could fit the experimental data. The detailed procedure for calculating the interfacial tension can be found elsewhere.[19]

2.3.3 Heterogeneous bubble nucleation at the interface

The heterogeneous bubble nucleation rate (J) induced by a pressure quench can be expressed by the following equations:[26]

$$J = N^{2/3}\left(\frac{1-m_A}{2}\right)\left(\frac{2\gamma_A}{\pi mBF}\right)^{1/2}\exp\left[\frac{-16\pi\gamma_A^3 F}{3kT_{sys}(P_{bub,cr}-P_{sys})^2}\right] \quad (20)$$

where

$$F = \frac{1}{4\gamma_A^3}\left[\gamma_A^3\left(2-3m_A+m_A^3\right)+\gamma_B^3\left(2-3m_B+m_B^3\right)\right] \quad (21)$$

$$m_A = \cos\theta = \frac{\gamma_A^2+\gamma_{AB}^2-\gamma_B^2}{2\gamma_A\gamma_{AB}} \quad (22)$$

$$m_B = \cos\varphi = \frac{\gamma_B^2+\gamma_{AB}^2-\gamma_A^2}{2\gamma_B\gamma_{AB}} \quad (23)$$

γ_A, γ_B and γ_{AB} represent the surface tension between polymer A and the blowing agent (CO_2), polymer B and CO_2, and the interfacial tension between polymer A and polymer B, respectively. N is the number density of the dissolved blowing agent molecules. $P_{bub,cr}$ is the pressure in a critical bubble, and P_{sys} is the system pressure. k is the Boltzmann constant, and T_{sys} is the system temperature. In the CO_2 foaming process, m, which is the molecular mass of gas molecules, is 44 g mol^{-1}, and B is normally approximated to be 2/3. θ and φ are the angles of γ_A with γ_{AB} and γ_B with γ_{AB}, respectively.

2.4 Results and Discussion

2.4.1 Characterization of blend properties

Because PP is immiscible and did not react with PMMA, only the PMMA/PC blends were characterized using TGA, DSC and FTIR. The thermal stabilities of the high-T_d PMMA and low-T_d PMMA were analyzed using TGA, and the results are shown in Figure 2.1. Note that the high-T_d PMMA exhibited a very small degradation with less than a 2% weight loss. However, the degradation of low-T_d PMMA began a weight loss at 200°C and a knee-point appeared in the weight-time curve at approximately 240°C. At the end of the TGA measurement, 37% of the low-T_d PMMA proceeded through the thermal degradation reaction. In our experiment, it was observed that a mixing time of 40 min was sufficient to complete the grafting reaction between the low-T_d PMMA and PC.

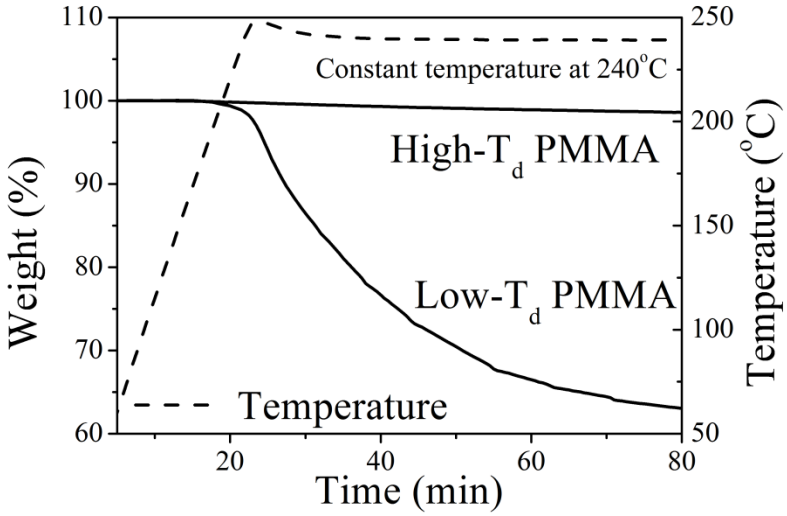

Figure 2.1 TGA curves of high-T_d and low-T_d PMMA

During the thermal degradation reaction between the low-T_d PMMA and PC, a graft copolymer was generated. This copolymer exhibits the same peaks as PMMA and PC in the FTIR spectra, which makes identifying the occurrence of a grafting reaction difficult. The selective solvent extraction method was employed to overcome this difficulty, where a PMMA-rich phase is selectively dissolved in acetone. The PC-rich phase remained as the non-soluble residues.[27,28] Because PC molecules were chemically connected to PMMA in the form of a copolymer and infused in the PMMA-rich phase, the PC chain segments should be detected in the PMMA-rich phase and extracted along with the PMMA molecules in acetone. When the extracted phase, which is the PMMA-rich phase, is analyzed by FTIR, the carbonyl stretching band of the PC carbonate group at 1773 cm^{-1} and that of the PMMA ester group at 1733 cm^{-1} may appear in the spectra. However, the presence of the 1773 cm^{-1} band might be superposed by the 1733 cm^{-1} band or the peak would be too small to be detected. In our study, Debier's strategy was employed to overcome the aforementioned problem.[28] Figure 2.2 presents the FTIR spectra of the 70/30 (PMMA/PC) blends extracted in acetone. Two characteristic peaks appeared in the spectra, which are very important for identifying the existence of the copolymer: (1) 1017 cm^{-1}, the vibration from a para-disubstituted benzene ring in PC and (2) 990 cm^{-1}, the vibration of the hydrocarbon bond in PMMA. The emergence of a peak at 1017 cm^{-1} and the increase in the height of the peak with the increasing amount of low-T_d PMMA indicated that sample blends No. 2 and 3 in Table 2.1 were partially miscible. For the 70/30 weight ratio blend (sample No. 1), the amount of copolymer dissolved in acetone may have been too small to be detected.

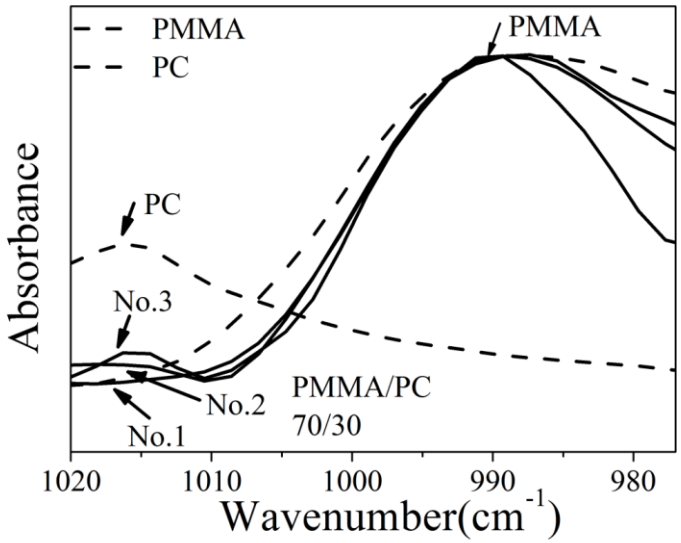

Figure 2.2 FTIR spectra of PC, PMMA and 70/30 wt% PMMA/PC blends (No. 1, 2 and 3)

With the presence of the copolymer, the miscibility of the high-T_d PMMA and PC increased and the T_g of both PMMA and PC became closer to each other. Figure 2.3 presents the DSC curves of the 70/30 (PMMA/PC) blends with different weight ratios of low-T_d PMMA in the blend. Because PMMA and PC were not completely miscible, two T_g peaks clearly appeared in the heating curves of the blend samples. However, the T_g of PC (PC-disperse domain), which is denoted by $T_g^{''}$, decreased from 151 to 138°C, and the T_g of PMMA (PMMA matrix), $T_g^{'}$, increased from 96 to 99.9°C as the low-T_d PMMA ratio increased.

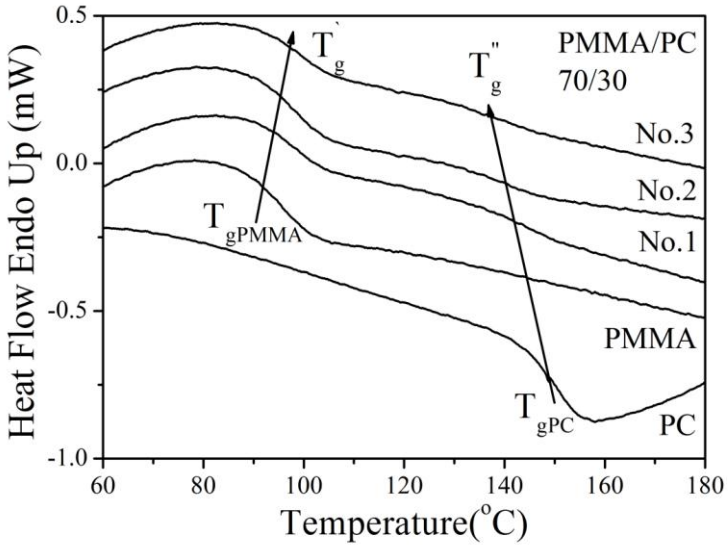

Figure 2.3 DSC heating curves of PC, PMMA and 70/30 wt% PMMA/PC blends (No. 1, 2 and 3)

With the assumption that the PMMA segment in the copolymer was homogeneously infused into the PC domain and a miscible state was achieved in both the domain and matrix, the Fox equation was applied to the DSC data and the weight fraction of PMMA infusing into the disperse PC domain and that of the PC infusing into the PMMA matrix was estimated using Eqs. (9) and (10). The results of these estimates are presented in Table 2.2. The details of the calculations are given elsewhere.[29,22] Although the thermal degradation of the high-T_d PMMA is difficult, it appears to have some capability of generating copolymers through the degradation reaction: 9% PC in the PMMA matrix and 8% PMMA in the disperse PC domain in 70/30 were estimated in sample No. 1, where no low-T_d PMMA was used. As the ratio of low-T_d PMMA increased, the weight percentage of PMMA infused in the PC domain increased to 16% in sample No. 3 of the 70/30 blend.

Table 2.2 T_g and the estimated weight percentage of PMMA and PC composition in the PMMA-matrix and PC-domain of the PMMA/PC blends

PMMA/PC		PMMA matrix				PC domain			
		$T_g^{'}$ (°C)	$\omega_{PMMA}^{'}$	$\omega_{PC}^{'}$	$\omega^{'}$	$T_g^{''}$ (°C)	$\omega_{PMMA}^{''}$	$\omega_{PC}^{''}$	$\omega^{''}$
70/30	**No. 1**	98.8	91%	9%	74%	144	8%	92%	26%
	No. 2	99.0	91%	9%	73%	140	13%	87%	27%
	No. 3	99.9	88%	12%	75%	138	16%	84%	25%
90/10	**No. 1**	97.2	96%	4%	93%	145	7%	93%	7%
	No. 2	97.3	95%	5%	93%	140	13%	87%	7%
	No. 3	97.6	95%	5%	94%	137	18%	82%	6%

Figure 2.4 presents the SEM micrographs of the morphologies of the PMMA/PC (70/30 and 90/10) and PMMA/PP 90/10 blends. The sea-island morphology was observed in all the blends. The disperse domain was PP or PC, whereas the matrix was PMMA. Because the PMMA/PC blends were prepared by reactive blending, the domain size of PC was considerably smaller than the PP domain. As can be seen in the DSC data of samples No. 1 to No. 3, a higher amount of low-T_d PMMA would produce considerably more graft copolymer and increase the miscibility between the PC domain and PMMA matrix. Consequently, the diameter of the domain decreased. This increase in miscibility was also observed in the SEM micrographs presented in Figure 2.4. Cavities or voids were observed in the PMMA/PP and PMMA/PC No. 1 blends. These morphological features were produced due to detachment of the PP or PC domain from the PMMA matrix when we cut the samples for SEM observation. The number of cavities or voids became insignificant as the amount of lower-T_d PMMA increased.

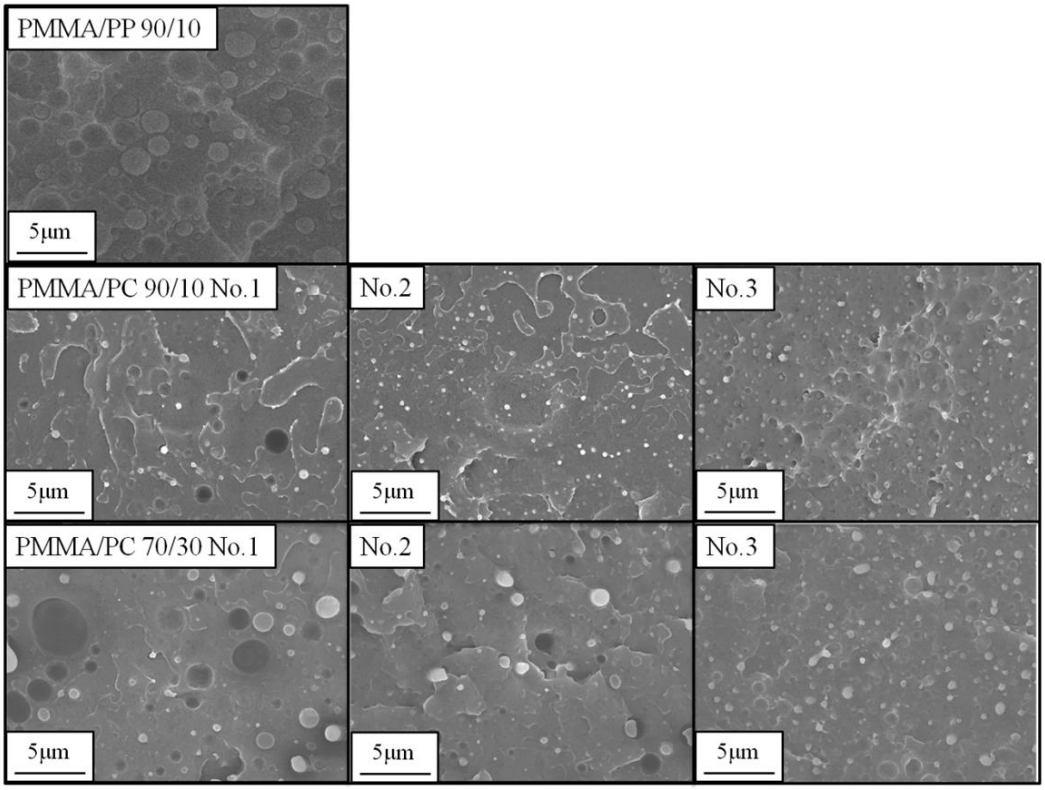

Figure 2.4 Morphologies of the 90/10 wt% PMMA/PP and the 70/30 wt% and 90/10 wt% PMMA/PC blends (No. 1, 2 and 3)

2.4.2 Characterization of interfacial tension

The storage modulus, G', of the PMMA/PC blends is shown in Figure 2.5. The viscoelastic modulus in un-crosslinked amorphous polymers over a broad range of frequencies normally starts from the glassy zone, across a transition zone to a plateau zone, and finally to the terminal zone. In our study, the pure PMMA and PC polymers were already in the terminal zone at 240°C, where both the storage modulus and loss modulus decreased with decreasing frequency. When the frequency was less than 0.25 rad s^{-1}, the storage modulus, G', of PMMA was too small to be accurately measured. The G' of PC also exhibited an erroneous value at frequencies less than 0.063 rad s^{-1}. The

immiscible characteristic of the PMMA/PP blend produced a less distinct plateau region; therefore, it was not included in Figure 2.5. For the PMMA/PC blends, a plateau region emerged in the frequency range from 1 to 0.063 rad s^{-1}. The plateau at lower frequencies was attributed to the relaxation of the disperse domain, whereas the plateau at higher frequencies was attributed to the relaxation of the matrix.[25] Here, the secondary plateau is highlighted because it is directly related to the interfacial tension. When the interfacial tension decreases, the domain size decreases and the total interfacial area increases. The former effect shifts the interfacial contribution to higher frequencies, whereas the latter increases its modulus.[30] With the increase of copolymer, the plateau was shifted to a higher position, as shown in Figure 2.5 where the plateau changes from 0.4 rad s^{-1} in sample No. 1 with a 70/30 ratio to 1 rad s^{-1} in sample No. 3 with the same ratio. The magnitude of the plateau also increased to a higher modulus, as shown in the enlarged figure in lower right corner.

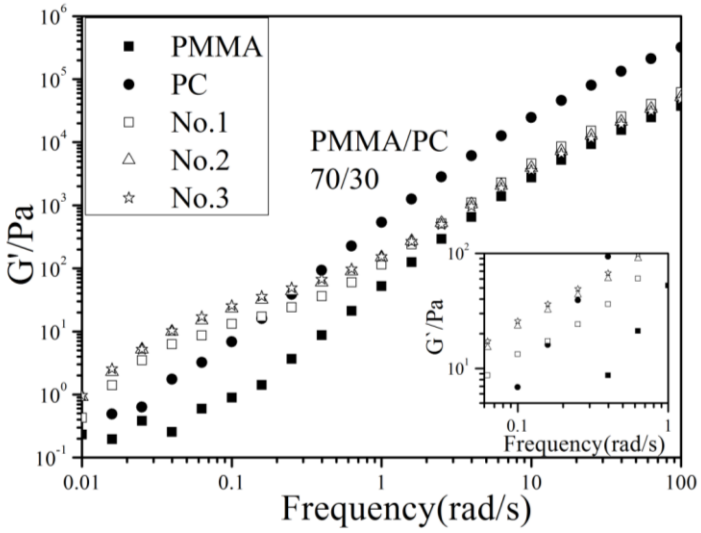

Figure 2.5 Comparison of the dynamic storage modulus curves, G', of PC, PMMA and 70/30 wt% PMMA/PC blends (No. 1, 2 and 3)

The measured domain size was subsequently used to calculate the interfacial tension of the PMMA/PP and PMMA/PC blends through the Palierne model, Eqs. (13)-(19). The calculated interfacial tensions are provided in Table 2.3. The interfacial tension was determined to fit the experimentally obtained storage modulus and loss modulus curves with the model. Figure 2.6 presents the experimental data for both the storage and loss modulus curves and the model estimate for both the PMMA/PC and PMMA/PP blends. The Palierne model provided a good agreement with the experimental data at frequencies greater than 0.25 rad s^{-1}. Specifically, the location and the magnitude of the secondary plateau were precisely expressed by the model. Some fitting error at low frequencies was most likely due to the inaccurate measurement of the storage modulus of PMMA. Note that the PMMA/PP blend exhibited the greatest interfacial tension of 4.7 mN m^{-1} and the PMMA/PC blends exhibited less interfacial tension, which decreased in both the 70/30 and 90/10 blends as the amount of low-T_d PMMA was increased.

For polymer blends, the interfacial tensions have been reported to be rather small values of approximately 1-10 mN m^{-1}.[30] In the case of polymer blends prepared by reactive blending, the value of interfacial tension might be even smaller. The nonreactive nylon/rubber blend had an interfacial tension as high as 9 mN m^{-1}, whereas the reactive nylon/rubber blend was on 0.25 mN m^{-1}.[31] Virgilio et al. used the breaking thread method and measured the interfacial tension of PMMA with PP to be 5 mN m^{-1}.[32] Moussaif et al. employed the imbedded fiber retraction method and measured the interfacial tension of PMMA with PC to be 0.6 mN m^{-1}.[33] The interfacial tension calculated in this study was quite close to these reported values.

Table 2.3 Interfacial tension calculated using the Palierne model

Blend component		*Interfacial tension(mN/m)*
PMMA/PP 90/10		4.7
PMMA/PC	No. 1	0.76
	No. 2	0.63
70/30	No. 3	0.51
PMMA/PC	No. 1	0.47
	No. 2	0.41
90/10	No. 3	0.37

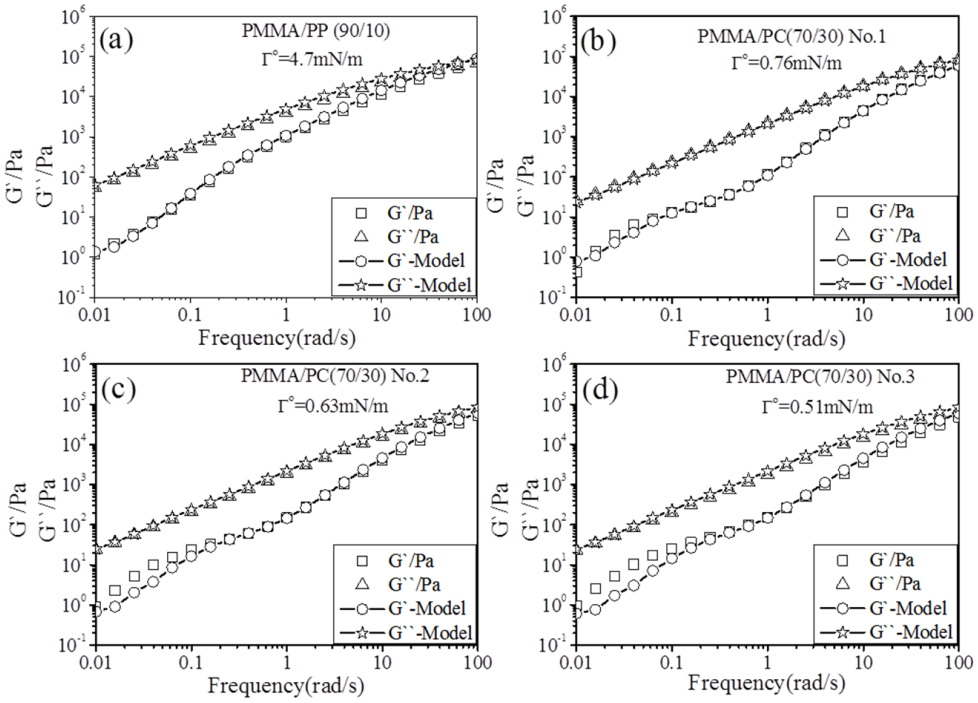

Figure 2.6 Fit of the Palierne model to the dynamic modulus data

The domain diameter, $2\times\overline{R_d}$, and the interfacial area per unit blend volume, *S*, for the PMMA/PC and PMMA/PP blends were then calculated using Eqs. (1)-(3), and the data were plotted along with interfacial tension, as shown in Figure 2.7. The disperse domain size in the PMMA/PC blends was smaller and their interfacial areas became larger than those of the PMMA/PP blend. With the increase of copolymer (low-T_d

PMMA ratio), the diameter of the PC disperse domain decreased. A better distribution of the PC disperse domain was achieved and larger interfacial areas were produced, as shown in Figure 2.7 (b). Comparing the results of the PMMA/PC blends with a 70/30 weight ratio to those of the PMMA/PC blends with a 90/10 ratio, the PMMA/PC blends with a lower PC ratio exhibited a smaller domain diameter and less interfacial area at all low-T_d PMMA contents.

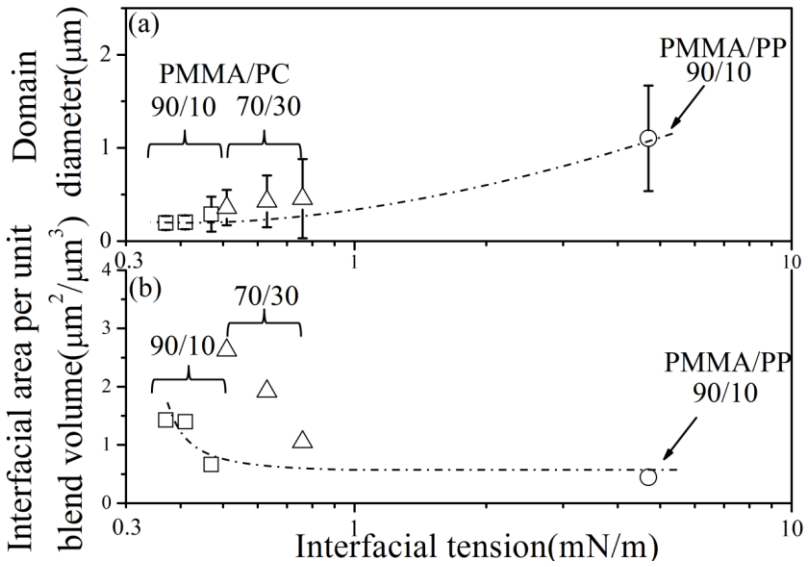

Figure 2.7 Number average domain diameter, $2\times\overline{R_d}$ (a) and the interfacial area per unit blend volume, *S* (b) of PMMA/PP and PMMA/PC blends

2.4.3 Cell morphology of foamed blends

Foaming was conducted using 10 MPa of CO_2 at three different temperatures, 60, 80 and 100°C. Under these foaming temperatures, the PMMA phase could be foamed while the PC and PP domains would not be foamed, but they could serve as bubble nucleating agents. Figure 2.8 presents the SEM micrographs of the foamed PMMA,

PMMA/PP and PMMA/PC blends. The cell density and the cell size were calculated from the SEM micrograph, and the results are illustrated in Figure 2.9. All the foamed samples possessed spherical cell geometries, but the PC domains were not clearly identified in the cell. This cell morphology of the PMMA/PC blends was quite different from that of the Polyethylene glycol (PEG)/PS blend foams reported by Taki et al.[34] Sharudin et al. reported that bubble growth dominated at the interface when the interfacial tension was very large.[5] When the polymers in the blend have extremely small interfacial tension, the bubble could grow into one polymer.

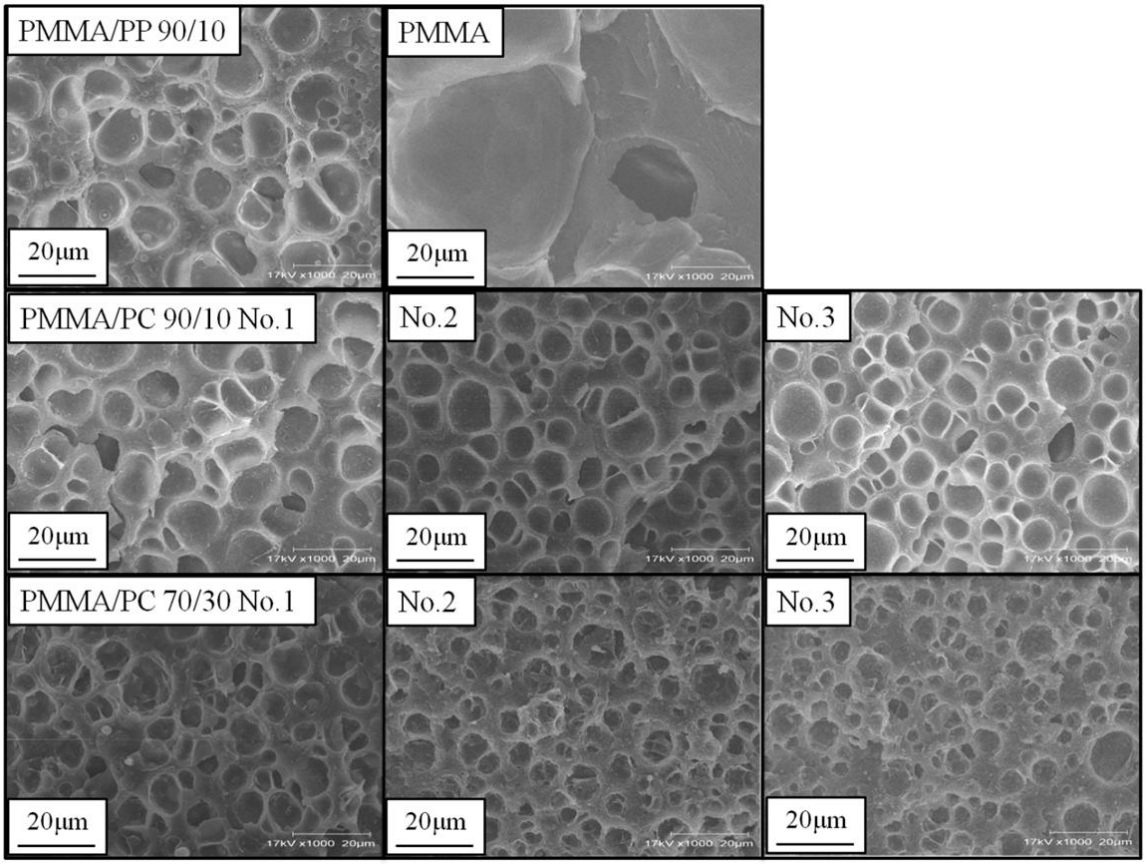

Figure 2.8 SEM micrographs of PMMA, PMMA/PP and PMMA/PC foamed at 80°C under 10 MPa of CO_2

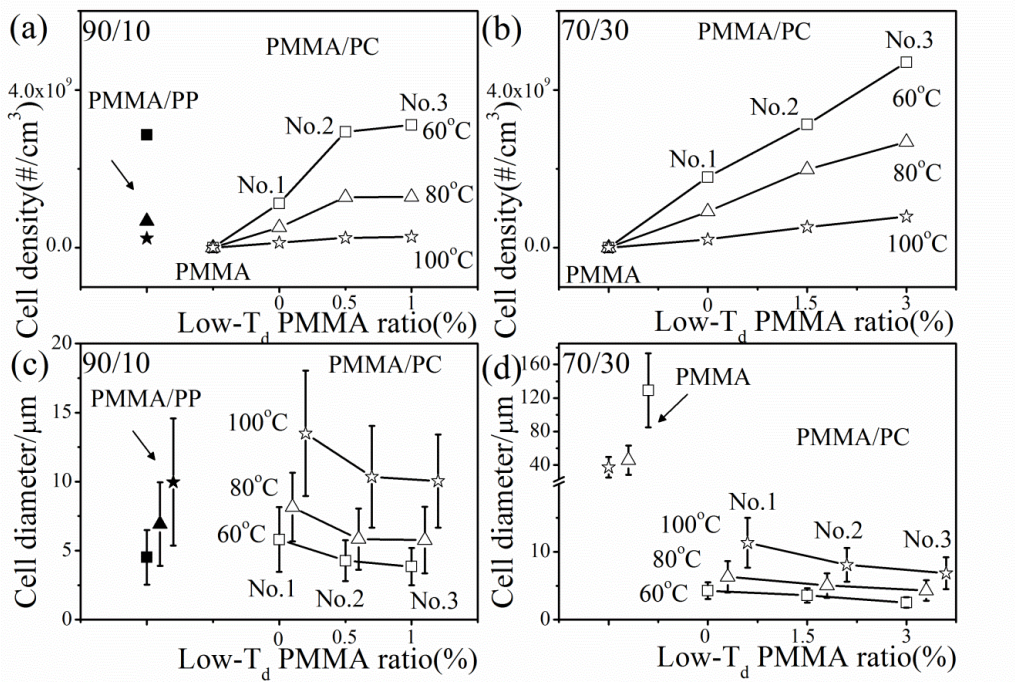

Figure 2.9 Cell density (a) and (b), and cell size (c) and (d), of the blends foamed at 60, 80 and 100°C

By blending PP or PC with high-T_d PMMA, the cell density of the foamed blends became considerably greater than that of the foamed high-T_d PMMA alone (Figure 2.9 (a) and (b)). This result indicates that heterogeneous bubble nucleation became more effective than homogeneous bubble nucleation with the addition of the PP or PC polymer to PMMA. The experimental results also indicate that the cell density increased and the cell size decreased with decreasing foaming temperature. With the decrease of the foaming temperature, the solubility of CO_2 in the polymer blends and the viscoelasticity of the matrix polymer increased. The increase of solubility provided a higher degree of supersaturation, and the increase of viscosity reduced the growth. Both effects served to increase the cell density and reduce the cell size.

In the blend foaming process, heterogeneous bubble nucleation predominantly occurs. The cell density becomes a function of the interfacial area and the surface and interfacial tensions, as described by Eqs. (20)-(23). Although the exact value of J was difficult to obtain in our study due to the lack of some physical parameter values, the effect of interfacial tension on bubble nucleation could be analyzed from the view of classic heterogeneous bubble nucleation theory. Goel et al. reported the surface tension of PMMA with CO_2, γ_A, at 60°C and 10 MPa to be 17 mN m^{-1}.[35] Wong et al. measured the surface tension of PC-CO_2, γ_{B2}, at 240°C and 15 MPa to be 19.5 mN m^{-1}, and Taki et al. measured the surface tension of PP-CO_2, γ_{B1}, at 170°C and 10 MPa to be 12 mN m^{-1}.[36,37] Compared with the surface tensions of those polymers under pressurized CO_2, the interfacial tension of PMMA with PC, γ_{AB2}, is extremely small while the interfacial tension of PMMA with PP, γ_{AB1}, is fairly large. Figure 2.10 presents two cases of blend foaming, (Case 1); the interfacial tension between the blend polymers is larger and comparable to those of the surface tensions between polymers and CO_2, and (Case 2); the interfacial tension between the blend polymers is considerably less than those of the surface tensions between polymers and CO_2 (Case 2). The angles of θ and φ are given in Eqs. (20)-(23). In case 1, which is the case of PMMA/PP, less energy is required for bubble nucleation at the interface between polymers. However, in case 2, which is the case of PMMA/PC, more energy is required for bubble nucleation at the interface between two polymers. Consequently, the nucleation at the interface between PMMA and PP is easier than at the PMMA and PC interface.

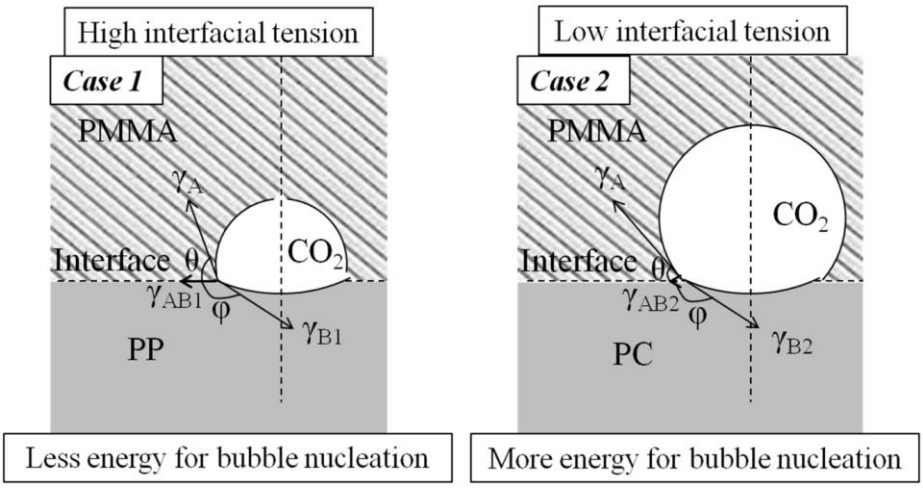

Figure 2.10 Schematic diagram for the formation of a bubble at the PMMA/PP interface with high interfacial tension (Case 1) and the PMMA/PC interface with low interfacial tension (Case 2)

The number of bubbles per unit interfacial area and the number of bubbles per unit number of domains are shown in Figure 2.11. The PMMA/PP blend with a high interfacial tension had a greater number of bubbles per unit interfacial area than the PMMA/PC blends. Furthermore, the number of bubbles per unit number of domains decreased with the reduction of interfacial tension because both the nucleation potential at the interface and the domain size decreased. Although the PP domain might not be well-dispersed due to the higher interfacial tension between PP and PMMA, the PP domain has greater potential for heterogeneous bubble nucleation than the PC domain. The experimental results indicate that the polymer blends qualitatively follow the classical heterogeneous bubble nucleation mechanism during the foaming process. The interfacial tension has a two-pronged effect on bubble nucleation: the interfacial area can be increased but the heterogeneity is decreased with decreasing interfacial tension. When

the interfacial tension is large and the heterogeneity plays a primary role in physical foaming, such as in PMMA/PP, the cell density would decrease with the reduction of interfacial tension between the blended polymers. When the interfacial tension is not considerably great and the interfacial area plays a dominant role, the cell density would increase with the reduction of interfacial tension, as illustrated in Figure 2.12.

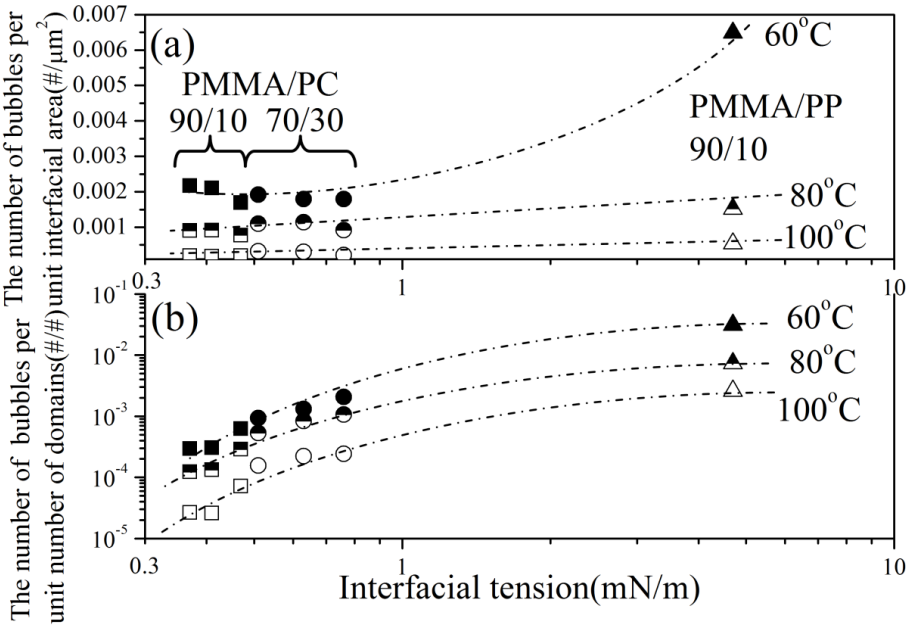

Figure 2.11 Number of bubbles per unit interfacial area (a) and the number of bubbles per unit number of domains (b) at different foaming temperatures: 60, 80 and 100°C

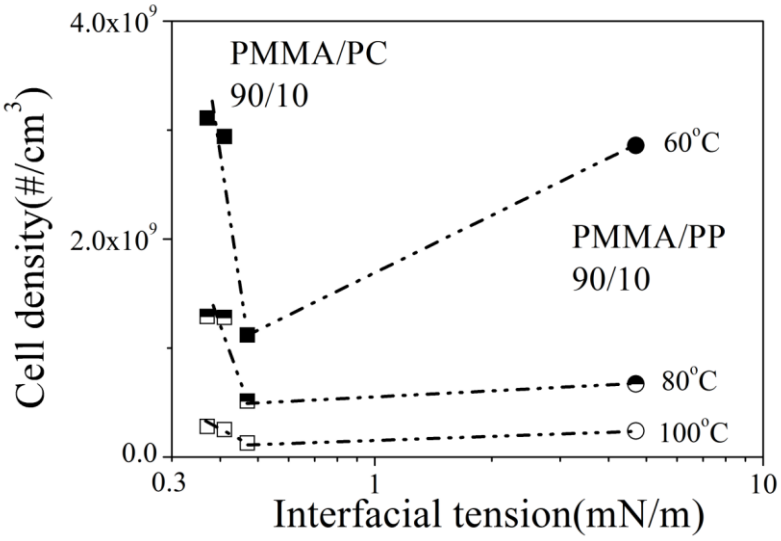

Figure 2.12 Cell density as a function of interfacial tension at different foaming temperatures: 60, 80 and 100°C

2.5 Conclusions

In this study, the nucleation and growth of bubbles at the interface between blended polymers was investigated by pressure quenched batch foaming. The miscibility of the PC domain with the high-T_d PMMA was controlled by the addition of low-T_d PMMA, which has a low thermal decomposition temperature and serves as a compatibilizer by forming a graft copolymer. The graft copolymer could be produced by melt blending. The copolymer reduces the dissimilarity of the PC domain from the PMMA matrix and reduces the interfacial tension between the two polymers. The reduction of interfacial tension could promote better distribution of the disperse domain, and the bubble nucleation was enhanced by increasing the area of the interface. However, the miscibility at the interface between two blended polymers might affect the bubble nucleation in different manner. When the interfacial tensions were considerably large and were intentionally decreased to improve the dispersibility of the minor phase, the number of bubbles per unit interfacial area and the number of bubbles per unit number of domains could decrease and significantly affect the overall cell density.

The actual performance of the compatibilizer on cell morphology could be determined by compromising the increase of total area of heterogeneous interface and the decrease of bubble nucleation ability per unit interfacial area. In this study, the true number of bubble nuclei could not be observed due to limitations of the SEM observation. However, this study clearly reveals an aspect of the effect of the bubble nucleating agent on the resulting cell morphology.

2.6 References

1 Klempner, D.; Frisch, K.C. *Handbook of Polymeric Foams and Foam Technology*. **1991,** Oxford University Press.

2 Ruckdaschel, H.; Gutmann, P.; Altstadt, V.; Schmalz, H.; Muller, A.H.E. *Adv. Polym. Sci.* **2010**, 227, 199-252.

3 Colton, J.S.; Suh, N.P. *Polym. Eng. Sci.* **1987**, 27, 485-492.

4 Colton, J.S.; Suh, N.P. *Polym. Eng. Sci.* **1987**, 27, 493-499.

5 Sharudin, R.W.; Nabil, A.; Taki, K.; Ohshima, M. *J. Appl. Polym. Sci.* **2010**, 119, 1042-1051.

6 Park, C.B.; Lee, P.C.; Wang, J.; Padareva, V. *Cell. Polym*. **2006**, 25, 1-18.

7 Siripurapu, S.; DeSimone, J.M.; Khan, S.A.; Spontak, R.J. *Macromolecules*. **2005**, 38, 2271-2280.

8 Spitael, P.; Macosko, C.W.; McClurg, R.B. *Macromolecules*. **2004**, 37, 6874-6882.

9 Zhai, W.; Wang, H.; Yu, J.; Dong, J.; He, J. *J. Polym. Sci., Part B: Polym. Phys.* **2008**, 46, 1641-1651.

10 Ruckdaschel, H.; Sandler, J.K.W.; Altstadt, V.; Retting, C.; Schmalz, H.; Abetz, V.; Muller, A.H.E. *Polymer*. **2006**, 47, 2772-2790.

11 Baker, W.E.; Scott, C.E.; Hu, G.H. *Reactive Polymer Blending*. **2001,** Hanser Gardner Publications, Inc.

12 Kyu, T.; Lim, D. *J. Chem. Phys*. **1990**, 92, 3951-3956.

13 Kyu, T.; Saldanha, J.M. *J. Polym. Sci., Part B: Polym. Phys*. **1990**, 28, 97-104.

14 Rabeony, M.; Hseih, D.T.; Garner, R.T.; Peiffer, D.G. *J. Chem. Phys*. **1992**, 97, 4050-4511.

15 Marchese, P.; Celli, A.; Fiorini, M. *Macromol. Chem. Phys.* **2002**, 203, 695-704.

16 Montaudo, G.; Puglisi, C.; Samperi, F. *J. Polym. Sci., Part A: Polym. Chem*. **1998**, 36, 1873-1884.

17 Ko, C.C.; Kyu, T.; Smith, S.D. *J. Polym. Sci., Part B: Polym. Phys*. **1995**, 33, 517-525.

18 Cole, P.J.; Cook, R.F.; Macosko, C.W. *Macromolecules.* **2003**, 36, 2808-2815.

19 Asthana, H.; Jayaraman, K. *Macromolecules*. **1999**, 32, 3412-3419.

20 Kohlhoff, D.; Ohshima, M. *Macromol. Mater. Eng.* **2011**, 296, 770-777.

21 Porter, R.S.; Wang, L.H. *Polymer*. **1992**, 33, 2019-2030.

22 Marin, N.; Favis, B.D. *Polymer.* **2002**, 43, 4723-4731.

23 Palierne, J.F. *Rheologica Acta*. **1990**, 29, 204-214.

24 Scholz, P.; Froelich, D.; Muller, R. *J. Rheol*. **1989**, 33, 481-499.

25 Graebling, D.; Muller, R.; Palierne, J.F. *Macromolecules.* **1993**, 26, 320-329.

26 Blander, M. *Adv. Colloid Interface Sci*. **1979**, 10, 1-32.

27 Kyu, T.; Ko, C.C.; Lim, D.S.; Smith, S.D.; Noda, I. *J. Polym. Sci., Part B: Polym. Phys*. **1993**, 31, 1641-1648.

28 Debier, D.; Devaus, J.; Legras, R. *J. Polym. Sci., Part A: Polym. Chem*. **1995**, 33, 407-414.

29 Kim, W.N.; Burns, C.M. *Macromolecules.* **1987**, 20, 1876-1882.

30 Larson, R.G. *The Structure and Rheology of Complex Fluids*. **1999**, Oxford University Press.

31 Wu, S. *Polym. Eng. Sci*. **1987**, 27, 335-343.

32 Virgilio, N.; Desjardins, P.; L`Esperance, G.; Favis, B.D. *Macromolecules.* **2009**, 42, 7518-7529.

33 Moussaif, N.; Jerome, R. *Macromol. Symp*. **1999**, 139, 125-135.

34 Taki, K.; Nitta, K.; Kihara, S.; Ohshima, M. *J. Appl. Poly. Sci*. **2005**, 97, 1899-1906.

35 Goel, S.K.; Bechman, E.J. *Polym. Eng. Sci*. **1994**, 34, 1137-1147.

36 Wong, A.; Leung, S.N.; Li, G.Y.G.; Park, C.B. *Ind. Eng. Chem. Res*. **2007**, 46, 7107-7116.

37 Taki, K.; Murakami, T.; Ohshima, M. *Asian Workshop on Polymer Processing in Singapore*, **2002**.

Chapter 3

BUBBLE GROWTH AT THE INTERFACE

3.1 Introduction

A variety of polymeric foams are currently commercially available to facilitate our daily lives. Polymer foams are used in a variety of applications, such as furniture, transportation, packaging, shock and sound attenuation.[1] The foams' applications are directly related to their cell morphology, which can be characterized by cell density, cell size, open and/or closed-cell structures.[2] The desired cell morphology is produced by a combination of the suitable chemical structure of the matrix, the specialized interfacial morphology of multi-components as well as the right processing conditions.

Additives are commonly introduced into polymers to make polymer composites for accelerating bubble nucleation and creating uniform cell morphology. The additives provide a large number of active sites with lower activation energy because the interface between the additives and polymer has a very high surface tension.[3,4] Differences in the surface tension as well as the viscoelasticity, solubility and diffusivity of physical foaming agents between polymers or between polymers and additives can adjust both the heterogeneous bubble nucleation and the growth at the interface.

For both polymer blends and polymer composites, the interface plays an important role for bubble nucleation and growth. Sharudin et al. studied the effect of interfacial tension on bubble nucleation in PP/PS and PP/PMMA blends.[5] Their visual observation experiments revealed that bubble nucleation was enhanced at the interface of

polymer blends that had higher interfacial tension. Semi-crystalline polymers, such as PP and Poly(L-Lactide) (PLLA), create the interface between crystalline and amorphous phases, which affects the bubble nucleation and growth when they are foamed. Baldwin et al. experimentally showed that semi-crystalline polymers achieved a high cell density and concluded that the interface between the crystalline and amorphous phases served as a preferential site for bubble nucleation.[6,7] However, Taki et al. observed that CO_2-foamed PLA favored bubble nucleation around spherulites only when the physical foaming agent, CO_2 in this case, was liberated from the growing spherulites.[8] The isothermal treatment under pressurized CO_2 or the absorption of CO_2 at elevated pressure and constant temperature near its melting point enhanced the crystallization and thickened the crystalline lamella. In this lamellar thickening process, the dissolved physical blowing agent (PBA) was expelled from the growing crystalline phase to the amorphous phase. As a result, the concentration of PBA increased at the interface between the crystalline and amorphous phases and enhanced the bubble nucleation at the interface.

The properties of the interface can be modified by adding some compatibilizers to the polymers or by modifying the surface of the additives, which increase the affinity between polymers or between the additive and the polymer matrix. Zhai et al. investigated the foaming behavior of PP/PS blends using PS-g-PP copolymer as a compatibilizer.[9] They reported that PS-g-PP copolymers with longer PS graft chains could improve the interface compatibility: the domain size decreased and the diffusion coefficient of CO_2 was lowered. When the blends were foamed with CO_2 by pressure quenching, higher cell densities as well as higher expansion ratios were observed.

Ruckdaschel et al. similarly observed that the higher interfacial compatibility improved the dispersion of domains and increased the cell density.[10]

According to the heterogeneous nucleation mechanism, a higher interfacial tension between two polymers should accelerate heterogeneous nucleation at the interface of both polymers. However, sufficient amounts of compatibilizer should lower the interfacial tension and might reduce the heterogeneous bubble nucleation rate. A higher compatibility could suppress the heterogeneous nucleation at the interface even though it could improve the dispersion of minor polymer domains. Thus, it is interesting to see the effect of interfacial compatibility on the cell morphology of foam.

A PC and PET blend system was chosen in this study to investigate the effect of interfacial compatibility, which is controlled by the transesterification reaction between the two polymers. The PC/PET blend has been extensively studied, particularly regarding the miscibility of this blend.[11] PET/PC has been established as an immiscible blend that could become partially and eventually totally miscible by the transesterification reaction and can be accelerated by a variety of catalysts, such as lanthanides, titanium and calcium/antimony.[12,13,14] The transesterification reaction generates copolymers containing long blocks of both PET and PC as by-products, which increases the miscibility between the PET and PC phases.[15] As a result, a small amount of copolymers is sufficient to compatibilize PET with PC. Thus, transesterification provides a unique route to improve the miscibility of the system without any other additives. This study investigated the effect of blend compatibility on cell morphology by varying the degree of transesterification, i.e., the annealing time. The presence of residual catalysts in the PET could carry out transesterification. Thus, no external catalyst was introduced.

3.2 Experimental

3.2.1 Materials

PC (Idemitsu, Taflon A2600, M_w=32,000), whose melt flow index (300°C 1.2 kg) is 6 g 10-min^{-1}, and PET (Mitsui Chemical, J125, M_w=56,000), whose inherent viscosity is 0.75 dl g^{-1}, were used as received. CO_2 (99.95% pure) (Showa-Tansan, Japan) was used as the physical foaming agent.

3.2.2 Preparation of PET/PC blends

PET and PC pellets were dried in a vacuum oven at room temperature for at least 2 days to remove moisture before blending. Pellets of both polymers were dry-mixed at two different weight ratios of PET to PC (10/90 and 30/70) and were fed into a melt mixer (Labo Plastomill, 4C150 Toyoseiki, Japan) at 270°C to prepare the blends. The melt mixing was conducted by rotating the mixture at 10 rpm for 2 min and then increasing it to 50 rpm for 8 min. The polymers were exposed to a temperature of 270°C for a total of 10 min.

3.2.3 Annealing procedure

After melt mixing, the PET/PC blend was placed in vacuum chamber for 2 days to remove moisture and then annealed in an oven at 280°C for three different time periods (1, 5 and 10 h) under nitrogen atmosphere. The blends with different transesterification degrees were obtained by changing the annealing time. After annealing, the blends were molded into plate-shape samples of 35 mm in width, 60 mm in length

and 1 mm in thickness on the hot press at temperature 280°C, under 10 MPa hydrostatic pressure for 6 min. At the beginning of compression, the hydrostatic pressure was released three times to disengage air or gas from sample. In the cooling procedure, the samples were taken out from the hot press and placed between two metal plates at room temperature to be cooled down.

3.2.4 Measurement of transesterification degree

Annealing at high temperatures induces transesterification, which changes several properties of the blend polymer, the glass transition temperature, T_g, being one of them. T_g was measured by differential scanning calorimetry (DCS: Pyris 1 Perkin Elmer) by heating the samples to 280°C at a rate of 10°C min^{-1}, holding at that temperature for 5 min and then cooling them to 200°C. In the cooling procedure of DSC, the samples had to be kept at 200°C for 30min so that PET could crystallize thoroughly and could not show cold crystallization in the heating procedure. The temperature was further decreased to 40°C to perform the second scan.[16] The rheological properties were also measured by a rheometer (Rheometric Scientific; Advanced Rheometric Expansion System, ARES) to clarify the changes in the PET/PC blend properties from annealing. Rectangular torsion geometry was used to conduct dynamic temperature ramp tests from 40°C to 200°C at a heating rate of 2°C min^{-1}. The constant oscillation frequency of the torsion bar was set to 1 rad s^{-1} with 0.1% constant strain. The test specimens were approximately 10 mm wide, 1 mm thick and 40 mm long.[17]

Attenuated Total Reflection Fourier Transform Infrared Spectroscopy (ATR-FTIR) (Perkin Elmer Spotlight 400) was used to detect the characteristic chemical groups

in the PET/PC blends in the range of 750-4000 cm^{-1} at a resolution of 2 cm^{-1}. The blend was compressed to prepare a thin film prior to the measurement. Nuclear Magnetic Resonance (^{1}H-NMR) (JEOL EX400) measurement was performed on the annealed blend sample to quantify the transesterification reaction. The annealed blend polymer sample was dissolved in a mixture of deuterated trifluoroacetic acid and deuterated chloroform ($CF_3COOD/CDCl_3$) at a 20/80 volume ratio. Tetramethylsilane (TMS) was used as an internal standard to measure the chemical shift.[16]

3.2.5 CO_2 foaming

All PET/PC blends were placed in a high pressure autoclave to dissolve CO_2 at 10 MPa for 22.3 h at 60°C. After removing the sample from the autoclave without foaming, it was immediately placed on an aluminum plate and was foamed on the hot press by heating it at 120°C for 1 min. The foaming temperature was fixed at 120°C, the point at which the change in cell morphology against annealing time is clearly observed. The sorption time of 22.3 h was also fixed to ensure that all blends reached an equilibrium state with CO_2.

3.2.6 Scanning electron microscopy (SEM)

The foamed samples were first frozen in liquid nitrogen to create cryogenic fracture surfaces that were then coated with gold for 30 s prior to observation under Tiny-SEM or SEM (JSM-6700F). The SEM (JSM-6700F) images were observed at an acceleration voltage of 10 kV, a current of 5 μA and a wide distance of 8 mm.

3.3 Results and Discussion

3.3.1 Characterization of transesterification

Figure 3.1 shows the DSC curves of the 30/70 (PET/PC) blend at different annealing times. The T_g of PC, T_{gPC}, decreased to 120.57°C as the annealing time increased. In the immiscible blends, each polymer's T_g should be visible. However, the shift of T_{gPC} to a lower temperature indicates the partial miscibility of PET with PC. T_{gPC} of the blend annealed for 10 h showed a broader thermal profile, indicating a wider range of molecular weight distribution and greater miscibility of both polymers. Unfortunately, the T_g of PET, T_{gPET}, could not be identified in the DSC curves for any blend.

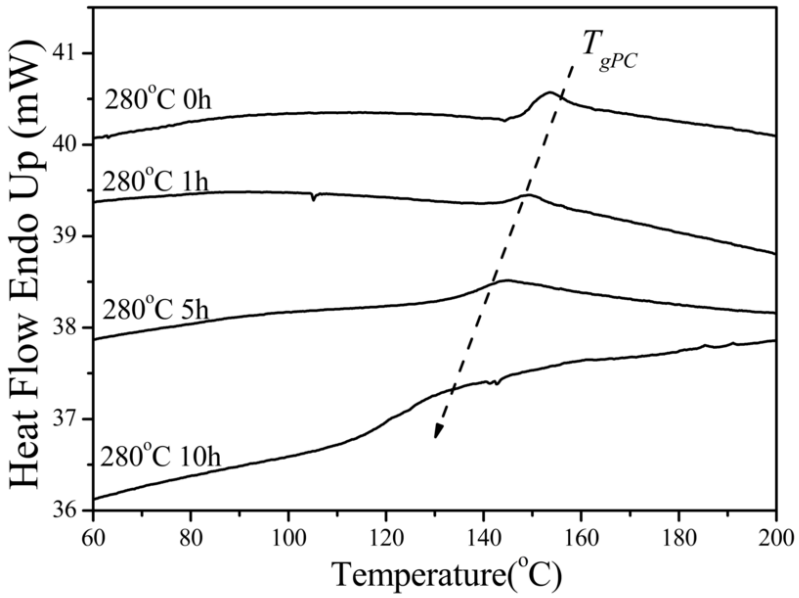

Figure 3.1 DSC curves for the 30/70 wt% PET/PC blend after annealing at 280°C for 0 (non-annealed blend), 1, 5 and 10 h.

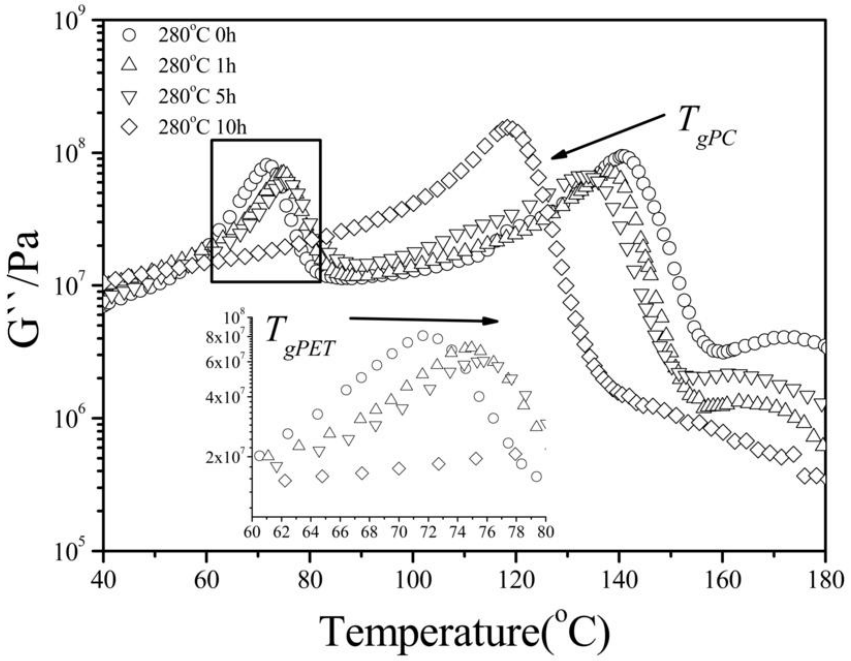

Figure 3.2 Measurements of the shear loss moduli (G") of PET/PC 30/70 wt% blends annealed at 280°C for 0 (non-annealed blend), 1, 5 and 10 h.

Rheological measurements were made to identify the T_{gPET}. The glass transition temperature of polymers can be identified from a peak G"-temperature curve.[18] The shear loss modulus, G", of the blend samples annealed for different time lengths are shown in Figure 3.2. All blends except one (10 h) had two peaks. The peak at the lower temperature corresponds to the T_{gPET} and the peak at higher temperature is the T_{gPC}. The T_{gPET} increased with an increased annealing time, as shown in the enlarged figure at lower left corner. The T_{gPC} decreased with increased annealing time, which coincided with the result of DSC measurements. The PET/PC (30/70) annealed for 10 h shows a single peak in the G"-temperature curve. The miscible polymer blend revealed an

intermediate glass transition temperature that fell between those of individual polymers.[19] Thus, 10 h of annealing made the PET/PC (30/70) miscible. The annealing time did not significantly change the G" value at 40°C, indicating that the degradation during the annealing process is negligible.

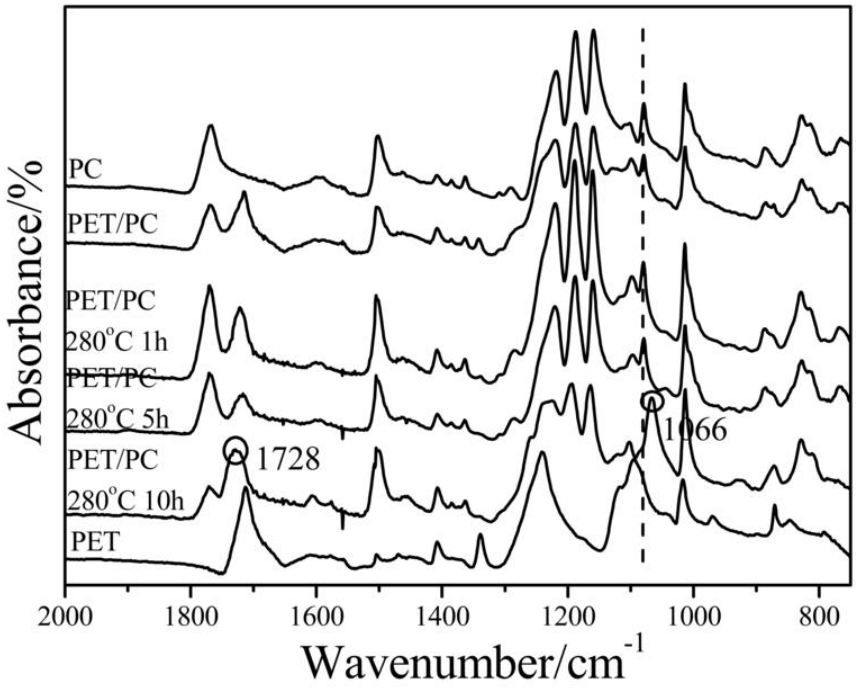

Figure 3.3 ATR-FTIR spectra of PC, PET and PET/PC 30/70 wt% annealed at 280°C for different times: 0 (non-annealed blend), 1, 5 and 10 h.

Figure 3.3 shows the FTIR spectra of the PET/PC (30/70) blend. Two characteristic peaks are very important for identifying the existence of copolymer in the spectra: (1) 1066 cm^{-1}, which is the vibration from an aromatic ester group and (2) 1728 cm^{-1}, which is the carbonyl stretching of an aromatic ester.[12] Only the sample annealed

for 10 h clearly exhibited the peaks at 1066 and 1728 cm^{-1} band. Conversely, no significant peaks were observed in the samples annealed for 1 or 5 h, although at these earlier time points, the amount of ester groups might have been too small to be detected by FTIR. The characteristic peak of the aliphatic-aromatic carbonate group does not show up on the FTIR spectrum because it undergoes ethylene carbonate degradation at 280°C.

The NMR results are shown in Figure 3.4. NMR can detect smaller amounts of copolymers than FTIR in PET/PC blends. As shown in Figure 3.4, there are six important peaks (a: 8.14, b: 8.18, c: 8.22, d: 8.29, e: 8.33, f: 8.38) in the region of terephthalic proton resonance. If no transesterification occurs, the molecular structure of PET does not change and the ethylene group exists at both ends of all terephthalic units. Thus, the four protons in the terephthalic units stay in the same environment and create a single peak at 8.14 (a). When the transesterification reaction occurs at one end of the terephthalic units and the ethylene group is substituted by benzene, the condition of four protons changes and multiple peaks (b: 8.18, c: 8.22, d: 8.29, e: 8.33) happen. When the transesterification reaction occurs on both end of terephthalic unit, a singlet arises at a chemical shift of 8.38 (f). The degree of transesterification can be calculated by identifying the copolymer, i.e., the number of terephthalic units that change, because the number of terephthalic units is kept constant in the blend.[16] The resulting degree of transesterification is listed in Table 3.1. Figure 3.4 (1) and Table 3.1 show that no copolymer is detected in non-annealed blends (annealing time: 0 h) or those annealed for 1 h. However, the blend annealed for 10 h shows an 89% degree of transesterification, which exceeds the necessary 5% degree of transesterification that is sufficient to make the PET/PC blend miscible, and shows one single T_g.[13]

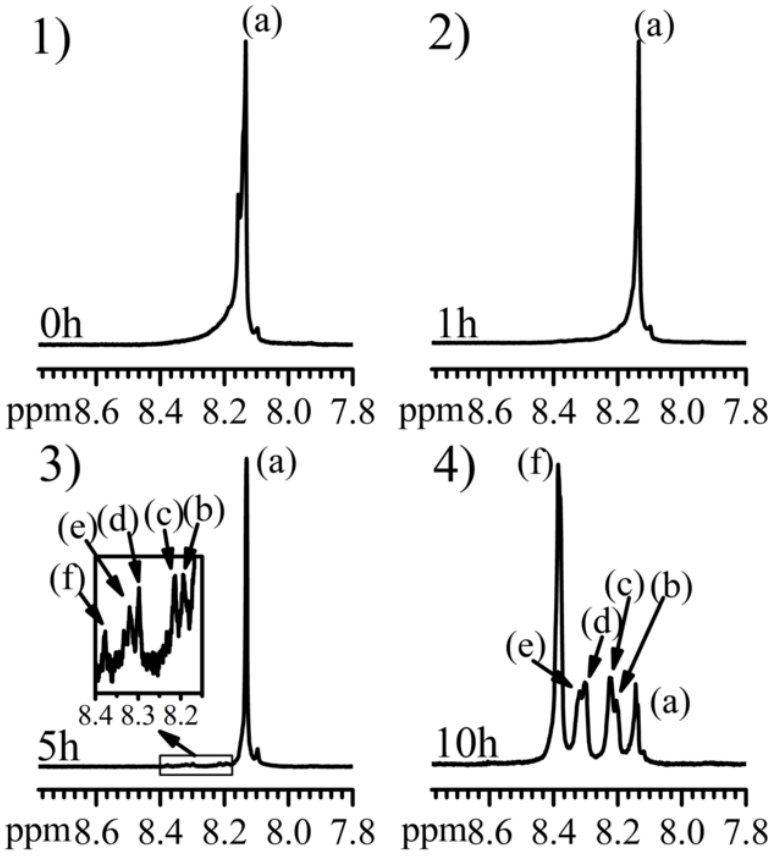

Figure 3.4 NMR spectra of the PET/PC 30/70 wt% blends annealed at 280°C for different times: 1) 0 h, 2) 1 h, 3) 5 h and 4) 10 h.

Table 3.1 Transesterification degree of PET/PC (30/70) blend

Annealing time 30/70 (PET/PC)	0 h	1 h	5 h	10 h
Transesterification	0%	0%	4.08%	89.85%

Figure 3.5 shows SEM micrographs of the PET/PC (30/70) blend morphology. Sea-island morphology is observed in the PET/PC (30/70) blend annealed for 0 and 1 h. The disperse domains are PET, while the matrix is PC. PET domains aggregate to

minimize the free energy and grow larger with increased annealing time because PET is thermodynamically immiscible with PC. The size of the PET disperse domains became larger with increasing annealing time. The boundaries between the PET disperse domains and the PC matrix became fuzzy as the annealing time increased and completely disappeared in the blend annealed for 10 h.

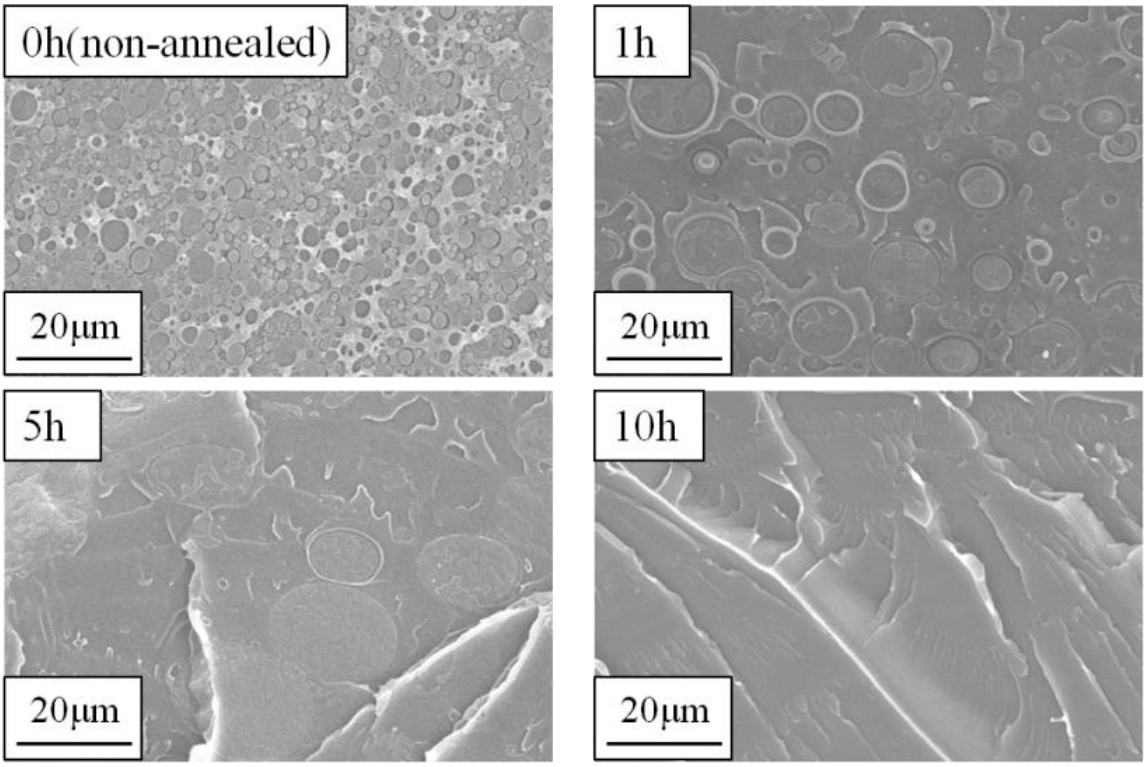

Figure 3.5 The blend morphology of PET/PC 30/70 wt% annealed at different times: 0 (non-annealed blend), 1, 5 and 10 h.

3.3.2 Cell morphology of foamed blends

Figure 3.6 shows SEM micrographs of the foamed PET/PC (30/70) blends. All blends were foamed under the same condition: CO_2 was dissolved at 60°C, 10 MPa for 22.3 h, and foaming was conducted by heating up and holding the samples at a

temperature of 120°C for 1 min. The SEM micrographs show that both the non-annealed PET/PC (30/70) blend and the sample annealed for 1 h had many particles in pores or surrounded by pores. This cell morphology is very similar to that of the PEG/PS blend foams reported by Taki et al.[20] The presence of crystalline domains prevented the PET from foaming at temperatures below 120°C and PET domains remained as spherical domains. When the non-annealed PET/PC (30/70) blend was foamed, the PET domains acted as a bubble nucleating agent at the interface between PET and PC. The interface between both polymers was weak and easily detached from the PC matrix in bubbles because the interfacial tension between PET and PC was high. The bubbles easily coalesced around the PET particles, trapping the particles in the pores.

As the annealing time increased to 1 or 5 h, the interface became stronger, and the adhesiveness of the PET particles to the PC matrix increased due to copolymer formation. However, the interface still acted as a bubble nucleation site due to a certain degree of heterogeneity, as shown in the blend morphology. Thus, large bubbles were found more often around particles than in the matrix as observed in the cell morphology of the blends annealed for 1 and 5 h. When the blends annealed for 1 and 5 h were foamed, the PET particles did not completely detach from the PC matrix and were connected to the PC matrix by a thin cell wall. As for PET/PC (30/70) blend annealed for 10 h, because the interface between PET and PC disappeared (Figure 3.5), and the T_g of the blend polymer decreased to a temperature slightly lower than the foaming temperature, it produced a uniform cell morphology and a microcellular structure.

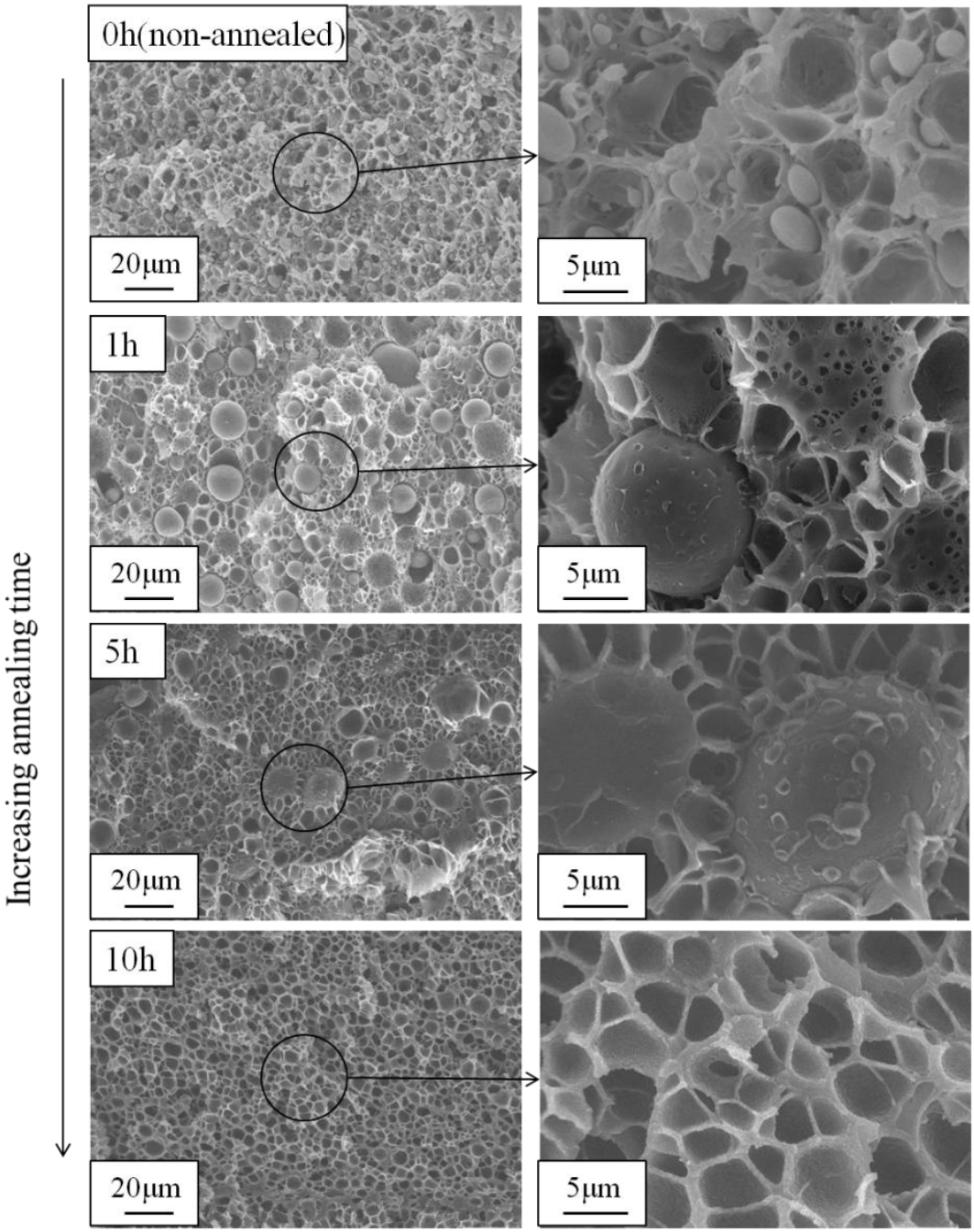

Figure 3.6 SEM micrographs of PET/PC 30/70 wt.% at different annealing times: 0 (non-annealed blend), 1, 5 and 10h.

Figure 3.7 shows the foaming results of PET/PC blended at ratio of 10/90. The effect of annealing time on the cell morphology of the foamed PET/PC (10/90) blend was

the same as that observed in the PET/PC (30/70) blend. However, because there was less amount of PET in the 10/90 blend than in the PET/PC (30/70) blend, the PET domain size remained smaller due to less coalescence. Figure 3.7 shows high magnification SEM micrographs that reveal small spherical PET domains in the pores or PET disperse domains connected to the matrix by fibrils.

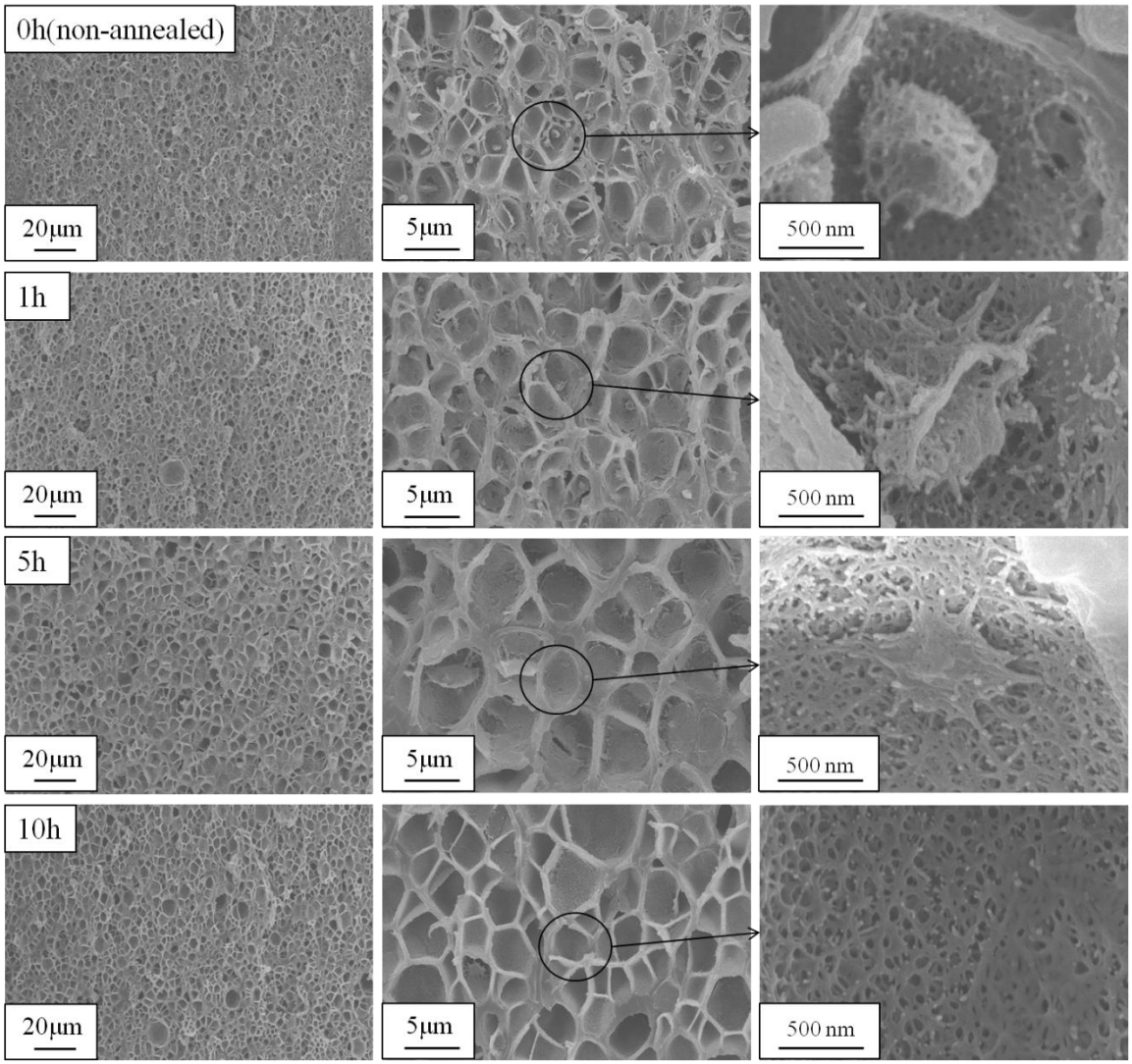

Figure 3.7 SEM micrograph of PET/PC 10/90 wt% at different annealing times: 0 (non-annealed blend), 1, 5 and 10 h.

Transesterification reaction might occur during the melt mixing of PET/PC (10/90) and therefore the affinity of PET for PC becomes higher. As a result, the PET domains in the cell morphology have fibrils connecting to the matrix. After annealing the blend for 1 h, the PET domains are deformed from spherical to irregular shapes due to stronger interfacial adhesion. After annealing for 5h, the PET domains are difficult to detect in the SEM micrographs of foamed blends. It is possible that the PET domains embedded into the PC matrix on the cell wall without forming a clear boundary. An annealing time of 10 h generated homogeneous PET/PC blend and therefore increased the uniformity of the cell morphology in the PET/PC (10/90) blend.

3.4 Conclusions

In this study, the bubble growth at the interface of the polymer blend was investigated using two different PET/PC blends. The miscibility of PET with PC was changed by altering the annealing time. Annealing the blends induces a transesterification reaction at the interface. As the annealing time increased, the degree of transesterification increased and the interface of both polymers became fuzzy. Varying the annealing time prior to foaming changed the miscibility of both polymers at the interface. The changing miscibility affected the heterogeneous bubble nucleation and growth at the interface as observed by the cell morphology of the foamed blends. Comparing the cell morphology of the blends with different miscibilities showed that the interface played an important role in bubble growth of physical foaming. When the interfacial adhesion between two polymers was weak, the bubbles nucleated easily and grew at the interface, and the cell morphology showed that PET particles were located in the pores or were surrounded by bubbles. When the miscibility increased at the interface, the PET particles formed fibrils to connect with the matrix. Uniform cell morphology was obtained when both polymers were miscible. This study clearly showed the role of the interface in bubble nucleation and growth and the effect of the miscibility of two polymers on cell morphology.

3.5 References

1 Klempner, D.; Frisch, K.C. *Handbook of Polymeric Foams and Foam Technology*. **1991,** Oxford University Press.

2 Ruckdaschel, H.; Gutmann, P.; Altstadt, V.; Schmalz, H.; Muller, A.H.E. *Adv. Polym. Sci.* **2010**, 227, 199-252.

3 Colton, J.S.; Suh, N.P. *Polym. Eng. Sci.* **1987**, 27, 485-492.

4 Colton, J.S.; Suh, N.P. *Polym. Eng. Sci.* **1987**, 27, 493-499.

5 Sharudin, R.W.; Nabil, A.; Taki, K.; Ohshima, M. *J. Appl. Polym. Sci.* **2010**, 119, 1042-1051.

6 Baldwin, D.F.; Park, C.B.; Suh, N.P. *Polym. Eng. Sci.* **1996**, 36, 1437-1445.

7 Baldwin, D.F.; Park, C.B.; Suh, N.P. *Polym. Eng. Sci.* **1996**, 36, 1446-1453.

8 Taki, K.; Kitano, D.; Ohshima, M. *Ind. Eng. Chem. Res.* **2011**, 50, 3247-3252.

9 Zhai, W.; Wang, H.; Yu, J.; Dong, J.; He, J. *J. Polym. Sci., Part B: Polym. Phys.* **2008**, 46, 1641-1651.

10 Ruckdaschel, H.; Sandler, J.K.W.; Altstadt, V.; Retting, C.; Schmalz, H.; Abetz, V.; Muller, A.H.E. *Polymer.* **2006**, 47, 2772-2790.

11 Nassar, T.R.; Paul, D.R.; Barlow, J.W. *J. Appl. Polym. Sci.* **1979**, 23, 85-99.

12 Suzuki, T.; Tanaka, H.; Nishi, T. *Polymer.* **1989**, 30, 1287-1297.

13 Zhang, Z.; Xie, Y.; Ma, D. *Eur. Polym. J.* **2001**, 37, 1961-1966.

14 Fiorini, M.; Pilati, F.; Berti, C.; Toselli, M.; Ignatov, V. *Polymer.* **1997**, 38, 413-419.

15 Ma, D.; Zhang, G.; He, Y.; Ma, J.; Luo, X. *J. Polym. Sci., Part B: Polym. Phys.* **1999**, 37, 2960-2972.

16 Marchese, P.; Celli, A.; Fiorini, M. *Macromol. Chem. Phys.* **2002**, 203, 695-704.

17 Kohlhoff, D.; Ohshima, M. *Macromol. Mater. Eng.* **2011**, 296, 770-777.

18 The Society of Polymer Science. *Kisokoubunnshikagaku*. **2006**, Tokyo-Kagaku-Dojin Press.

19 Nemoto, T.; Takagi, J.; Ohshima, M. *Polym. Eng. Sci.* **2010**, 50, 2408-2416.

20 Taki, K.; Nitta, K.; Kihara, S.I.; Ohshima, M. *J. Appl. Polym. Sci.* **2005**, 97, 1899-1906.

Chapter 4

NANOPOROUS STRUCTURE ON THE CELL WALL

4.1 Introduction

In physical foaming, bubble nucleation can be induced either by temperature or pressure quench.[1] When polymer composites or polymer blends are physically foamed, the heterogeneous interface in the polymer normally becomes a bubble nucleation site. The molecules of the blowing agent diffuse into the interface and form the gaseous space, i.e., bubbles. The bubbles are expanded by allowing the pressure difference between the bubble and the polymer matrix to be a driving force of growth. During bubble expansion, stretching-induced structures can be formed. Fukasawa et al. studied nanopores on the cell walls of bubbles in PC microcellular foams.[2] They observed the bubble growth in situ using a polarized optical microscope and obtained birefringence data. The data proved that the polymer was stretched along the wall of the bubbles. They speculated that the nanopores would be formed on the cell wall of PC foams by the orientation-induced crystallization and the discharge of CO_2 from the crystals. Although PC itself is essentially an amorphous polymer, they noted the possibility of crystallization of PC by CO_2 plasticization. However, they failed to show any concrete crystallization data to confirm the occurrence of crystallization under CO_2 foaming. In fact, they conducted differential scanning calorimetry (DSC) and wide-angle X-ray diffraction (WAXD) measurements and did not detect crystallization.

Similar nanoporous structures have been observed on the cell walls of amorphous Polyether imide (PEI) and Polyether sulfone (PES) microcellular foams. Sorrentino et al. reported that a nanoporous structure with pore diameters of few hundred nanometers could be formed in PES by a solid state foaming with a fast and large degree of super saturation.[3] Miller et al. reported a nanoporous structure with a 100 nm average pore diameter and a porous strut thickness less than 60 nm in PEI microcellular foams.[4] They speculated that either secondary bubble nucleation or spinodal decomposition occurred on the cell wall and formed the nanoporous structure. They noted that secondary bubble nucleation could be induced by stress-strain deformations during cell expansion. However, they could not consolidate the secondary nucleation or spinodal decomposition. Moreover, Krause et al. reported interesting experimental results from PSU foam with open nanopores on the cell walls in the early stage of fine cell foaming research.[5] Nanopores with diameters ranging from 10 to 100 nm were formed by adding a solvent. They speculated that the fluctuations in the cell wall thickness were significantly enhanced by the plasticization effect of the solvent molecules. The fluctuations lead to the formation of nanopores on the cell wall. This formation mechanism of the nanoporous structure was only conjecture, as confirming evidence of this speculation was not presented.

The formation of nanoporous structures might not be directly related to the bubble nucleation or spinodal decomposition of the gas-polymer phase separation. In fact, similar nanoporous structures have been observed in stretched glassy or semi-crystalline polymer films. This fine structure, called craze, is very much similar to nanopores on the cell walls of foams.[6,7,8] Crazes are deformation zones where non-oriented polymeric

solids are transformed into fibrils by high tension. If the applied tension is sufficiently large, the microvoids grow and coalesce to form fibrils, which are a few nanometers in diameter.[6] The crazing zone generally propagates perpendicular to the applied tension. Crazes are formed at highly stressed regions associated with stress concentrations and molecular inhomogeneity. The main difference between craze and plastic deformation is the presence of voids. With the formation of voids, large strains change the distortional plasticity (plastic deformation) to dilatational deformation (crazing).[7] During stretching, plastic strain first occurs in the stress-concentrated region and then leads to the development of lateral stresses. Subsequently, either global plastic shear deformation outside the initial region or cavitational deformation inside the initial region occurs depending on the strain conditions (strain, strain rate, temperature, etc.) and polymer characteristics (molecular weight, entanglement density and crosslinks).[8] Polymers with a high entanglement density, such as PC, PEI and PES, favor cavitational deformation and crazing at temperatures close to their glass transition temperatures, T_g.[9,10,11] Environmental crazing (dilatational deformation of polymers in contact with solvents) is frequently utilized to facilitate crazing behavior.[12,13,14] The solvent acts as a crazing agent and decreases the T_g, i.e., the plasticization effect to the polymers and the reduction of the surface tension.[6] The plasticizing effect easily orients the molecular chains in the stretching direction, which readily facilitates craze. The reduction in the surface tension suppresses the excess energy of microvoid formation and enhances the craze initiation.

The cell wall undergoes biaxial elongational stretching during the polymer foaming process.[15] The formation of microvoids or cavitational deformation could be induced during biaxial elongational stretching. The nanoporous structure, similar to that

during the crazing process, could be generated on the cell wall. Because CO_2 has a plasticization effect and reduces the surface tension, this process could simultaneously facilitate the formation of microvoids or cavitational deformation (crazing). Therefore, the nanoporous structure is likely generated by crazing instead of orientation-crystallization. In this study, the effect of the foaming temperature on the nanoporous structure on the cell wall of PC foams was thoroughly investigated, and the structure was compared with that induced by crazing in terms of the formation conditions, such as strain, strain rate and processing temperature. Furthermore, the effect of environmental crazing on the cell structure of foams was also investigated by using acetone as a crazing agent.

4.2 Experimental

4.2.1 Materials

PC (Idemitsu, Taflon A2600, M_w=32,000), whose melt flow index (300°C 1.2 kg) is 6 g 10-min^{-1}, was used as received. CO_2 (99.95% pure) (Showa-Tansan, Japan) was used as the physical blowing agent and acetone (99.5% pure) (Wako, Japan) was used as the co-blowing agent.

4.2.2 Tensile test

The stretching experiments were conducted using a tensile tester (AGS-1kNJ, Shimadzu Corp., Japan) with a heating chamber (TEC-N300, TRA). 10 mm wide and 1 mm thick PC specimens were prepared. The gauge length was set at 20 mm. The stretching experiments were performed by changing the ambient temperature to three different levels, 162, 167 and 170°C, which were higher than the original T_g of PC (147.7°C). The nominal strain and strain rate were also changed to 40, 80 and 100 mm, (i.e., 200, 400 and 500) and 5, 40 and 80 mm min^{-1}, (i.e., 0.0042, 0.033 and 0.067 s^{-1}), respectively. Microcellular foaming is normally conducted at temperatures slightly higher than the T_g of the polymer, which would be reduced by the plasticization effect of CO_2. The strain rate exerted on the cell wall during bubble growth is approximately in the range of 0.01 to 1 s^{-1}.[16] To compare the nanoporous structure in the stretching process with that in the foaming process, the experimental temperature and the strain rate of the stretching experiments were determined by considering the foaming behaviors.

Our interest in this study was not to develop a model of the formation of nanoporous structures with the strain and strain rate, but to identify an analogy between the nanoporous structure induced by stretching and by foaming in terms of the effects of the strain and strain rate. Furthermore, due to the limitations of tensile machines, biaxial stretching tests could not be conducted, and only uniaxial stretching tests were used to form microvoids by crazing. The nanoporous structure formed by uniaxial stretching may not be exactly the same as that formed by biaxial stretching or that formed on cell wall of foams. However, it could be useful to identify an analogy between the stretching-induced nanoporous structure and the foaming-induced nanoporous structure.

4.2.3 CO_2+acetone foaming

The specified amount of liquid acetone was dropped into a high-pressure autoclave at room temperature. A 1 mm thick PC sample was then placed into the autoclave followed by CO_2 purging. The sample was suspended in the autoclave to prevent its direct contact with liquid acetone. Then, the sorption of CO_2+acetone was performed at the three acetone/CO_2 mole concentrations, 0, 1.0 and 2.83 mol%, while maintaining the pressure at 10 MPa, temperature at 60°C and sorption time at 22.3 h. At 60°C and 10 MPa, the mixtures of CO_2+acetone (0, 1.0 and 2.83 mol%) became supercritical.[17] The sorption time (22.3 h) was fixed to ensure that the PC matrix reached an equilibrium state with the CO_2+acetone mixture. Just after the sorption, the sample was placed on a hot press and foamed by heating at one of these temperatures: 80, 100, 110, 120, 140, 150, 160 and 170°C for 1 min. These foaming temperatures were higher than the boiling point of acetone. After foaming, the samples were measured by DSC, but

crystallinity could not be detected. To observe the cell morphology, the sample was immersed in icy water immediately after foaming so that bubble growth could be frozen.

4.2.4 Solubility and surface tension measurements

The solubility of CO_2 and acetone in the PC was measured as follows: the sample was first dried in a vacuum chamber for 2 days and carefully weighted after drying. The sample was then placed in a high-pressure autoclave and immersed in the CO_2+acetone mixture at 60°C 10 MPa for 22.3 h. The weight was measured before and after sorption to calculate the solubility of CO_2 and that of the CO_2-acetone mixture. The desorption behavior of CO_2 and acetone was also measured by occasionally weighing the samples while maintaining the samples in a refrigerator where the temperature was regulated at 4°C.

The surface tension of PC in the presence of CO_2 and acetone was measured using a pendant drop method. The details of the experimental scheme and the setup can be found elsewhere.[18] The measurements were conducted at four different pressures, 15, 16, 18 and 20 MPa, while maintaining the temperature at 240°C. The acetone concentrations in CO_2 were 3.07, 2.89, 2.57 and 2.31 mol% for 15, 16, 18 and 20 MPa, respectively.

4.2.5 Characterization of cell morphology

The morphology was observed by scanning electron microscopy (SEM, JSM-6700F, JEOL Japan), using a 10 kV acceleration voltage, 5 μA and a wide distance of 8 mm. The samples were frozen in liquid nitrogen to create cryogenic fractural surfaces and then coated with gold prior to SEM observation. The image processing software Image J

was used to calculate the cell density and the number average cell radius, $\overline{R_n}$. The solid and foam densities were measured using a densitometer (Mirage Electronic Densimeter MD-200S) and to calculate the cell density. The cell density with respect to the foamed polymer, N_f, was calculated as follows:

$$N_f = \left(\frac{n}{A}\right)^{1.5} \quad (1)$$

where n is the number of bubbles in a total area, A.

The cell density with respect to the solid polymer, N_o, was calculated as follows:[19]

$$N_o = \frac{\rho_s}{\rho_f}\left(\frac{n}{A}\right)^{1.5} \quad (2)$$

where ρ_f and ρ_s are the densities of the foam and solid bulk, respectively. Here, ρ_s / ρ_f is also known as the expansion ratio.

The pore density, N_p, and the number average pore radius, $\overline{R_p}$, on the cell wall were also calculated from the SEM micrographs at high magnification:

$$N_p = \frac{n_p}{A} \quad (3)$$

where n_p is the number of pores on the cell wall in a total area, A.

A gas pycnometer (AccuPyc, Shimadzu Corp.) was used to measure the volume of samples. The volume (V_{mea}), excluding the open pores, was measure by the gas pycnometer. The apparent volume of samples (V_{app}) was measured geometrically by using a caliper. Thus, the open-cell content (ε) and open-cell ratio (ε_r) were then calculated as follows:[20]

$$\varepsilon = \frac{V_{app} - V_{mea}}{V_{app}} \tag{4}$$

$$\varepsilon_r = \frac{\varepsilon}{1 - \rho_f / \rho_s} \tag{5}$$

The open-cell content (ε) indicates the volume fraction of open cells in a foam, and the open-cell ratio (ε_r) indicates the volume ratio of open cells to the total (open + closed) cells.

The thickness of cell wall (δ) was calculated as follows:[21]

$$\delta = d\left(\frac{1}{\sqrt{1 - \rho_f / \rho_s}} - 1\right) \tag{6}$$

where d is the average cell diameter.

4.3 Theory in Brief

4.3.1 Calculation of surface tension

To calculate the surface tension of PC in the presence of CO_2+acetone, the densities of PC with CO_2 as well as that with CO_2+acetone were needed.[22] Those densities were estimated by the mixing rule of the Sanchez-Lacombe equation of state with the characteristic parameters listed in Table 4.1:[23]

$$\tilde{\rho}^2 + \tilde{P} + \tilde{T}[\ln(1-\tilde{\rho}) + (1-1/r)\tilde{\rho}] = 0 \qquad (7)$$

where r is the segment number. $\tilde{\rho}$, $\tilde{P}$ and $\tilde{T}$ are the reduced density, pressure and temperature, respectively. They are defined as follows:

$$\tilde{\rho} = \rho/\rho^* \qquad \tilde{P} = P/P^* \qquad \tilde{T} = T/T^* \qquad (8)$$

where ρ, P and T are the density, pressure and temperature, respectively. ρ^*, P^* and T^* are the characteristic parameters. These parameters are summarized in Table 4.1.

Table 4.1 Characteristic parameters of the Sanchez-Lacombe equation of state for PC, CO_2 and acetone

	ρ^*[kg/m^3]	P^*[MPa]	T^*[K]
PC[24]	1276	496	802
CO_2[15]	1253	369	341
Acetone[25]	917	533	484

The parameters of binary mixtures are defined as follows:[18, 26]

$$r_i^0 = \frac{M_i P_i^*}{\rho_i^* R T_i^*} \qquad (9)$$

$$\phi_i^0 = \frac{r_i^0 n_i}{r_1^0 n_1 + r_2^0 n_2} \tag{10}$$

$$v^* = \phi_1^0 v_1^* + \phi_2^0 v_2^* \tag{11}$$

$$\phi_i = \phi_i^0 \frac{v_i^*}{v^*} \tag{12}$$

$$r_i = r_i^0 \frac{v_i^*}{v^*} \tag{13}$$

$$x_i = \frac{m_i / M_i}{m_1 / M_1 + m_2 / M_2} \tag{14}$$

$$r = r_1 x_1 + r_2 x_2 \tag{15}$$

$$X = \Delta P^* v^* / RT \tag{16}$$

$$v = v_1^* / v_2^* \tag{17}$$

$$T^* = (T_1^* \phi_1 + v T_2^* \phi_2) / (\phi_1 + v\phi_2) + \phi_1 \phi_2 XT \tag{18}$$

$$\rho^* = 1 / (m_1 / \rho_1^* + m_2 / \rho_2^*) \tag{19}$$

$$P^* = \phi_1 P_1^* + \phi_2 P_2^* - \phi_1 \phi_2 \Delta P^* \tag{20}$$

where *i=1* and *2* (components 1 and 2). *M* is the molar mass, and *R* is the gas constant. r_i^0 and r_i are the numbers of sites occupied by a molecule of species *i* in the pure state and in the mixture, respectively. n_i, ϕ_i, m_i and x_i are the number of moles, volume fraction, mass fraction and mole fraction of component *i*, respectively. v^* and v_i^* are the molar volumes of lattice sites of mixture and component *i*, respectively.

For a CO_2-acetone system, ΔP^* is calculated as follows:[15]

$$\Delta P^* = P_1^* + P_2^* - 2(1-\kappa_{12})(P_1^* P_2^*)^{1/2} \tag{21}$$

where κ_{12} is binary interaction parameter and the value of κ_{12} is 0.0128 for a CO_2+acetone system.[27]

For a polymer-gas system, subscripts 1 and 2 denote CO_2 and polymer, respectively. Because the interaction parameters of PC with CO_2 and acetone are unknown, the ΔP^* of CO_2 and polymers was approximated as follows:[26]

$$\Delta P^* = (\sqrt{P_1^*} - \sqrt{P_2^*})^2 \qquad (22)$$

4.4 Results and Discussion

4.4.1 Properties of PC in presence of CO_2+acetone

The solubility of CO_2 as well as that of the CO_2 and acetone mixture at 10 MPa and 60°C is listed in Table 4.2. After dissolving the CO_2+acetone mixture in polymer at 60°C and 10 MPa for 22.3 h, the PC sample was maintained at 4°C in a refrigerator to intentionally leach CO_2 and maintain the acetone in the polymer. Figure 4.1 shows the desorption behavior of the CO_2+acetone mixture from PC at 4°C. The weights of all samples were stabilized and remained constant after approximately 400 h. The weight gain did not reach zero even for the polymer/CO_2 system, where it reached approximately 0.36 wt%. The weight gain was caused either by residual CO_2 or water absorbed from humid air. Subtracting this final gain of the polymer/CO_2 system from the final gain of the polymer/(CO_2+acetone) system, the amount of acetone absorbed in PC was calculated as shown in the enlarged figure. The total solubility of the mixture in PC is correlated positively with the swelling effect.

Notably, the solubility of the CO_2+acetone (2.83 mol%) mixture was approximately 11 wt% in PC while that of CO_2 alone was 9.7 wt%. The solubility of CO_2 increased from 9.7 to 10.1 wt% as the acetone content was increased in the mixture. The solubility of acetone itself also correlated positively with the acetone concentration. The degree of the plasticization effect of supercritical CO_2+acetone fluid correlated positively with the acetone content in the mixture.

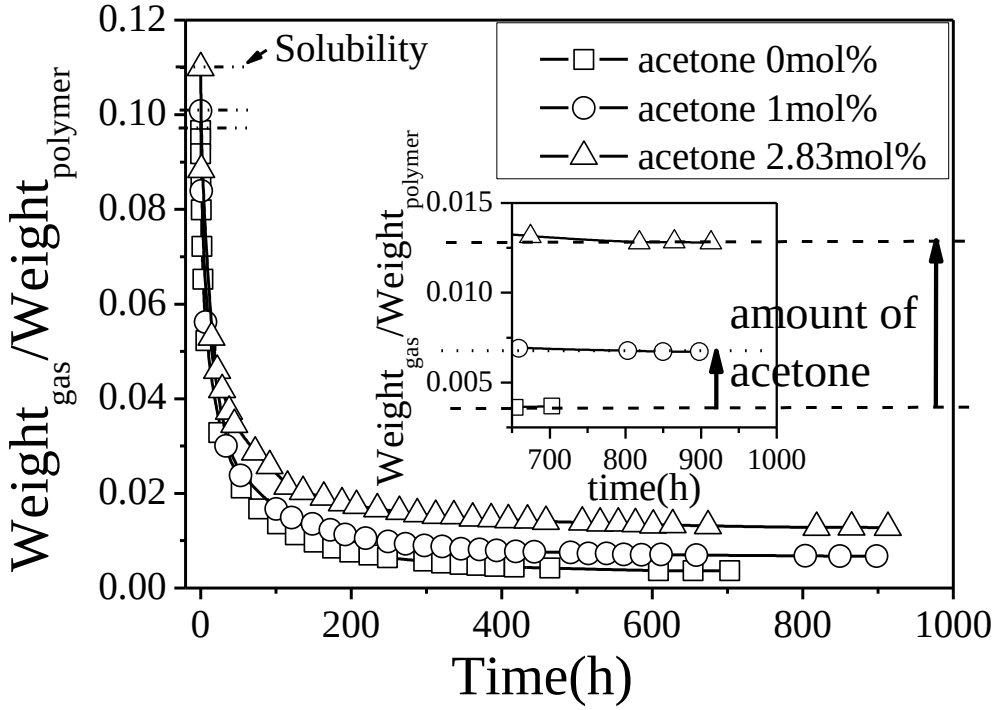

Figure 4.1 Amount of CO_2+acetone mixture in PC as a function of elapsed time

Table 4.2 Solubility of CO_2+acetone mixture in PC

Amount of acetone in the mixture (mol%)	Solubility of mixture in PC (g/g)		
	CO_2(wt%)	Acetone(wt%)	Total(wt%)
0%	9.7%	0%	9.7%
1%	9.8%	0.30%	10.1%
2.83%	10.1%	0.91%	11.0%

The surface tension of PC in supercritical CO_2+acetone fluid at 240°C and at various pressures was measured, and the resulting values are summarized in Figure 4.2. Wong et al. also measured the surface tension of PC in CO_2 at 240°C and 14.7 MPa using a sessile drop method, and their results are also plotted in Figure 4.2.[28] The surface tension of PC in the presence of CO_2 decreased from 19.1 to 17.6 mN m^{-1} as the pressure

increased from 15 to 20 MPa. CO_2 apparently increased the chain mobility of PC and softened the polymer. Similarly, the solubility of CO_2 in PC was further increased by the addition of acetone to CO_2, and the surface tension of PC in the presence of CO_2+acetone decreased to 17.8 mN m^{-1} at 15 MPa.

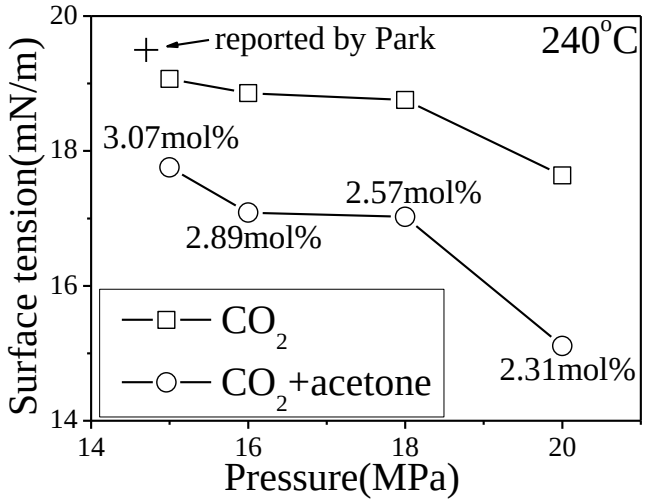

Figure 4.2 Surface tension of PC in supercritical CO_2 and CO_2+acetone fluids

4.4.2 Cell morphology of PC foams with CO_2+acetone

Figure 4.3 shows the SEM micrographs of the PC foams. The cell size and the cell density were calculated using Eq.(1) from the SEM micrograph, and the expansion ratio was calculated according to ρ_s / ρ_f . The results are illustrated in Figure 4.4. As the foaming temperature increased, the cell size became larger and the expansion ratio increased. When the cells impinged on each other, the cell shape tended to be polygonal. By comparing the cell size and expansion ratios of the PC/CO_2 system with those of the PC/(CO_2+acetone) systems, the addition of acetone to CO_2 clearly increased the cell size

and expansion ratio. This effect is apparent because the acetone in PC increases the solubility of CO_2 and enhances plasticization in PC.

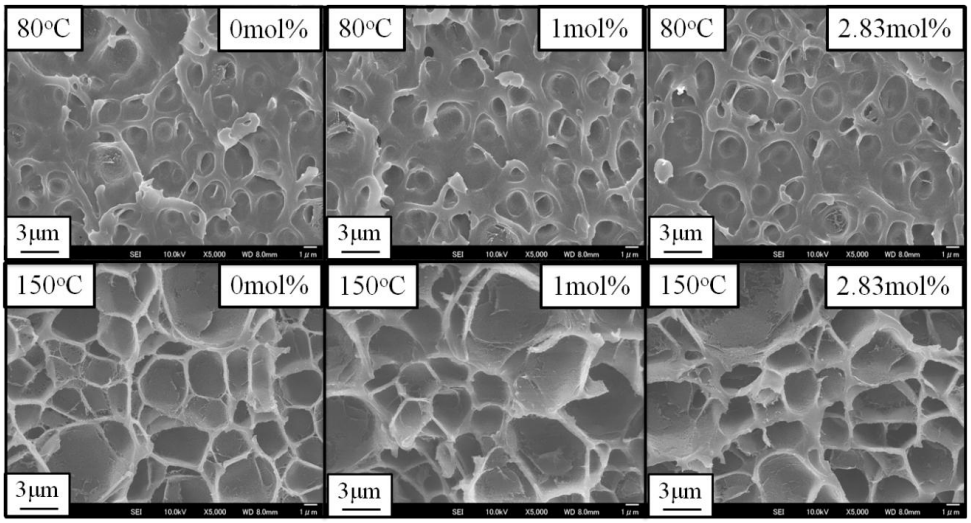

Figure 4.3 SEM micrographs of PC foamed at 80 and 150°C for 1 min after dissolving CO_2+acetone (0, 1, 2.83 mol% acetone concentration) mixture

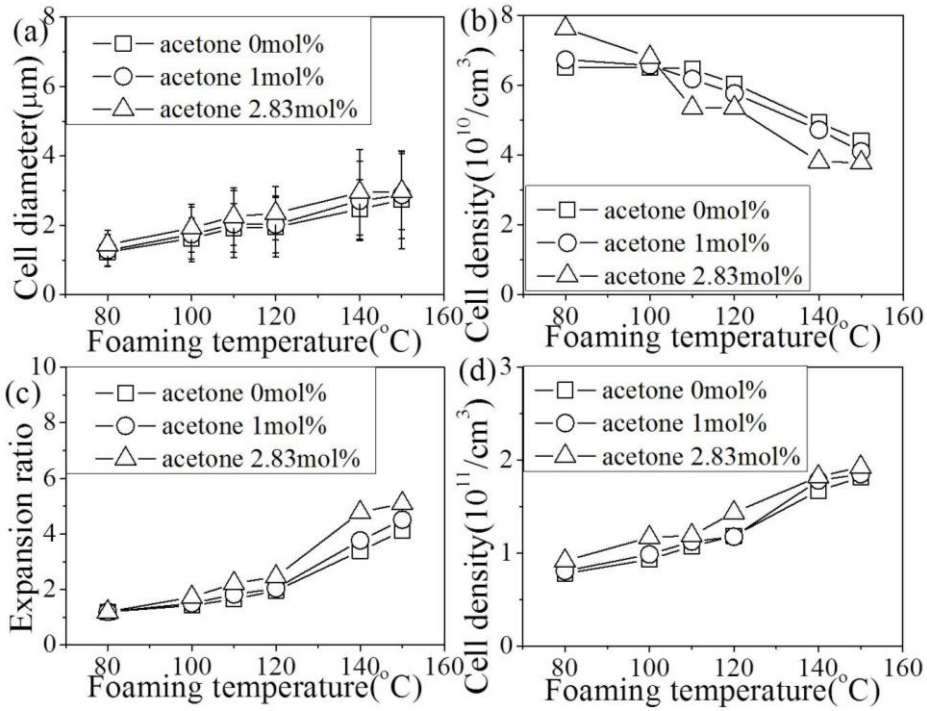

Figure 4.4 Cell diameter (a), cell density with respect to the foamed polymer (b), expansion ratio (c) and cell density with respect to the solid polymer (d) of the PC foams

The cell density per unit volume of foam, N_f, is shown in Figure 4.4 (b). The cell density negatively correlated with the average cell size. This relationship is often observed because the number of cells that can be observed in one micrograph of SEM reduces when the cell size increases. Figure 4.4 (d) shows the cell density per unit volume of a solid polymer, N_o. The cell density, N_o, correlated positively with the foaming temperature. A higher foaming temperature increased the degree of supersaturation and the cell density, N_o. Furthermore, the cell density, N_o, was increased by the addition of acetone into CO_2. As shown in the measurement of surface tension in presence of CO_2 and CO_2+acetone, the surface tension was lowered by CO_2 and acetone. The energy required for bubble nucleation was then decreased, and the nucleation was enhanced.

4.4.3 Nanoporous structure in stretching process

Figure 4.5 shows the fracture surface morphology of PC prepared by stretching. Small crack non-oriented patterns were observed in some of the micrographs. This pattern was due to the gold coating used to prepare the SEM samples. The sample prepared at 167°C with a strain rate of 40 mm min^{-1} and strain of 80 mm shows a strip pattern without microvoids. By reducing the strain rate from 40 to 5 mm min^{-1}, the strip pattern was not observed and the surface morphology was smooth. The strip pattern indicates significant molecular chain alignment and the fluctuations of chain concentration in the plastic zone. The increase of the strain rate from 40 to 60 mm min^{-1} promoted chain alignment and then created microvoids or nanoporous structure. Similarly, increasing strain from 40 to 100 mm enhanced the strip pattern and led to the

formation of a nanoporous structure. In this stretching process, the ambient temperatures were set to designated temperatures higher than the T_g of PC. Therefore, the chain relaxation occurs after stretching, and the chain orientation was relaxed. When the ambient temperature was 162°C, the chain orientation became dominant, the chain relaxation was suppressed and a nanoporous structure was formed. On the contrary, when the temperature was 170°C, the chain relaxation became dominant and the nanoporous structure disappeared.

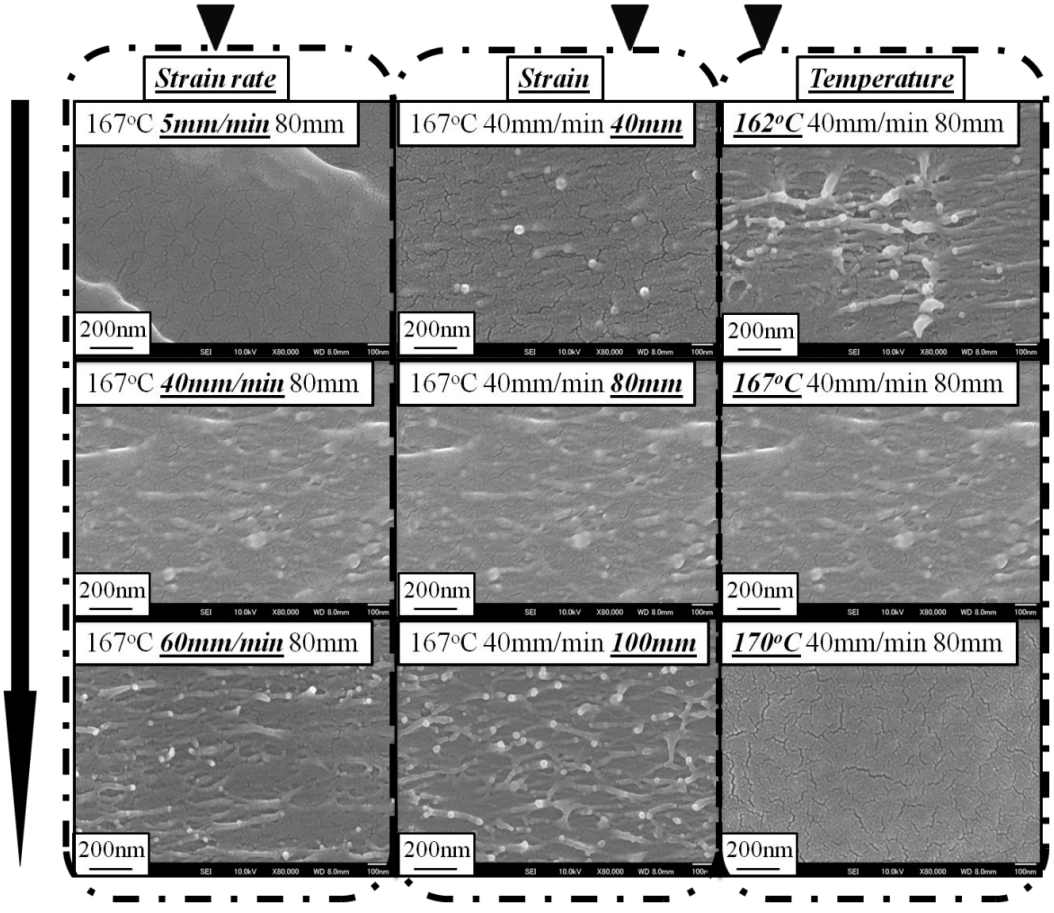

Figure 4.5 SEM micrographs of fracture surface of PC tensile specimens (stretching direction ←→)

4.4.4 Nanoporous structure in foaming process

Figure 4.6 shows micrographs of the morphology of the cell wall foamed at 120°C. When the foaming time was 2 s, the samples showed bubbles with smooth cell walls. When the foaming time was increased to 10 s, the cell wall underwent biaxial elongation and the walls began to show voids. Further increasing the foaming time to 1 min established a nanoporous structure, which can be clearly observed in Figure 4.6 (c). This result partly supports the mechanism proposed by Miller et al.: the nanoporous structure is induced at a subsequent stage after the initial bubble nucleation.[4] However, it is not a secondary nucleation induced by CO_2 because the mechanism of bubble nucleation in the polymer matrix and that of cavitation on the cell wall are quite different from each other. CO_2 may have assisted cavitation but does not lead to cavitation directly. The amount of CO_2 dissolved in the polymer matrix is commonly acknowledged to be insufficient for spinodal decomposition and expected to significantly decrease once bubble nucleation is induced by supersaturation. Consequently, inducing spinodal decomposition during CO_2 foaming is very difficult. Another mechanism proposed by Sorrentino et al. requires a fast decrease in the CO_2 concentration.[3] If this mechanism is accurate, cavitation should then have occurred simultaneously or immediately after bubble nucleation. Figure 4.6 (a) indicates that the cell wall was still smooth without any voids for a foaming time of 2 s, which occurred immediately after bubble nucleation.

After foaming the PC at 120°C with foaming time of 1 min, the foamed sample was placed in a vacuum chamber for 2 days to completely leach the dissolved CO_2. The sample was annealed at 170°C for 2 min to release the inner stress. The cell and the cell wall morphologies of the treated sample are shown in Figure 4.7 (a) and (b), respectively.

The nanoporous structure on the cell wall disappeared while the cells themselves remained. This effect is analogous to the phenomena observed during crazing, where microvoids could be erased by annealing at a temperature higher than the T_g. Annealing induces chain relaxation; the entanglement point is regenerated and the cell wall is smoothed.

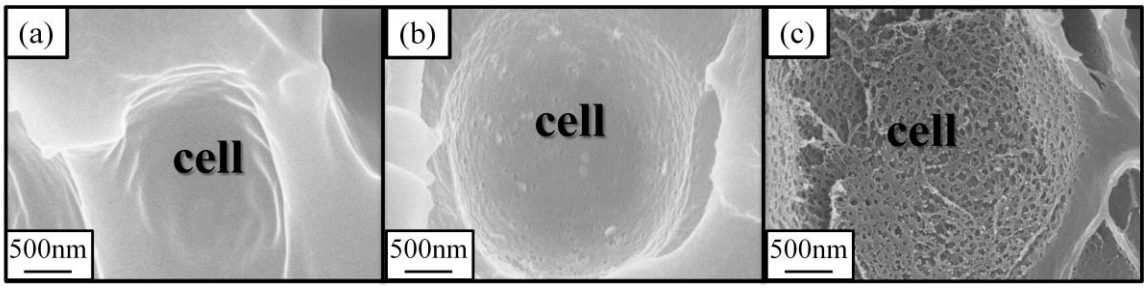

Figure 4.6 Cell wall morphologies of PC foams at a foaming time of 2 s (a), 10 s (b) and 1 min (c) (foaming temperature 120°C)

Fukasawa et al. speculated that the nanoporous structure on the cell wall was induced by crystallization.[2] However, if the formation of the nanoporous structure was related to crystals, the porous structure should have remained after annealing at 170°C. Furthermore, crystallization was not detected in any samples in our study, as shown in Figure 4.8. The noise of the DSC curves at approximately the T_g might be induced by nanopore collapse, while the noise at approximately 190°C might be induced by cell collapse. Therefore, the nanoporous structure in the foaming process is analogous to the microvoids induced by cavitation.

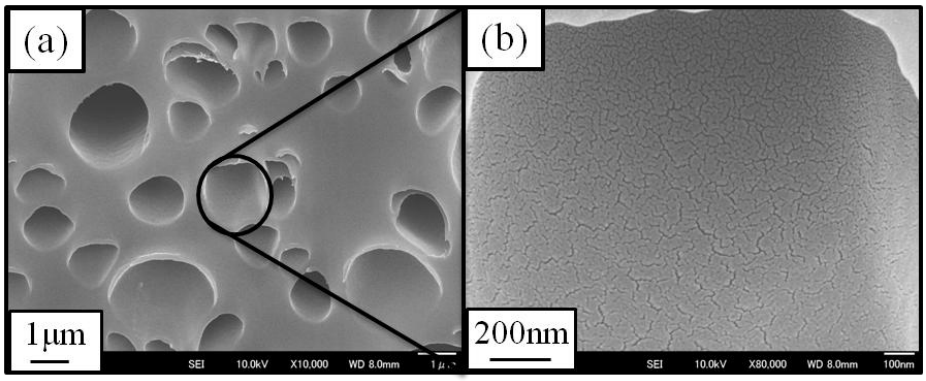

Figure 4.7 SEM micrographs of PC foamed at 120°C for 1 min first and then annealed at 170°C for 2 min (a). (b) is higher magnification.

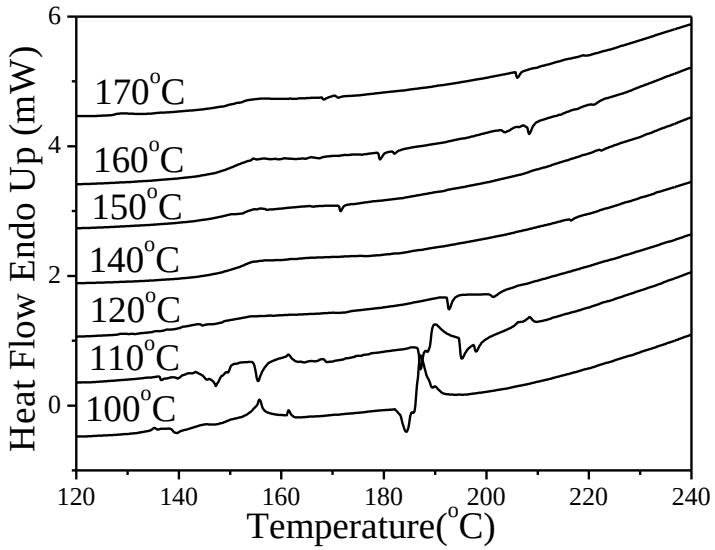

Figure 4.8 DSC heating curves of PC foamed at various temperatures for 1 min after dissolving CO_2+acetone (2.83 mol%) mixture

Figure 4.9 shows the micrographs of the nanoporous structure on the cell wall foamed at various temperatures. The nanopore size and density were measured from the SEM micrographs and the results are illustrated in Figure 4.10. The nanopore density, N_p, on the cell wall first increased and then decreased as the foaming temperature increased.

A nanopore structure could not be observed on the cell walls of samples foamed at 160°C after dissolving CO_2 and acetone or those foamed at 170°C after dissolving CO_2 alone. The nanoporous structure on the cell wall transformed to a fibril structure as the microvoids of craze grew and coalesced to form fibrils when the applied tension was sufficiently large. Figure 4.11 shows the SEM micrographs of cell walls foamed with CO_2 at 140°C. The nanopores on the cell wall subsequently grew, coalesced and transformed into fibrils.

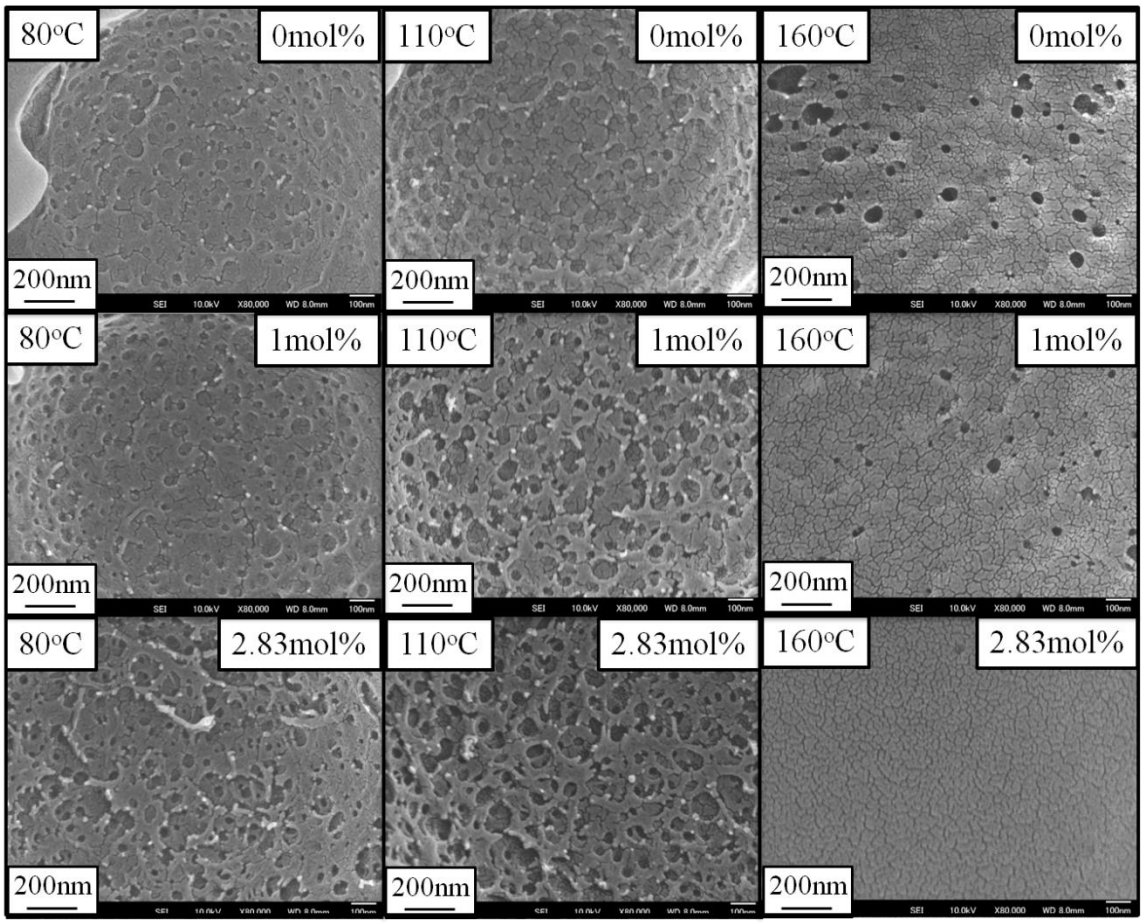

Figure 4.9 Nanoporous structure on the cell wall of PC foamed at 80, 110 and 160°C after dissolving CO_2+acetone (0, 1, 2.83 mol%) mixture (foaming time 1 min)

The expansion ratio, bubble growth rate and foaming temperature of the foaming process corresponded to the strain, strain rate and ambient temperature of the stretching process, respectively. If the nanopores from the foaming process are produced by stretching-induced cavitation or crazing, the pore size and pore density should be related to the expansion ratio, bubble growth rate and foaming temperature. For example, a larger expansion ratio or higher bubble growth rate should increase the degree of chain orientation and the nanopore density on cell wall. On the contrary, a higher temperature should accelerate the chain relaxation and decrease the degree of nanopore formation. Therefore, the degree of nanopore formation on the cell wall is determined by the competitive effects of two cause-and-effect relationships (Figure 4.12): the stretching-induced microvoid formation-temperature and the polymer chain relaxation-temperature (continuous and broken lines) relationships. The experimental results from this study clearly demonstrate these competitive effects of the foaming temperature, as shown in Figure 4.10.

Furthermore, the addition of acetone to CO_2 minimally increased the nanopore size and significantly increased the density, as shown in Figure 4.10. This addition also slightly shifted the nanopore density curve and foaming temperature relationship to lower temperatures. Acetone has been reported to act as a crazing agent, and the formation of stretching-induced microvoids or cavitational deformation is reportedly promoted by acetone.[14]. Analogous to the acetone effect on the formation of stretching-induced microvoids, the nanopore density on the cell wall of foams correlated positively with the acetone concentration in CO_2 (Figure 4.10 (b)).

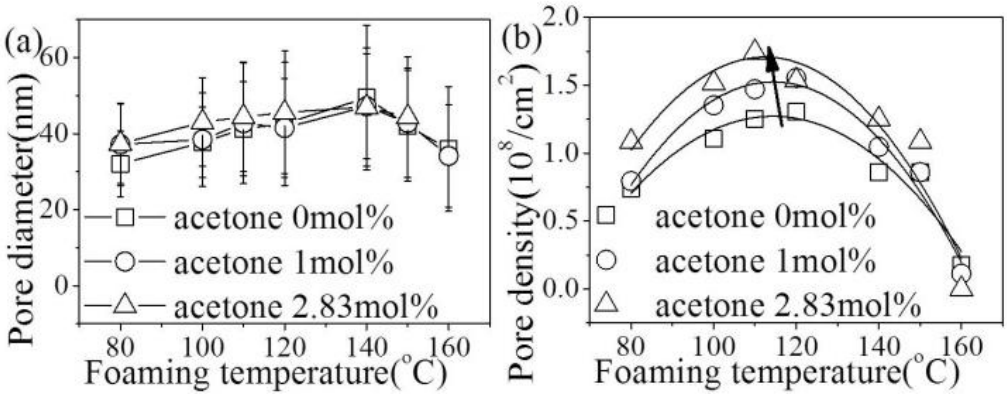

Figure 4.10 Pore size (a) and pore density (b) of nanoporous structure on the cell wall of PC foams

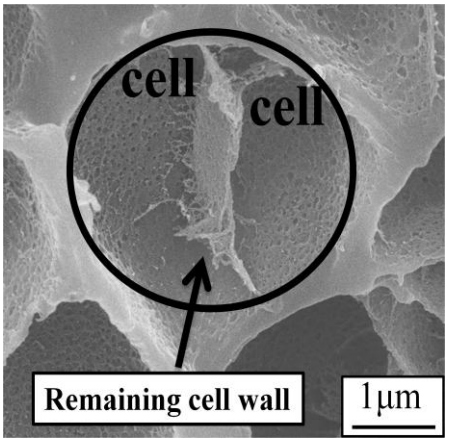

Figure 4.11 Cell coalescence of PC foam at 140°C

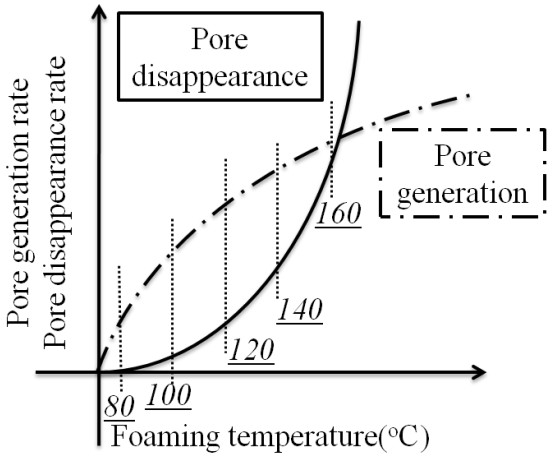

Figure 4.12 Schematic graph of pore generation rate and pore disappearance rate

4.4.5 Open-cell PC foams

When the cell walls significantly thinned, the nanopores could open the cell wall and the cell structure opened. Figure 4.13 shows the open-cell content (OCC) and open-cell ratio (OCR) of the foams. The OCC was less than 2% for the sample foamed at a temperature lower than 120°C. However, it increased to approximately 80% as the foaming temperature increased to 150°C. Further increasing the foaming temperature enhanced the relaxation of the polymer chain, advanced the deterioration of the nanoporous structure and increased the thickness of the cell wall. As a result, the OCC decreased. Figure 4.13 (b) clearly shows that the open-cell ratio directly depends on the thickness of the cell wall, but is independent of the pore density on the cell wall. This relationship may be attributed to the different pore morphology in the cell wall compared to that on the cell wall. Moreover, not all nanopores contribute to cell opening. When the cell walls were thicker than 0.75 μm, the OCR was low and did not significantly change. However, the OCR increased dramatically as the wall thickness decreased from 0.75 to 0.5 μm. When the wall thickness fell below 0.5 μm, the OCR reached 100%.

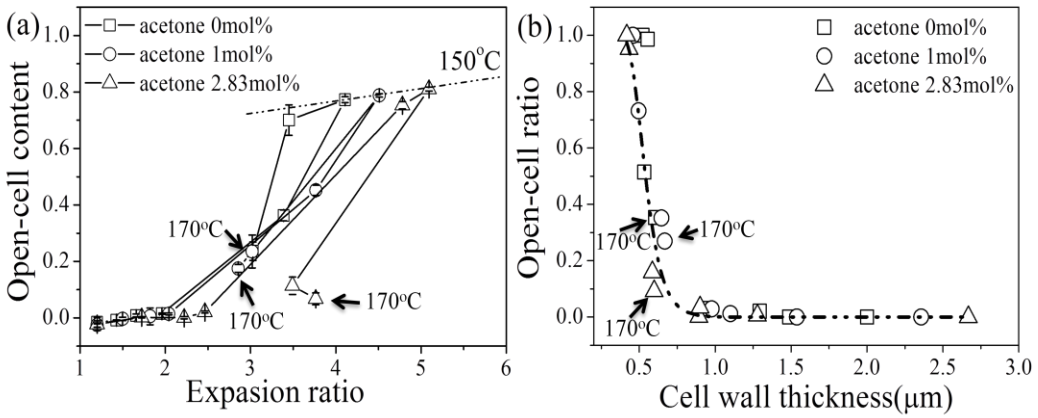

Figure 4.13 Open-cell content as a function of expansion ratio (a) and open-cell ratio as a function of cell wall thickness (b).

4.5 Conclusions

We observed the cell and cell wall morphologies of PC foams prepared with CO_2 and CO_2+acetone mixtures. The nanoporous structure on the cell wall of the foams prepared at low foaming temperatures with high expansion was observed. The changes in nanoporous structure as a function of the expansion ratio, bubble growth rate and foaming temperature in batch physical foaming processes were compared to those in the microvoids as a function of strain, strain rate and ambient temperature in the crazing process. The nanoporous structure of the PC foams could be considered a crazing structure induced by the elongation during the foaming process. The formation of the nanoporous structure on the cell wall was promoted by a large expansion ratio and fast bubble growth rate but inhibited by the polymer relaxation. The addition of acetone to CO_2 increased the solubility of CO_2 in PC and decreased the surface tension of PC. Therefore, acetone increased the cell size and cell density per unit volume of solid polymer. Furthermore, acetone acted as a crazing agent for PC. In other words, the formation of a nanoporous structure was facilitated by acetone. Open-cell PC foams with a nanoporous wall structure could be obtained when the cell walls were thinner than 0.75 μm.

4.6 References

1 Ruckdaschel, H.; Gutmann, P.; Altstadt, V.; Schmalz, H.; Muller, A. *Adv. Polym. Sci.* **2010**, 227, 199-252.

2 Fukasawa, Y.; Chen, J.; Saito, H. *J. Polym. Sci., Part B: Polym. Phys.* **2008**, 46, 843-846.

3 Sorrentino, L.; Aurilia, M.; Iannace, S. *Adv. Polym. Tech.* **2011**, 30, 234-243.

4 Miller, D.; Chatchaisucha, P.; Kumar, V. *Polymer*. **2009**, 50, 5576-5584.

5 Krause, B.; Boerrigter, M.E.; van der Vegt, N.F.A.; Strathmann, H.; Wessling, M. *J. Membr. Sci.* **2001**, 187, 181-192.

6 Kausch, H.H. *Crazing in Polymers, Vol. 2*. **1990**, Springer-Verlag Berlin Heidelberg.

7 Argon, A.S. *Polymer*. **2011**, 52, 2319-2327.

8 Kausch, H.H. *Crazing in Polymers, Vol. 1*. **1983**, Springer-Verlag Berlin Heidelberg.

9 Dettenmaier, M.; Kausch, H.H. *Polym. Bull.* **1980**, 3, 571-578.

10 Gensler, R.; Plummer, C.; Kausch, H.H.; Munstedt, H. *J. Mater. Sci.* **1997**, 32, 3037-3042.

11 Plummer, C.J.G.; Donald, A.M. *J. Polym. Sci., Part B: Polym. Phys.* **1989**, 27, 325-336.

12 Kirloskar, M.A.; Donovan, J.A. *Polym. Eng. Sci.* **1987**, 27, 124-130.

13 Miltz, J.; DiBenedetto, A.T.; Petrie, S. *J. Mater. Sci.* **1978**, 13, 2037-2040.

14 Thomas, E.L.; Israel, S.J. *J. Mater. Sci.* **1975**, 10, 1603-1607.

15 Taki, K.; Tabata, K.; Kihara, S.; Ohshima, M. *Polym. Eng. Sci.* **2006**, 46, 680-690.

16 Ohshima, M. *Saisentan plastic seikei kako series, Vol. 2*. **2013**, Plastic Age Tokyo.

17 Page, S.H.; Sumpter, S.R.; Goates, S.R.; Lee, M.L.; Dixon, D.J.; Johnston, K.P. *J. Supercrit. Fluids.* **1993**, 6, 95-101.

18 Taki, K.; Murakami, T.; Ohshima, M. *Asian Workshop on Polymer Processing in Singapore*, **2002**.

19 Park, C.B.; Lee, P.C.; Wang, J.; Padareva, V. *Cell. Polym.* **2006**, 25, 1-18.

20 Miyamoto, R.; Fukumori, M.; Shikuma, H.; Ohshima, M. *Proeedings of the Polymer Processing Society 28th Annual Meeting in Thailand,* **2012**.

21 Klempner, D.; Frisch, K.C. *Handbook of Polymeric Foams and Foam Technology.* **1991**, Oxford University Press.

22 Andreas, J.M.; Hauser, E.A.; Tucker, W.B. *J. Phys. Chem.* **1938**, 42, 1001-1019.

23 Sanchez, I.C.; Lacombe, R.H. *Macromolecules.* **1978**, 11, 1145-1156.

24 Kim, C.K.; Paul, D.R. *Polym. Eng. Sci.* **1994**, 34, 24-32.

25 Rodgers, P.A.; Sanchez, I.C. *J. Polym. Sci., Part B: Polym. Phys.* **1993**, 31, 273-277.

26 Doghieri, F.; Sarti, G.C. *Macromolecules.* **1996**, 29, 7885-7896.

27 Chen, J.; Wu, W.; Han, B.; Gao, L.; Mu, T.; Liu, Z.; Jiang, T.; Du, J. *J. Chem. Eng. Data.* **2003**, 48, 1544-1548.

28 Wong, A.; Leung, S.N.; Li, G.Y.G.; Park, C.B. *Ind. Eng. Chem. Res.* **2007**, 46, 7107-7116.

Chapter 5

OPEN-CELL PET/PC BLEND FOAMS

5.1 Introduction

Polymeric foams have versatile thermal and mechanical properties, and they can be applied to many plastic parts. The application depends on the cell morphology of the foams, which is characterized by the cell density, cell size, and open and/or closed-cell structures.[1] The polymeric foams used for construction, packaging, and heat insulation are commonly made of closed-cell foams.[2] The foams used for shock absorption, sound attenuation, battery separators, and cell-scaffolds for tissue engineering are normally made of open-cell foams. [3,4,5]

Several cell-opening strategies have been proposed in the field of physical foaming, such as creating high temperature differences between the surface and core of an extrudate, using mixed blowing agents to induce secondary nucleation and to change the cell densities, using interpolymer blending, and blending two polymers with different crystallization temperatures. [6,7,8,9,10] Lee et al. prepared open-cell foams from PE and PP blends by extrusion.[9] They proposed two strategies to open the cell wall of the thermoplastic polymer foams: i) The polymer blends were prepared so that their dispersed domains could be composed of a low-T_c (soft) polymer and the matrix could be composed of a high-T_c (hard) polymer. Cell opening was then initiated through the soft domains trapped between growing adjacent cells. ii) The polymer blends were prepared so that their dispersed domains could be composed of a high-T_c (hard) polymer and the

matrix could be composed of a low-T_c (soft) polymer. Cell opening was then initiated by debonding the interface between the hard domains and the soft matrix. Lee et al. incorporated a secondary blowing agent to further plasticize the soft regions so that the stiffness contrast between the hard and soft regions in the polymer blend could be intensified.[7] Kohlhoff et al. used an interpenetrating network structure to increase the stiffness contrast between the domain and matrix and prepared open cellular PLA-based blends, in which the monomer acted as another cell-opening agent.[8] To prepare open cellular homopolymer foams, the hard/soft inhomogeneity strategy could be extended to a crystalline/amorphous structure. Semi-crystalline polymers, such as PP, have a hard region in the crystallite and a soft region in the amorphous area. Miyamoto et al. used a crystalline nucleating agent for PP to form three-dimensional network of highly connected nano-fibrils by foaming.[11] The network maintained the cellular size at the nano/microscale level and opened the cell walls by debonding the lamellae from the inter-lamellar amorphous region. Another cell-opening method was reported by Krause et al.[12] They prepared an open cellular PSU film using CO_2 and tetrahydrofuran (THF) as a blowing agent. During foaming, the cell wall thickness fluctuated, and the degree of fluctuation was facilitated by THF. Consequently, the cell walls were open, and the foam featured nanopores. The authors extended their study to obtain open nanoporous polymers and polymeric blends by CO_2 foaming.[13,14] Their open nanoporous morphology on the cell wall seemed to be a function of cell wall stretching and certain inhomogeneities in the structural or physical properties. However, the relationship was not clarified, and the mechanism of transition from closed to open cells remained uncertain.

Cell sizes have also been reduced in the foaming industry for the production of microcellular foams. The prevention of cell coalescence was one of the key factors in reducing the cell size. Cell coalescence and cell size in physical foaming are commonly reduced by increasing the viscosity of the matrix polymer and enhancing the strain hardening behavior. Li et al. numerically simulated polymer foaming to study the dynamics and stability of bubble growth.[15] They found that the stability of bubbles was controlled by the strain hardening characteristics and elastic properties of the polymers. Cross-linking agents and highly viscous components have been used and proven effective to increase the viscoelasticity and suppress cell coalescence.[16,17] Carbon nanotube, nanoclay and long-chain branched polymers could also be used to control the viscoelasticity and reduce the cell size.[18,19,20] They can orient the polymer chains in biaxial elongational flow and increase viscoelasticity locally at the cell wall. To produce open porous microcellular foam, the cell size is reduced while simultaneously opening or rupturing the cell wall. The increase in viscoelasticity and introduction of strain hardening behavior or local polymer orientation can reduce the cell size but might not enhance cell opening. A different strategy is necessary to reduce the cell size, increase the cell density and simultaneously enhance the degree of cell opening.

In this study, the heterogeneous interface was focused on as the site for cell opening. Instead of making the clear contrast between soft and hard domains in the polymer blends, the interfacial properties between the two domains were obscured for cell opening and microcellular foaming. The effect of the interfacial properties on the bubble nucleation was investigated in Chapter 2. Decreasing the interfacial tension between the domain and matrix polymers increased the compatibility between two

polymers and increased the interfacial area, which increased the number of heterogeneous nucleation sites. Conversely, decreasing the interfacial tension reduced the heterogeneity between the domain and matrix polymers and suppressed the bubble nucleation rate at the interface. Therefore, decreasing the interfacial tension provided positive and negative effects on bubble nucleation. The effect of interfacial properties on the bubble growth was then investigated in Chapter 3. PET domains were easily detached from the PC matrix in bubbles due to the weak interfacial affinity between the domain and matrix polymers. Decreasing the interfacial tension increased the interfacial affinity and led to a fibril structure that connected the semi-crystalline domains and matrix polymers. Furthermore, it was found in Chapter 4 that the nanoporous structure on the cell wall led to open-cell PC foams when the cell walls were thinner than 0.75 μm. Consequently, an optimal interfacial property may exist for microcellular foam with a high open-cell ratio.

Interface modification is a common method for controlling the interfacial tension and blend morphology. In this study, PET/PC blends were used to prepare the open porous microcellular foam. In our system, PET dispersed domains were used as bubble nucleating agents. The miscibility between PET and PC was changed by a copolymer produced during the transesterification reaction. The presence of a copolymer at the interface can locally reduce the polymer viscoelasticity at the interface, facilitate stretching and open the cell wall around the PET domains with a fibrillated structure. The fibrillation at the interface may also lead to a stretch-induced void formation mechanism, which increases the cell density. Therefore, a novel method was reported in this study to control CO_2 foaming with optimal interfacial properties to achieve a designated foam morphology, such as small cell size, large cell density and large open-cell ratio.

5.2 Experimental

5.2.1 Materials

PC (Idemitsu, Taflon A2600, M_w=32,000, MFR=6 g 10-min^{-1} (300°C 1.2 kg)) and PET (Mitsui Chemical, J125, M_w=56,000, inherent viscosity=0.75 dl g^{-1}) were used as received. CO_2 (99.95% purity, Showa-Tansan, Japan) was used as the physical foaming agent.

5.2.2 Preparation of PET/PC blends

PET and PC pellets were dried in a vacuum oven at room temperature for at least 2 days. They were dry-mixed at two different weight ratios of PET to PC (10/90 and 30/70) and fed into a melt mixer (Labo Plastomill, 4C150 Toyoseiki, Japan). After melt blending, the PET/PC blend was placed in a vacuum oven for another 2 days to remove moisture. The blend was then annealed in an oven at 280°C for two different time periods (1 and 5 h) with a nitrogen purge (heat-annealing process). The transesterification degree was controlled by changing the heat-annealing time. The transesterification reaction can be accelerated by a variety of catalysts, such as lanthanides, titanium, and calcium/antimony.[21,22,23] However, the residual catalysis in PET could carry out the reaction in this study. Therefore, no external catalyst was introduced into our system. Because the PET domain could aggregate when PET/PC 30/70 wt% blends were heat-annealed, the blends were again melt-mixed to increase the dispersion of the PET domains in PC. The sample ID., heat-annealing times and weight ratios of PET/PC blends are summarized in Table 5.1.

The first melt-mixing was conducted at 270°C by rotating a kneading rotor at 10 rpm for the first 2 min. The rotation speed was then increased to 50 rpm for the next 8 min. The second melt-mixing was conducted at 10 rpm for 2 min, followed by 50 rpm for 3 min. After mixing, the blends were molded into a plate shape using a hot compression molding machine.

Table 5.1 Weight ratio, heat-annealing time and sample ID. of PET/PC blends

Blend ratio	Heat-annealing time	Sample ID.
PET/PC	0 h	A0
30/70	1 h	A1
	5 h	A5
PET/PC	0 h	B0
10/90	1 h	B1
	5 h	B5

5.2.3 CO_2 foaming

The PET/PC blend samples were placed in a high-pressure autoclave to dissolve the CO_2 at 10 MPa for 22.3 h at 60°C. After removing the sample from the autoclave without foaming, it was immediately placed on an aluminum plate and foamed on the hot press by heating for 1 min at three different foaming temperatures: 80, 120 and 150°C. The sorption time was fixed at 22.3 h to ensure that all blends reached an equilibrium state with CO_2.

5.2.4 Characterization of PET/PC blend rheological properties and crystallinity

The rheological properties were measured using a rheometer (Advanced Rheometric Expansion System, ARES, TA Instruments, USA): Rectangular torsion

geometry was used to conduct dynamic temperature ramp tests from 40 to 200°C at a heating rate of 2°C min^{-1}. The constant oscillation frequency of the torsion bar was set to 1 rad s^{-1} with 0.1% constant strain. G'' was measured and used to identify the glass transition temperature (T_g) of neat PET (T_{gPET}), neat PC (T_{gPC}), and the PET domain ($T_g^{'}$) and PC matrix ($T_g^{''}$) in blends. Rectangular torsion geometry was also used for the dynamic frequency sweep tests at temperatures below 200°C in the frequency range of 0.01-100 rad s^{-1}. The strain was set in the range of 0.1-0.4%. When the measurement temperature was higher than 200°C, the parallel plate geometry was used for the dynamic frequency sweep tests at strains of 5-15%. Prior to the dynamic frequency sweep tests, a strain sweep test was conducted to determine the strain limit for a linear viscoelastic response. A master curve of the G'-frequency was then obtained at 150°C. To calculate the interfacial tension, the blends were first placed between two parallel plates at 260°C for 5 min to completely melt the crystals in the PET domains. The blends then underwent dynamic frequency sweep tests at 250°C. The blends were confirmed to remain amorphous during the tests. The extensional viscosity (uniaxial extensional viscosity) was measured with a fixture. Four strain rates, 0.1, 0.2, 0.5 and 1.0 s^{-1}, were applied to PC, A0 and A1 at 240°C. The testing temperature for sample A5 was set to 220°C to prevent the sample from sagging during the measurement. The samples for the rectangular torsion test were approximately 10 mm in width, 1 mm in thickness and 40 mm in length. The samples for the parallel plate test were 25 mm in diameter and 2 mm in thickness. The geometry for the samples for the uniaxial elongational viscosity measurement was 18 mm × 10 mm × 0.7 mm. A differential scanning calorimeter (DSC: Pyris 1 Perkin Elmer) was used to measure the crystallinity of the PET domain in the

blend polymer and the neat PET. The sample was heated from 40 to 280°C at a rate of 10°C min^{-1}. The crystallinity was calculated using 140 J g^{-1} as the heat of fusion of 100% crystalline PET.

With the exception of samples used to measuring T_g and the interfacial tension, all samples were CO_2-annealed at 60°C and 10 MPa for 22.3 h so that the condition of the samples was analogous to that prior to foaming.

5.2.5 Characterization of blend and foam morphology

Scanning electron microscopy (SEM) was used to observe the blend and cell morphology of the foam. The samples were frozen in liquid nitrogen to create cryogenic fractural surfaces and then coated with gold for 180 s before observation under a SEM (Tiny-SEM 1540, Technex Co. Ltd., Japan) or field emission SEM (JSM-6700F, Jeol, Japan). FESEM images were collected at an acceleration voltage of 10 kV, a current of 5 μA and a wide distance of 8 mm. The image processing software Image J was used to calculate the dispersed domain density, N_d, and the number average domain radius, $\overline{R_d}$, from the SEM micrographs.

$$\overline{R_d} = \frac{1}{c}\sum_i^c R_i \qquad (1)$$

$$N_d = \frac{\phi}{\overline{V_c}} = \frac{\phi}{\frac{4}{3c}\pi\sum_i^c R_i^3} \qquad (2)$$

where R_i is the radius of the i-th domain measured from the SEM micrographs. $\overline{R_d}$ is the average domain radius. ϕ is the volume fraction of the dispersed domain, and it is calculated from the weight ratios and densities of both polymers.

The interfacial area between the dispersed domain and the matrix per unit volume of blend, *S*, is calculated by:

$$S = N_d \overline{S_d} = N_d \frac{4}{c} \pi \sum_i^c R_i^2 \quad (3)$$

where $\overline{S_d}$ is the number average domain surface.

The cell density with respect to the solid polymer, N_f, and the number average cell radius, $\overline{R_n}$, were also calculated from the SEM micrographs. The bulk densities of the samples before and after foaming were measured by a densitometer (Mirage Electronic Densimeter MD-200S) and were used to calculate the cell density. The cell density with respect to the solid polymer was then calculated by the following:[24]

$$N_o = \frac{\rho_s}{\rho_f} \left(\frac{n}{A} \right)^{1.5} \quad (4)$$

where *n* is the number of bubbles in a total area, *A*. ρ_f and ρ_s are the densities of the foam and the solid bulk, respectively. Here, ρ_s / ρ_f is also known as the foam expansion ratio.

A gas pycnometer (AccuPyc, Shimadzu Corp.) was used to measure the volume of samples. The volume (V_{mea}), excluding the open pores, was measured by the gas pycnometer. The apparent volume of the samples (V_{app}) was measured geometrically using a caliper. Thus, the open-cell content (ε) and open-cell ratio (ε_r) were then calculated by the following:[11]

$$\varepsilon = \frac{V_{app} - V_{mea}}{V_{app}} \quad (5)$$

$$\varepsilon_r = \frac{\varepsilon}{1 - \rho_f / \rho_s} \quad (6)$$

The open-cell content (ε) indicates the volume fraction of open cells in the foam, and the open-cell ratio (ε_r) indicates the volume ratio of open cells to total (open + closed) cells.

The thickness of the cell wall (δ) was calculated by the following:[2]

$$\delta = d\left(\frac{1}{\sqrt{1 - \rho_f / \rho_s}} - 1\right) \quad (7)$$

where *d* is the average cell diameter.

5.3 Theory of Blend Characterization in Brief

5.3.1 Component of fraction from the Fox equation

The T_g of a miscible polymer blend can be estimated by the Fox equation. When the equation is applied to partially miscible polymer blends, the minor polymer is commonly assumed to homogeneously infuse the major polymer phase. With this assumption, we applied the Fox equation to the PET/PC blends to estimate the weight fraction of PET in the PC matrix and that of PC in PET.[25,26]

$$\frac{1}{T_g^{'}} = \frac{\omega_{PET}^{'}}{T_{gPET}} + \frac{\omega_{PC}^{'}}{T_{gPC}} \tag{8}$$

and

$$\frac{1}{T_g^{''}} = \frac{\omega_{PET}^{''}}{T_{gPET}} + \frac{\omega_{PC}^{''}}{T_{gPC}} \tag{9}$$

where $\omega_{PC}^{'}$ is the weight fraction of PC infused in the PET domain and $\omega_{PET}^{'}$ (:=1- $\omega_{PC}^{'}$) is the weight fraction of PET in the PET domain. $\omega_{PET}^{''}$ (:=1- $\omega_{PC}^{''}$) is the weight fraction of PET in the PC matrix, and $\omega_{PC}^{''}$ is the PC weight fraction in the PC matrix. $T_g^{'}$ and $T_g^{''}$ are the glass transition temperatures of the PET domain and the PC matrix, respectively. T_{gPET} and T_{gPC} are the glass transition temperatures of the neat PET and the neat PC, respectively.

The weight fractions of PC in the PET domain and of PET in the PC matrix were calculated using Eqs. (10) and (11) with the T_g data of the blend and the neat polymers.

$$\omega_{PC}^{'} = \frac{T_{gPC}(T_{gPET} - T_g^{'})}{T_g^{'}(T_{gPET} - T_{gPC})} \qquad = 1 - \omega_{PET}^{'} \tag{10}$$

and

$$\omega_{PET}^{''} = \frac{T_{gPET}(T_{gPC} - T_g^{''})}{T_g^{''}(T_{gPC} - T_{gPET})} \qquad = 1 - \omega_{PC}^{''} \tag{11}$$

Furthermore, the weight fractions of both the PET domain and the PC matrix could be calculated from mass balance equations, which can be derived by transforming Eqs. (10)-(11)

$$\omega^{'} = \frac{\omega_{PC} - \omega_{PC}^{''}}{\omega_{PC}^{'} - \omega_{PC}^{''}} \tag{12}$$

and

$$\omega^{''} = \frac{\omega_{PC} - \omega_{PC}^{'}}{\omega_{PC}^{''} - \omega_{PC}^{'}} \tag{13}$$

where $\omega^{'}$ is the estimate of the weight fraction of the PET domain, $\omega^{''}$ is the estimate of the weight fraction of the PC matrix in the blend after transesterification reaction and ω_{PC} is the weight fraction (70% or 90%) of the PC matrix in the blend before transesterification reaction.[25,26]

5.3.2 Estimate of interfacial tension

About the content in this part, please refer to Chapter 2.

5.4 Results and Discussion

5.4.1 Characterization of blend properties

Figure 5.1 shows the shear loss moduli (G'') of the PET/PC blends with a 30/70 blend ratio. The T_g of the polymer was determined by the temperature at which the G''-temperature curve reached a peak.[27] The measured T_g of the neat PET and PC were 70.4°C and 147.7°C, respectively. The T_g of the PET-dispersed domains in the blend, denoted $T_g^{'}$, increased from that of neat PET to 79.1°C. The T_g of the PC matrix, $T_g^{''}$, decreased from that of neat PC to 124.4°C by mixing and heat annealing. The miscibility between PET and PC was increased at the interface by the presence of the PET-b-PC copolymer. Therefore, the two T_g values approached one another. The copolymer was produced by a transesterification reaction and was characterized by NMR and FTIR in Chapter 3. The Fox equation was applied by assuming that the PET segment of the copolymer infuses and uniformly disperses into the PC matrix and that the PC segment also infuses into the PET domain. This equation was then used to estimate the weight fraction of PET that infused the PC matrix and the weight fraction of PC that infused the dispersed PET domains. The calculated weight fractions are listed in Table 5.2. The details of the calculations are given elsewhere.[28,26] By conducting the transesterification reaction at 280°C, the degrees of PET segment infusion into the PC matrix and of PC infusion into the PET-dispersed domains both increased. The weight fractions of the PET domains and PC matrix were obtained from Eqs. (12) and (13) and used to calculate the crystallinity of the PET domains, domain density, and interfacial area between the PET domains and the PC matrix.

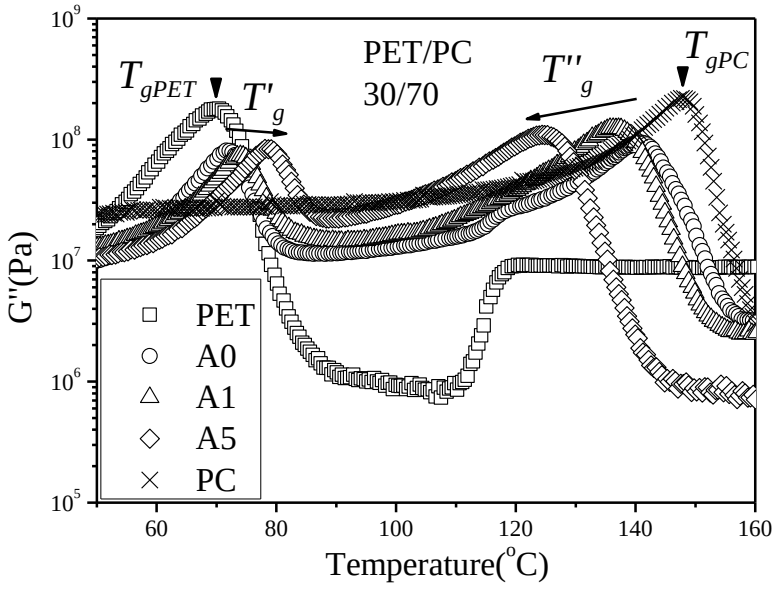

Figure 5.1 Shear loss moduli (G'') of PET, PC and 30/70 wt% PET/PC blends (A0, A1 and A5)

Table 5.2 T_g and the estimated weight percentage of PET and PC in the PET domain and PC matrix of the PET/PC blends

PET/PC		PET domain				PC matrix			
		$T_g^{'}$ (°C)	$\omega_{PET}^{'}$	$\omega_{PC}^{'}$	$\omega^{'}$	$T_g^{''}$ (°C)	$\omega_{PET}^{''}$	$\omega_{PC}^{''}$	$\omega^{''}$
30/70	**A0**	71.7	96.7%	3.3%	27.5%	140.5	4.6%	95.4%	72.5%
	A1	74.0	90.9%	9.1%	26.9%	136.3	7.6%	92.4%	73.1%
	A5	79.1	79.0%	21.0%	20.8%	124.4	17.1%	82.9%	79.2%
10/90	**B0**	72.5	94.6%	5.4%	8.0%	143.6	2.6%	97.4%	92.0%
	B1	73.9	91.1%	8.9%	7.1%	141.8	3.8%	96.2%	92.9%
	B5	75.9	86.2%	13.8%	3.3%	136.6	7.4%	92.6%	96.7%

Figure 5.2 shows the SEM micrographs of the PET/PC blend with a 30/70 blend ratio. A sea-island morphology was observed in most of the blends. The dispersed

domains consisted of PET, whereas the matrix consisted of PC. The domain size decreased as the heat-annealing time increased for the blend with a 30/70 PET/PC blend ratio. The rheological data of the blends indicates that a longer heat-annealing time could produce more copolymer and increase the miscibility between the PET domains and the PC matrix. Consequently, the diameter of the domains decreased.

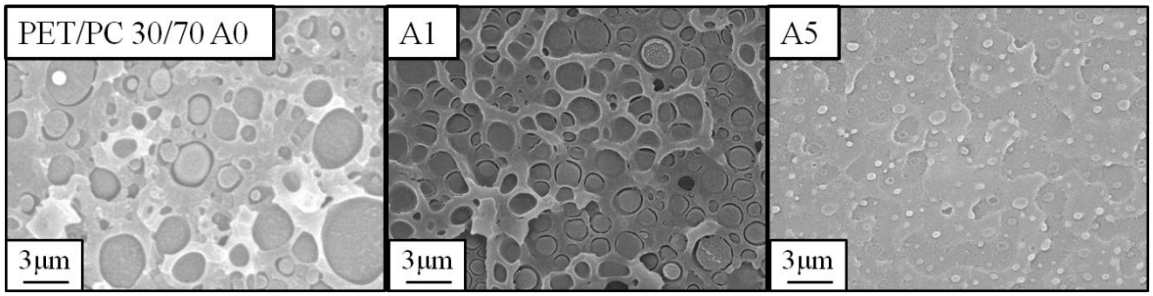

Figure 5.2 SEM Morphology of the 30/70 wt% (A0, A1 and A5) PET/PC blends

The domain size was measured and used to calculate the interfacial tension. The values of the interfacial tension are given in Table 5.3. The interfacial tension was determined by fitting the Palierne model to the experimental data of the storage and loss moduli. Figure 5.3 shows the experimental data and the model estimates for the PET/PC blends with a 30/70 blend ratio. The validity of the Palierne model was confirmed in our previous study on PMMA/PC and PMMA/PP blends in Chapter 2. The model also agreed well with the experimental data for the PET/PC blends. The non-heat-annealed PET/PC blend, A0, exhibited the largest interfacial tension, 2.3 mN m^{-1}, and blends A5 and B5 showed the smallest interfacial tensions, less than 0.01 mN m^{-1}. The interfacial tension inversely correlated with the heat-annealing time in both the 30/70 and 10/90 blends.

Table 5.3 Interfacial tension calculated using the Palierne model

Blend component		Interfacial tension(mN/m)
PET/PC	A0	2.3
	A1	0.647
30/70	A5	0.01
PET/PC	B0	1.1
	B1	0.21
10/90	B5	0.008

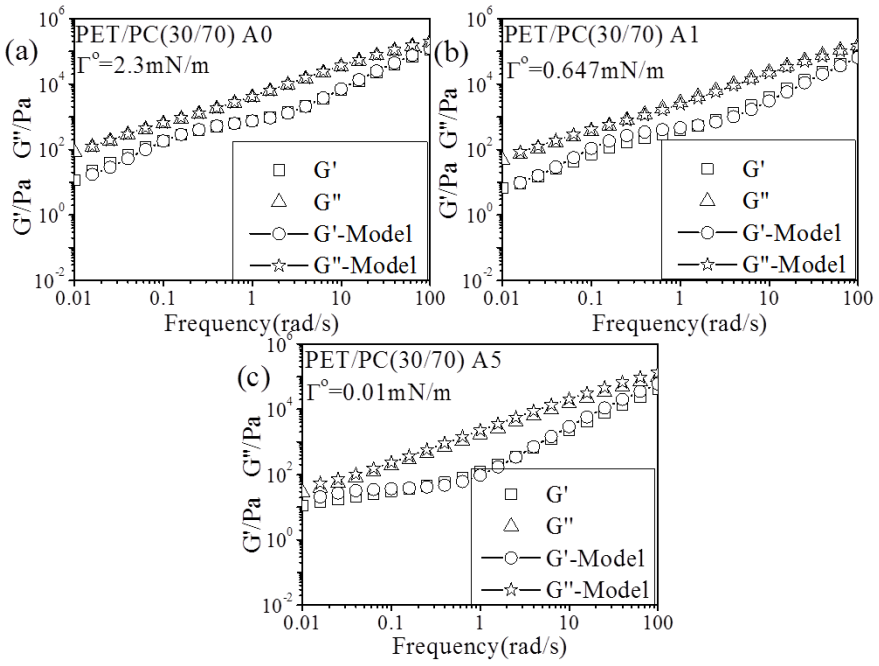

Figure 5.3 Estimates of the Palierne model and experimental data of the dynamic modulus

The domain diameter, $2\times\overline{R_d}$, the domain density, N_d, and the interfacial area per unit blend volume, S, were measured from SEM micrographs and calculated using Eqs. (1)-(3). The calculated values were plotted as a function of the interfacial tension, as shown in Figure 5.4. For PET/PC with a blend ratio of 30/70 (i.e., the A series), the size

of the PET-dispersed domains decreased from approximately 1.2 μm to 400 nm, the domain density and the interfacial area per unit volume of polymer blend increased as a result of the decreasing interfacial tension. In other words, the compatibility, uniformity and dispersion of the PET domains in the blend were drastically improved by increasing the copolymer, i.e., increasing the heat-annealing time. In contrast, the PET domain size was 300 nm without heat annealing for PET/PC with a blend ratio of 10/90 (i.e., B0), and it did not change with the decrease in interfacial tension, as shown in Figure 5.4-a. Furthermore, the domain density and the interfacial areas per unit volume of the polymer blend showed results opposite to those of the PET/PC blend with a 30/70 blend ratio (Figure 5.4-b and c): the domain density and interfacial area both decreased when the interfacial tension decreased. Because of the low volume fraction of PET in the 10/90 wt% PET/PC blends (Table 5.2), the PET domains could be well dispersed without heat annealing. The amount of copolymer correlated positively with the heat-annealing time. However, increasing the amount of copolymer enhanced the infusion of PET segments into the PC matrix rather than improving the PET domain dispersion and uniformity in the blend. As the heat-annealing time increased and the interfacial tension decreased, the small PET domains tended to disappear because PET was transformed into the copolymer, which was infused into the PC matrix. Therefore, both the PET domain density and the interfacial area per unit volume of the blend polymer decreased in the 10/90 wt% PET/PC blends as the interfacial tension decreased.

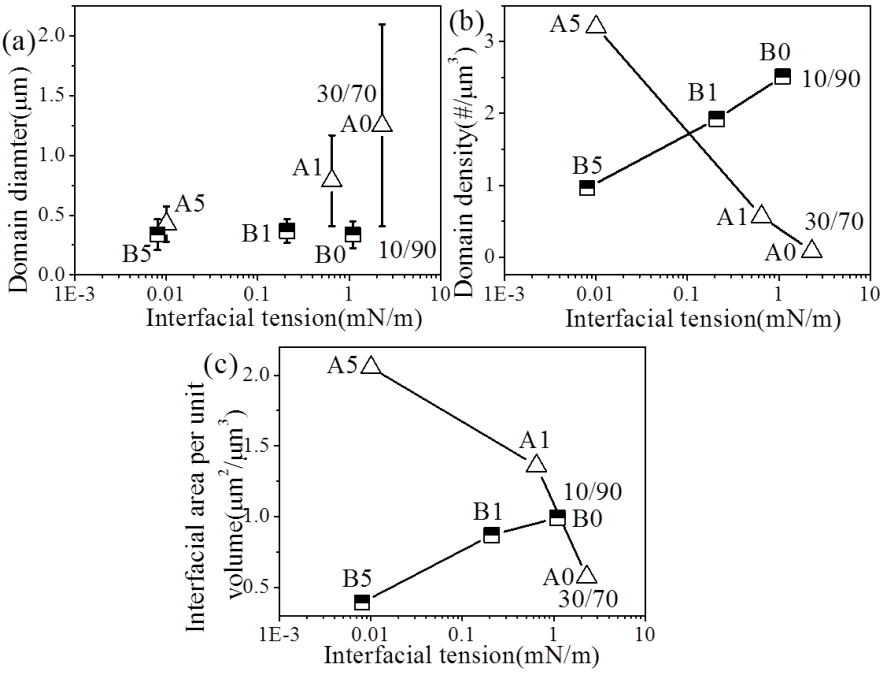

Figure 5.4 Number average domain diameter, $2\times\overline{R_d}$ (a), the dispersed domain density, N_d (b) and the interfacial area per unit blend volume, S (c) of the PET/PC blends

Figure 5.5 shows the DSC curves of the neat PET and PET/PC blends with a 30/70 wt% blend ratio annealed under 10 MPa-CO_2 at 60°C for 22.3 h. The thermal properties measured by DSC are summarized in Table 5.4. The PET crystallized even though the CO_2-annealing temperature for A0, A1 and A5 was lower than the glass transition temperatures of the neat PET and the PET phase in the blends. This crystallization can be attributed to the plasticization effect of CO_2. Two peaks were detected in both the neat PET and blends (A0, A1). When the neat PET and its blends were CO_2-annealed, a secondary crystallization occurred, which was detected by the peak of the heat curve at approximately 110°C. The peaks of the secondary and primary crystals were, respectively denoted T_{m2} and T_{m3} in Figure 5.5. As shown in Table 5.4, the

enthalpy of fusion of the primary crystals, ΔH_3, decreased as the amount of copolymer increased; T_{m2} could not be clearly detected in blends A5 because it overlapped with the glass transition temperature of PC: the melting point of the secondary crystals, T_{m2}, increased while that of the primary crystals, T_{m3}, decreased as the amount of copolymer increased. This relationship indicates that the crystalline structures of the primary crystals thinned and became less perfect while those of the secondary crystals thickened as the amount of copolymer increased. The melting points of the primary and secondary crystals often move in opposite directions.[29]

The crystallization of the polymers is also affected by the size of the dispersed domain. Tol et al. reported a homogeneous nucleation process for a PS/Styrene-maleic anhydride (SMA)/Polyamide (PA6) blend in submicron dispersed PA6 domains.[30] The imperfect crystals had a very low melting temperature compared with the primary and secondary crystals. In samples A5, B0, B1 and B5, the dispersed PET domain size was less than 500 nm (Figure 5.4-a). Therefore, the nucleation induced in the PET domains tended to be homogeneous because the size was too small for crystals to exist. The corresponding peak was then denoted T_{m1}, as shown in the enlarged section in Figure 5.5. The total crystallinity was calculated from the enthalpy of the primary crystals (ΔH_3), the enthalpy of the secondary crystals (ΔH_2) and the enthalpy of the crystals induced by the homogeneous nucleation in the submicron dispersed PET domains (ΔH_1). The total crystallinity decreased from 29% to 7.8% in the 30/70 blend ratio PET/PC and from 26% to 9.4% in 10/90 blend ratio PET/PC.

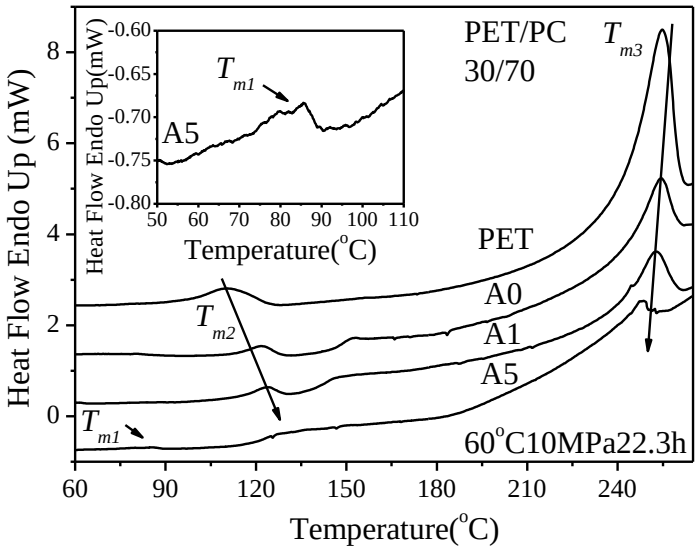

Figure 5.5 DSC heat curves of the neat PET and the PET/PC 30/70 wt% blends (A0, A1 and A5) after CO_2-annealing at 60°C 10 MPa for 22.3 h

Table 5.4 Thermal properties of the neat PET and PET/PC blends after CO_2-annealing at 60°C 10 MPa for 22.3 h

Sample ID.		T_{m1}(°C)	ΔH_1(J/g)	T_{m2}(°C)	ΔH_2(J/g)	T_{m3}(°C)	ΔH_3(J/g)	ΔH_{total}(J/g)	Crystallinity(%)
PET		-	-	112.5	4.07	254.7	46.1	50.2	36%
PET/PC 30/70	**A0**	-	-	122.6	1.11	254.9	10.2	11.3	29%
	A1	-	-	123.9	1.29	252.9	8.74	10.0	27%
	A5	86.1	0.10	-	-	249.1	2.17	2.27	7.8%
PET/PC 10/90	**B0**	83.4	0.24	120.7	0.17	252.4	2.60	2.84	26%
	B1	84.6	0.16	120.6	0.13	242.4	0.73	1.02	10%
	B5	-[a]	-[a]	-[a]	-[a]	241.8	0.44	0.44	9.4%

a – too small to be observed;

The master curves of the PC and PET/PC blends with a 30/70 wt% blend ratio are shown in Figure 5.6. The viscoelastic modulus of all samples originated in the glassy

zone (G'>10^8 Pa), moved from the transition zone to the plateau zone (10^7 Pa>G'>10^6 Pa) and finally reached the terminal zone (G'<10^5 Pa). When the samples were foamed at either 80, 120 and 150°C, they were mostly in the rubbery state, in which the polymer chains could move to create voids and the elasticity of the polymer matrix could still maintain its shape. As shown in Figure 5.6, the elasticity of PC was higher than that of the PET/PC blends over the entire frequency range. As the heat-annealing time increased, the amount of the PET segments that infused the PC matrix increased and the elasticity of the PET/PC blends decreased. Furthermore, the T_g of PC decreased, along with the elasticity and viscosity of the PC matrix.

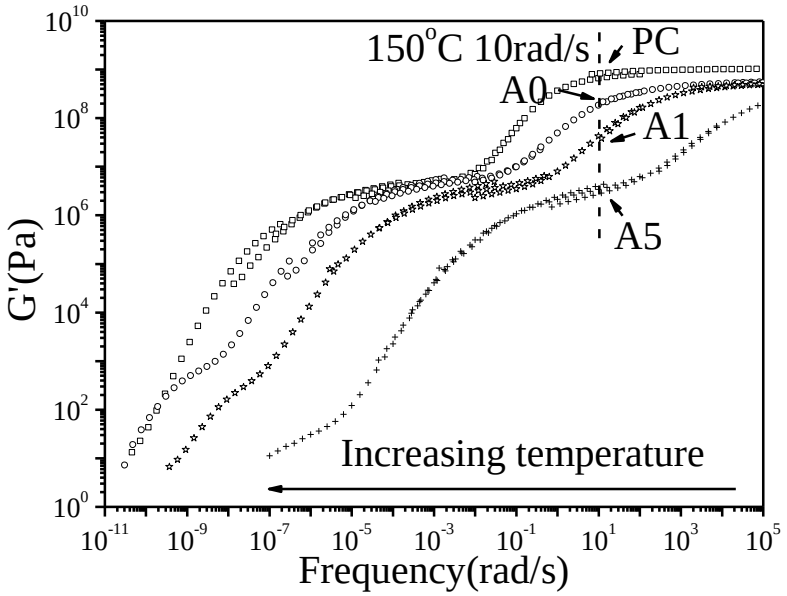

Figure 5.6 Master curves of the G' of PC and PET/PC 30/70 wt% blends (A0, A1 and A5) at 150°C

Figure 5.7 shows the uniaxial extensional viscosity of the PC and the PET/PC blends (A0, A1 and A5). The viscosity measurements were conducted at four different

constant strain rates, 0.1, 0.2, 0.5 and 1.0 s^{-1}, at 240°C for all samples, except for blend A5. Blend A5 was measured at 220°C to prevent it from sagging during the measurement. None of the samples showed any strain hardening behavior.

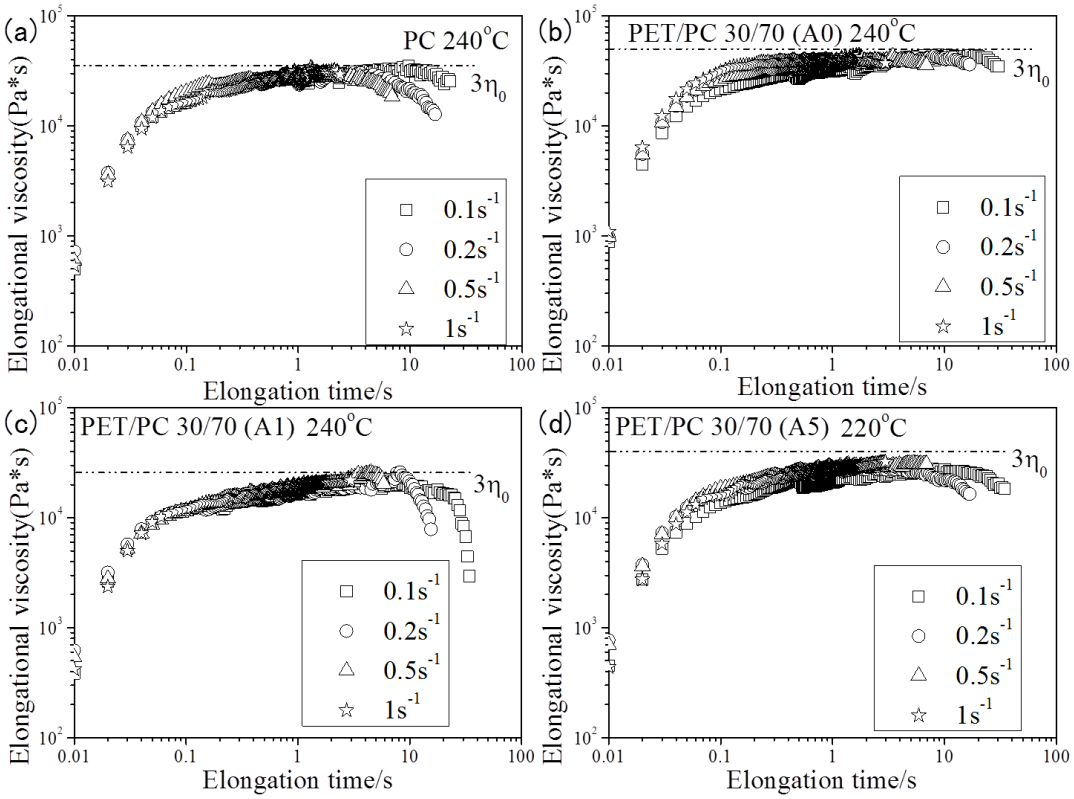

Figure 5.7 Uniaxial elongational viscosity of PC and PET/PC 30/70 wt% blends (A0, A1) at 240°C and the PET/PC 30/70 wt% blend (A5) at 220°C at different constant strain rates. Dashed lines represent the value of three times the zero shear viscosity.

5.4.2 Cell morphology of foamed blends

After dissolving CO_2 into the samples at 10 MPa and 60°C for 22.3 h, the samples were foamed at three different temperatures, 80, 120 and 150°C. Under these foaming conditions, bubble nucleation occurred only in PC and not in the PET domain due to the

presence of crystals. However, the PET domains could serve as the bubble nucleating agents. Figure 5.8 shows the SEM micrographs of the foamed PET/PC blends (A0-A5). The higher magnification SEM micrographs are also shown in Figure 5.9. Because of the space limitation, the SEM micrographs of the blends B0, B1 and B5 are not presented here. Blend B0 had similar foam morphology with blend A1. Blends B1 and B5 had similar cell morphology with blend A5. All foams showed a spherical cell geometry. As the foaming temperature increased, the cells impinged on each other and the cell wall thickness was reduced. The higher magnification SEM images in Figure 5.9 show that the foam of blend A0, which had the largest interfacial tension, showed smooth cell walls. The PET domain seems to function as a bubble nucleating agent, and bubble nucleation occurred at the weak interface between the PET and PC. The foams of blend A1 and B0, which had the reduced interfacial tension and PET crystallinity, showed a fibril-like structure around the PET domains. The lowered interfacial tension and the infusion of copolymer into PET and PC increased the bonding force between PET and PC. The bonding force then stretched the crystal lamellas in the PET domains to form the fibril-like structure. Further increasing the heat-annealing further decreased the interfacial tension. Moreover, the crystallinity of the PET domains also decreased. Therefore, the degree of fibrillation decreased, as shown in the micrograph of foamed blends A5, B1 and B5. Therefore, blends A1 and B0 showed a higher degree of fibrillation than blends A5, B1 and B5, in which the PET domains had a much lower crystallinity. These findings indicated that the fibril-like structure was generated by stretching the crystalline lamellas in the PET domains in the presence of bonding forces between PET and PC.

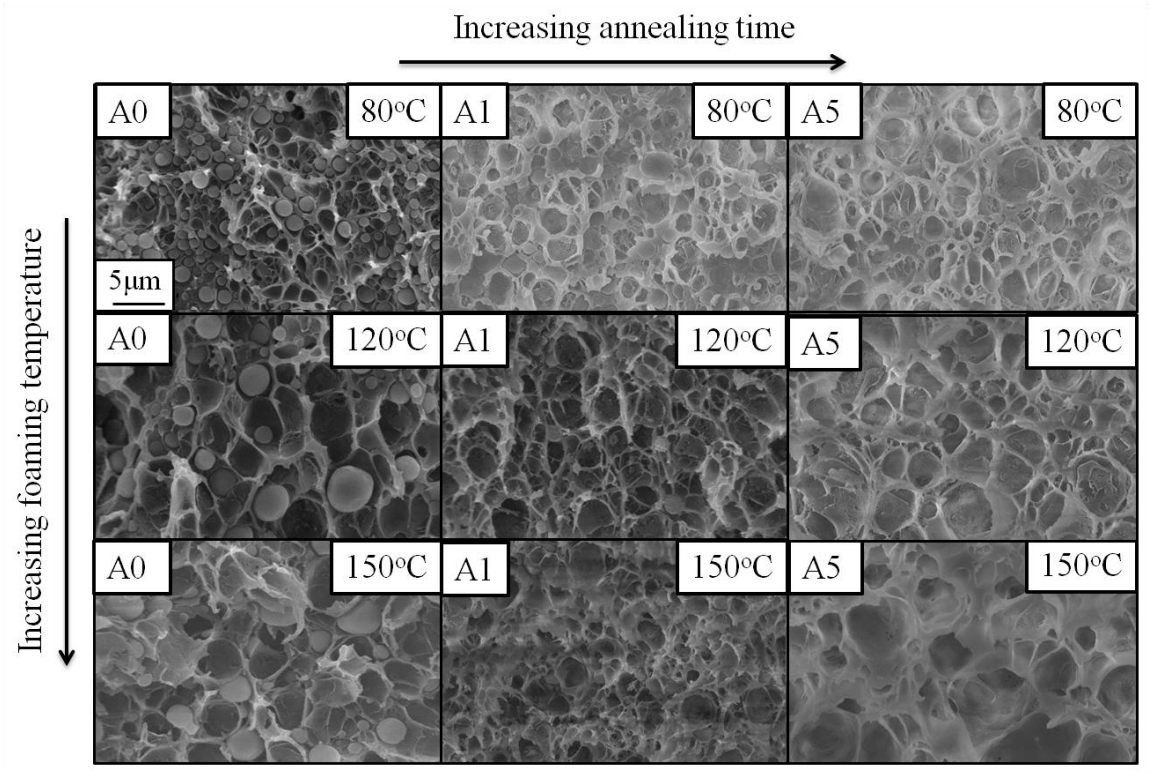

Figure 5.8 SEM micrographs of PET/PC 30/70 wt% blends (A0, A1 and A5) foamed at 80, 120 and 150°C (Magnification × 3000)

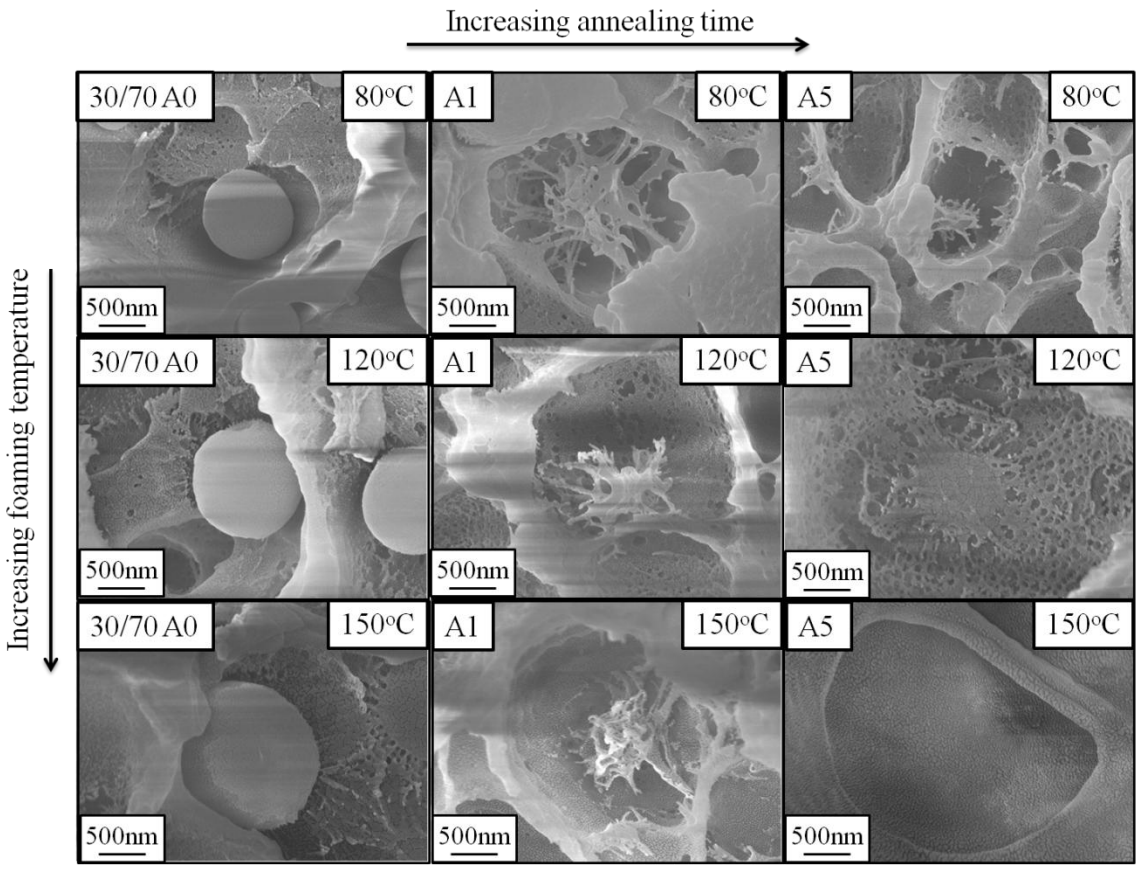

Figure 5.9 SEM micrographs of PET/PC 30/70 wt% blends (A0, A1 and A5) foamed at 80, 120 and 150°C (Magnification × 30000)

The cell density and the cell size were measured from the SEM micrograph, and the results are illustrated in Figure 5.10. The cell density of blends A0, A5, B1 and B5 decreased as the foaming temperature increased, as shown in Figure 5.10. Only blends A1 and B0, which showed a highly fibrillar cell morphology, showed an increase in the cell density as the foaming temperature increased. A higher foaming temperature led to a larger degree of supersaturation and increased the cell density per unit volume of the solid polymer. The decreased cell density for blends A0, A5, B1 and B5 could be attributed to cell coalescence that resulted from a decrease in the viscosity at high

foaming temperatures. The increase in the cell density for blends A1 and B0 was not induced by the suppression of cell coalescence because neither blend showed strain hardening behavior. However, this increase could be related to the formation of fibril-like structures. The bubble nucleation mechanism in blends A1 and B0 could likely differ from that of blends A0, A5, B1 and B5. This difference might be related to the stretch-induced void formation in crystalline polymers.

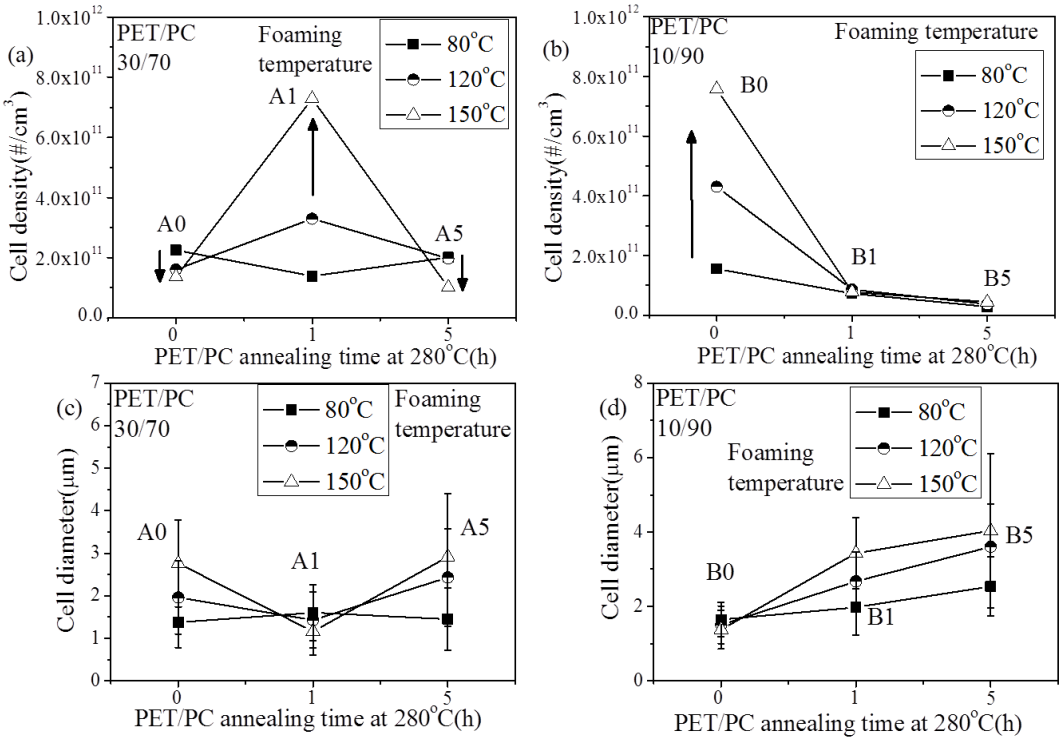

Figure 5.10 Cell density, (a) and (b), and cell size, (c) and (d), of the blends foamed at 80, 120 and 150°C

The open-cell content (volume fraction of open cells in the polymeric foam) of all foamed samples was measured. The open-cell ratio (volume ratio of open cells to total

cells) and cell wall thickness were then calculated using Eqs. (6) and (7). The results are presented in Figure 5.11 and Figure 5.12. Increasing the foaming temperature increased the expansion ratio. This increase, in turn, increased the open-cell content of most of the foams. Nevertheless, blends A1 and A5 shrank when they were foamed at 150°C because the foaming temperature was much higher than the glass transition temperature of the matrix polymer PC. Thus, their expansion ratio was not increased with the increase in the foaming temperature, which also prevented the open-cell content from increasing. Figure 5.12 also shows that the open-cell ratio increased monotonously as the cell wall thinned. The PET/PC 10/90 wt% blend performed better overall with respect to the cell density, cell size and open-cell content as shown in Table 5.5. The fibril-structure of blend B0 could provide the high open-cell content with the low expansion ratio.

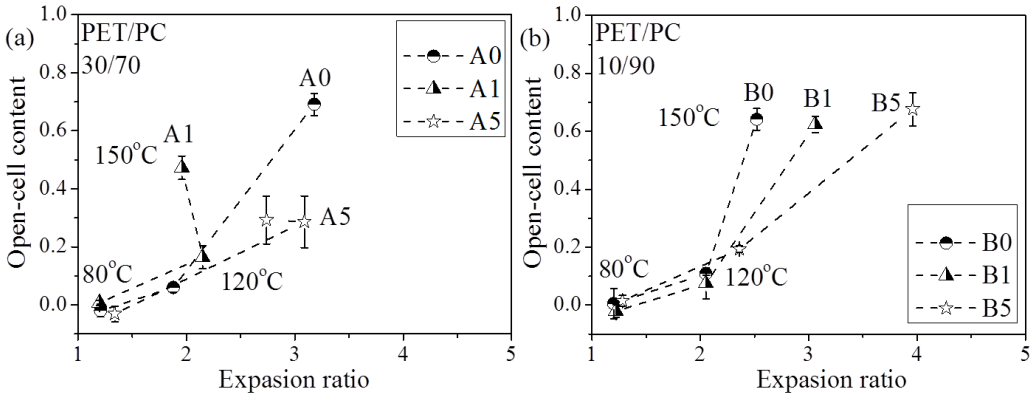

Figure 5.11 Open-cell content of PET/PC 30/70 wt% (a) and PET/PC 10/90 wt% (b) blends as a function of expansion ratio

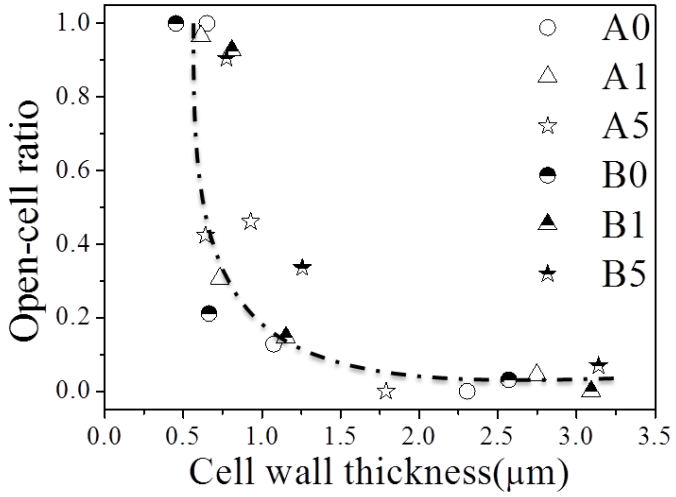

Figure 5.12 Open-cell ratio as a function of cell wall thickness

Table 5.5 Blend and foam properties of PC and PET/PC blends

Sample ID.		*Interfacial tension(mN/m)*	Crystallinity (%)	Cell density (#/cm^3)	Cell size (μm)	Open-cell content (%)
PET/PC 30/70	A0	2.3	29%	1.37E11	2.76	69.1%
	A1	0.647	27%	7.28E11	1.16	47.3%
	A5	0.01	7.8%	1.02E11	2.92	29.3%
PET/PC 10/90	B0	***1.1***	***26%***	***7.58E11***	***1.38***	***64.1%***
	B1	0.21	10%	7.8E10	3.43	62.3%
	B5	0.008	9.4%	4.5E10	4.03	67.6%
PC		-	-	1.81E11	2.74	77.3%

5.5 Conclusions

In this study, we reported a novel method for controlling the foam morphology of open-cell foams by forming fibril-like structures around the PET domains. Heat annealing was a critical process for modifying the interfacial properties by forming a copolymer at the interface between the PET and PC phases. The interfacial tension decreased, the affinity between PET and PC increased, and the crystallinity of the PET domains decreased as the amount of copolymer increased. When the interfacial affinity was strong, a fibril-like structure formed during CO_2 foaming by stretching the crystalline lamellas in the PET domains. The degree of fibrillation was a function of the crystallinity of the PET domains. When the heat-annealing procedure was optimized to generate a large degree of fibrillation during CO_2 foaming, PET/PC blend foams with a large cell density (7×10^{11} # cm^{-3}), a small cell size (less than 2 μm) and 100% open cells were generated.

5.6 References

1. Ruckdaschel, H.; Gutmann, P.; Altstadt, V.; Schmalz, H.; Muller, A.H.E. *Adv. Polym. Sci.* **2010**, 227, 199-252.

2. Klempner, D.; Frisch, K.C. Handbook of Polymeric Foams and Foam Technology. **1991,** Oxford University Press.

3. Mantovani, M.; Gastagnetti, C.; Godano, P.P.; Yamaguchi, H. Multifunctional sound attenuation underbody kit for automobile exterior. JP 4279624.

4. Wong, D.T.; Mullin, S.A.; Battaglia, V.S.; Balsara, N.P. *J. Membr. Sci.* **2012**, 394-395, 175-183.

5. Liao, X.; Zhang, H.; He, T. *J. Nanomater*. **2012**, 1-12.

6. Lee, P.C.; Li, G.; Lee, J.W.S.; Park, C.B. *J. Cell. Plast.* **2007**, 43, 431-444.

7. Lee, P.C.; Naguib, H.E.; Park, C.B.; Wang, J. *Polym. Eng. Sci.* **2005**, 45, 1445-1451.

8. Kohlhoff, D.; Ohshima, M. *Macromol. Mater. Eng.* **2011**, 296, 770-777.

9. Lee, P.C.; Wang, J.; Park, C.B. *Ind. Eng. Chem. Res.* **2006**, 45, 175-181.

10. Park, C.B.; Padareva, V.; Lee, P.C.; Naguib, H.E. *J. Polym. Eng.* **2005**, 25, 239-260.

11. Miyamoto, R.; Fukumori, M.; Shikuma, H.; Ohshima, M. *Proceeding of the Polymer Processing Society 28th Annual Meeting in Thailand*, **2012**.

12. Krause, B.; Boerrigter, M.E.; van der Vegt, N.F.A.; Strathmann, H.; Wessling, M. *J. Membr. Sci.* **2001**, 187, 181-192.

13. Krause, B.; Sijbesma, H.J.P.; Münüklü, P.; van der Vegt, N.F.A.; Wessling, M. *Macromolecules*. **2001**, 34, 8792-8801.

14. Krause, B.; Diekmann, K.; van der Vegt, N.F.A.; Wessling, M. *Macromolecules*. **2002**, 35, 1738-1745.

15. Li, Y.; Yao, Z.; Chen, Z.; Cao, K.; Qiu, S.; Zhu, F.; Zeng, C.; Huang, Z. *Chem. Eng. Sci.* **2011**, 66, 3656-3665.

16. Zhai, W.; Wang, H.; Yu, J.; Dong, J.; He, J. *Polym. Eng. Sci.* **2008**, 48, 1312-1321.

17. Liao, Q.; Tsui, A.; Billington, S.; Frank, C.W. *Polym. Eng. Sci.* **2012**, 52, 1495-1508.

18. Zhai, W.; Wang, J.; Chen, N.; Naguib, H.E.; Park, C.B. *Polym. Eng. Sci.* **2012**, 52, 2078-2089.

19. Kumar, C.A.; Krishnamurthy, J. *Polym. Eng. Sci.* **2011**, 51, 1749-1756.

20. Spitael, P.; Macosko, C.W. *Polym. Eng. Sci.* **2004**, 44, 2090-2100.

21. Suzuki, T.; Tanaka, H.; Nishi, T. *Polymer*. **1989**, 30, 1287-1297.

22. Zhang, Z.; Xie, Y.; Ma, D. *Eur. Polym. J.* **2001**, 37, 1961-1966.

23. Fiorini, M.; Pilati, F.; Berti, C.; Toselli, M.; Ignatov, V. *Polymer*. **1997**, 38, 413-419.

24. Park, C.B.; Lee, P.C.; Wang, J.; Padareva, V. *Cell. Polym.* **2006**, 25, 1-18.

25. Porter, R.S.; Wang, L.H. *Polymer.* **1992**, 33, 2019-2030.

26. Marin, N.; Favis, B.D. *Polymer*. **2002**, 43, 4723-4731.

27. The Society of Polymer Science. *Kisokoubunnshikagaku.* **2006**, Tokyo-Kagaku-Dojin Press.

28. Kim, W.N.; Burns, C.M. *Macromolecules.* **1987**, 20, 1876-1882.

29. Wang, Z.G.; Hsiao, B.S.; Sauer, B.B.; Kampert, W.G. *Polymer.* **1999**, 40, 4615-4627.

30. Tol, R.T.; Mathot, V.B.F.; Groeninckx, G. *Polymer.* **2005**, 46, 2955-2965.

Chapter 6

GENERAL CONCLUSION

The specific applications of polymeric foams depend on the foam properties, like cell density, cell size, open- and/or closed cell, etc. Three basic foaming processes, i.e., bubble nucleation, bubble growth and cell coalescence, are the bridges which connect a variety of blend properties with versatile foam properties. The construction of such kinds of bridges is of great importance to the fundamentals of polymer blend foaming. Even though a large number of researchers have done great amount of works concerning the foaming behavior of polymer blends, it was mainly focused on the dispersion of second phase polymer (interfacial area). Foaming behavior at the interface has also been studied by foaming polymer/inorganic additive composites as well. However, not until the ideas of locating bubble nucleation in dispersed domains (to obtain nanocell foams), inducing bubble nucleation in both domains and matrix (to obtain bimodal cell foams) or debonding domains from the matrix in the cell wall in the process of bubble growth (to obtain open-cell foams), the advancement of polymer blends on controlling foam properties have been realized. Among those ideas, the interfacial properties, like interfacial area, interfacial tension, interfacial adhesion, etc. play vital roles in the foaming processes of bubble nucleation, bubble growth and cell coalescence. The works introduced above explained the foaming behavior from the macroscopic point of view. As for the microscopic point of view, it is still unclear how bubble nucleation and bubble growth occur at the interface. Therefore, this work aims to understand the detailed effects of interfacial properties on foaming processes, and provides an insight into

macromolecular chain movements at the interface during bubble nucleation and bubble growth. In order to present this work in clarity and simplicity, this thesis is divided into two parts: first part describes the fundamentals of bubble nucleation and bubble growth at the interface and the contents are as follows:

Chapter 2: Bubble nucleation at the interface of PMMA/PC and PMMA/PP blends.

Chapter 3: Bubble growth at the interface of PET/PC blends.

Second part utilizes the knowledge obtained above to produce desirable open-cell foams and the contents are as follows:

Chapter 4: Open-cell PC foam.

Chapter 5: Open-cell PET/PC blend foams

6.1 Bubble nucleation at the interface of PMMA/PC and PMMA/PP blends

In chapter 2, two amorphous polymers, PMMA and PC were selected to study the effect of interfacial properties on bubble nucleation; because crystalline structure would induce heterogeneous bubble nucleation at the interface between lamellas and amorphous regions as well. PC with larger elasticity was selected as domain while PMMA with lower elasticity was selected as matrix, so that the bubble nucleation would only occur at the interface between PMMA and PC. As for PMMA/PP blends where PP was domain and PMMA was matrix, even though PP was semicrystalline polymer, the incompatible characteristic of PMMA/PP blends implied very weak influence of PP crystalline on interfacial properties. The interfacial properties of PMMA/PC blends were then precisely controlled by reactive blending, during which graft copolymers were generated at the interface. Consequently, the PMMA/PC blend properties were changed by those copolymers: the dispersion of PC domains was facilitated and the interfacial area increased, as shown in Figure 6.1 (a). However, the interfacial tension between PC domains and PMMA matrix decreased with increasing the amount of copolymers. Hence, the effectiveness of heterogeneous bubble nucleation at the interface also decreased with increasing the amount of copolymers, as shown in Figure 6.1 (b).

Since heterogeneous bubble nucleation is a function of interfacial area, the schematic graph of heterogeneous bubble nucleation efficiency is also illustrated in Figure 6.2. At higher interfacial tension, i.e., PMMA/PP blend, the nucleation ability per unit interfacial area was larger. Along with decreasing interfacial tension with the addition of copolymer to PMMA/PC blend, the heterogeneity decreased and nucleation

ability per unit interfacial area decreased correspondingly. In the end, it is noted that if the increase of interfacial area can not compensate the loss of heterogeneity, cell density will decrease with decreasing interfacial tension.

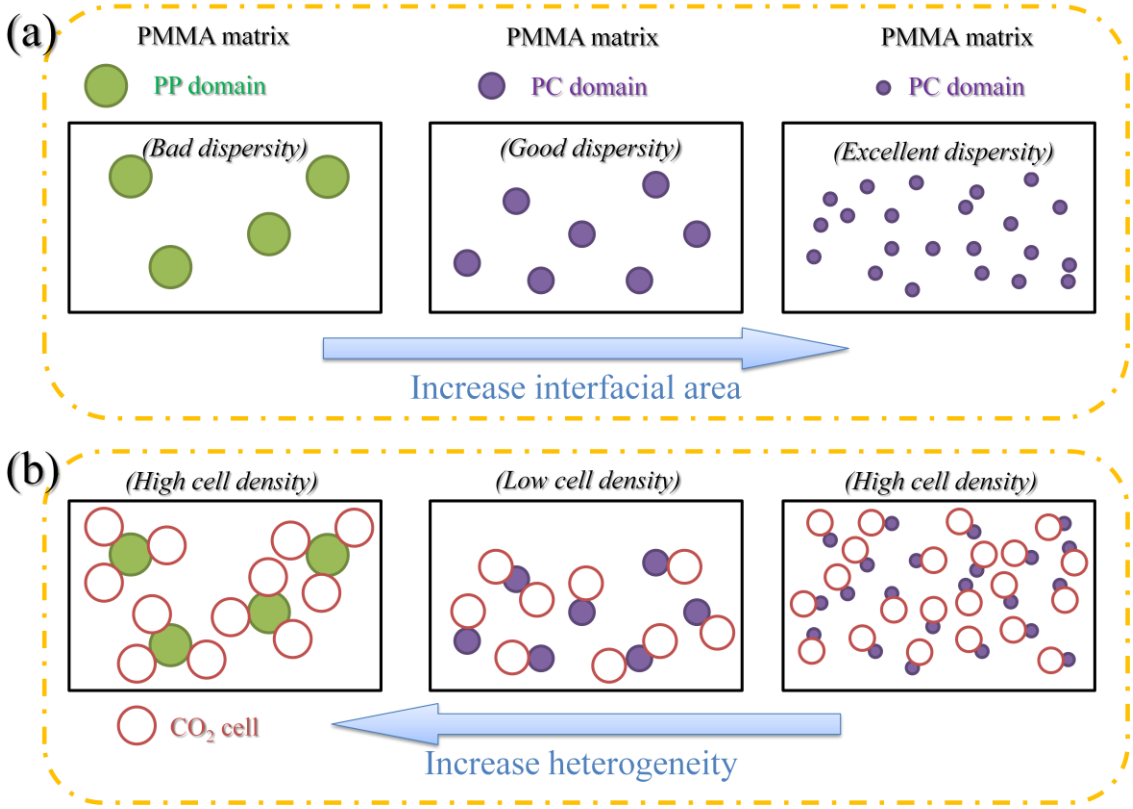

Figure 6.1 Schematic graphs of blend morphology and foam morphology

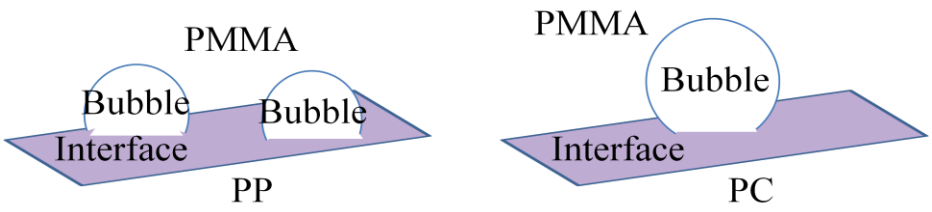

Figure 6.2 Schematic graph of bubble nucleation at the interface

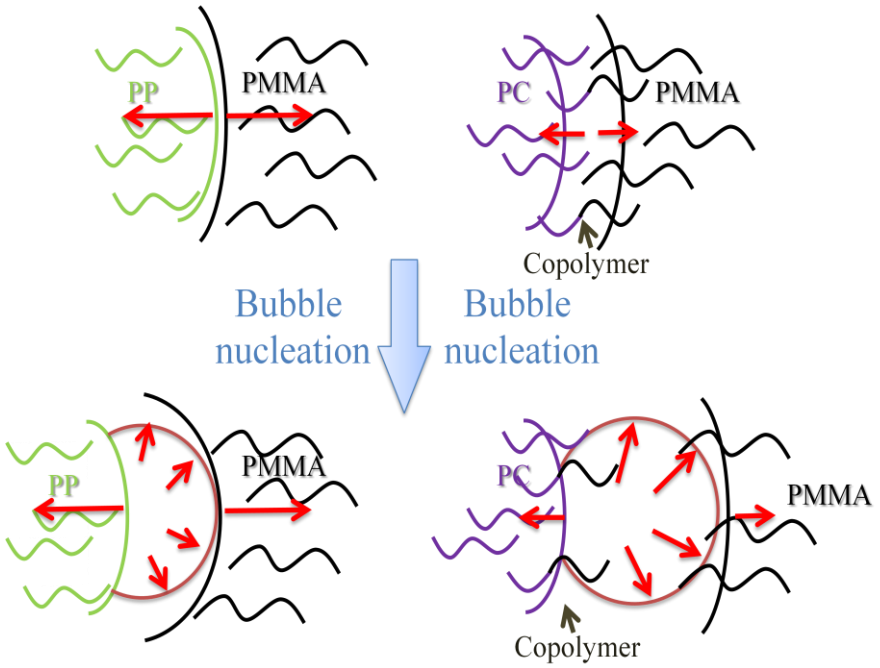

Figure 6.3 Schematic graph of bubble nucleation at the interface (microscopic view)

Figure 6.3 illustrates the heterogeneous bubble nucleation at the interface of polymer blends from the microscopic point of view. It is noted that the PMMA or PP molecular chains tend to gather with their own molecular chains, and therefore a pressure gradient is generated at the interface. Furthermore, the incompatible PMMA/PP blend had very large interfacial tension, which means very large pressure (force field) gradient perpendicular to the interfacial boundary. When the bubble nucleation occurred at the interface, this pressure gradient effectively lowered the energy required for bubble nucleation. In contrast, PMMA/PC blends with very small pressure gradient required more energy for bubble nucleation. Therefore, the energy barrier for bubble nucleation in PMMA/PC blends is much larger than PMMA/PP blend.

6.2 Bubble growth at the interface of PET/PC blends

Normally, the thickness of interface is less than 0.1 μm, hence it is very difficult to observe the effect of interfacial properties on bubble growth in the system of amorphous polymer blend. As for semicrystalline polymer, the length of lamellas can be as large as 3 μm, which is comparable to cell size. Therefore, in chapter 3, PET/PC blends were prepared to investigate the effect of interfacial properties on bubble growth at the interface. Semicrystalline PET was used as domain and amorphous PC was used as matrix. (The matrix polymer has to be amorphous, otherwise the crystalline structure will significant affect bubble nucleation and bubble growth which results in complicate foaming behavior). Mixing PET with PC at 270°C only led to incompatible blend. In order to increase the interfacial adhesion, annealing was conducted to generate block copolymer at the interface between PET domains and PC matrix. When incompatible PET/PC blend was foamed by CO_2, the weak interfacial adhesion led to smooth surface of PET domains. However, the compatible PET/PC blend foams had either PET domain with rough surface or tightly packed interface after CO_2 foaming. Higher magnification SEM micrographs of PET/PC 10/90 blend foams show fibrils at submicron scale, because the strong bonding force, i.e., large interfacial adhesion, stretched the lamellas in PET domains to form the fibril structure, as shown in Figure 6.4.

Due to the existence of crystalline phase, PET domain was not foamed. However, the amorphous phase in PET domain was plasticized by CO_2. After bubble nucleation, two factors (interfacial adhesion and plasticization) cooperated to stretch lamellas in PET domains. We have to keep in mind that the fibril structure was mainly formed during bubble growth, but not bubble nucleation; because the existence of crystalline structure

would significantly weaken the degree of fluctuation of CO_2 concentration and correspondingly lead to less bubble nucleation if fibril structure were involved in bubble nucleation (CO_2 cannot dissolve in semicrystalline phase).

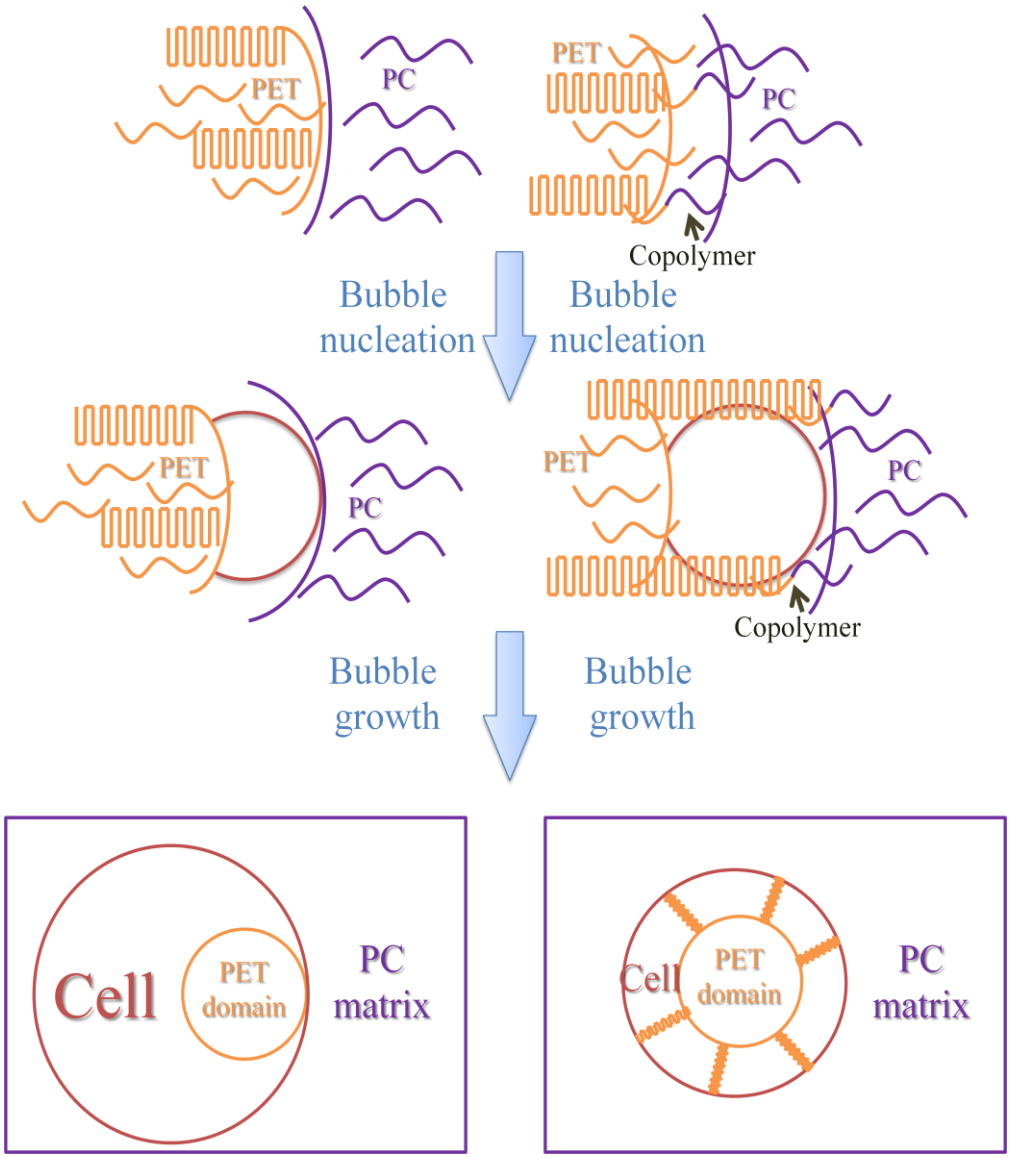

Figure 6.4 Schematic graph of bubble growth at the interface

6.3 Open-cell PC and PET/PC blend foams

When PC matrix was foamed by CO_2, the biaxial elongational flow induced dilatational deformation and then nanoporous structure emerged on the cell wall, as shown in Figure 6.5. After bubble nucleation, the molecular chains on the cell wall began to orient in the direction of biaxial elongational flow. Along with molecular chain alignment, lateral force was formed and subsequently cavitation occurred. Larger expansion ratio and faster bubble growth rate induced to larger degree of chain orientation, and hence larger nanopore density on the cell wall. In contrast, higher environmental temperature led to larger degree of chain relaxation, and hence smaller nanopore density on the cell wall. Moreover, with the addition of acetone as crazing agent, the formation of nanoporous structure was facilitated due to larger expansion ratio and smaller surface tension. With increasing expansion ratio further, the cell wall thickness decreased and subsequently nanoporous structure on the cell wall attributed to open-cell foams.

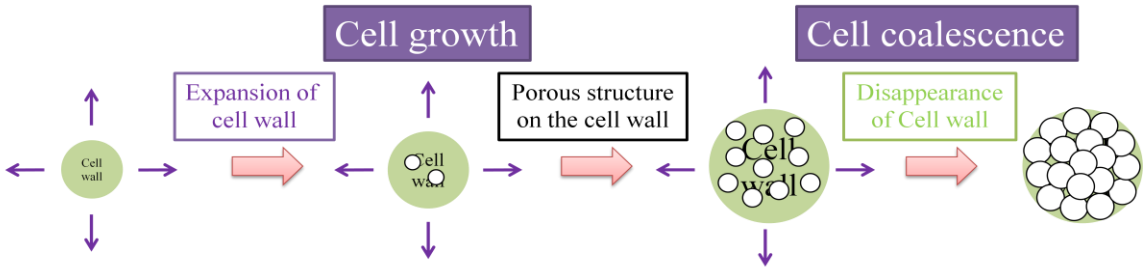

Figure 6.5 Schematic graph of the structure on the cell wall

In order to obtain 100% open-cell ratio PC foam, large expansion ratio was required to reduce the cell wall thickness; because cell size was large. The relationship

among cell wall thickness, expansion ratio and cell size was clearly expressed by equation (7) in chapter 5. Hence, heterogeneous bubble nucleation could be utilized to obtain open-cell foams with large cell density, small cell size and 100% open-cell ratio. However, the nanoporous structure on the cell wall not only opens the cell walls, but also induces cell coalescence, as shown in Figure 6.5. Consequently, open-cell foam made by incompatible PET/PC blend had large cell size and small cell density; because the effect of heterogeneous bubble nucleation was neutralized by cell coalescence.

Therefore, the strategy of modifying interfacial properties is utilized. By adding copolymer, the amount of PET molecules dissolved in PC matrix increased, and hence the elasticity and viscosity of PC matrix decreased which facilitated the cavitation on the cell wall. At the same time, the increase of interfacial adhesion led to large degree of fibrillation by stretching crystalline lamellas in PET domains, which further enhanced bubble nucleation. Since the fibril structure was related with interfacial adhesion and lamellas in PET domains, amorphous polymer blend foams, like PMMA/PC, did not show any fibril structure even if they had strong interfacial adhesion. Meanwhile, the copolymers hindered the crystallization behavior in PET domains due to different chemical compositions. When the interfacial adhesion was strengthened by copolymers, the crystallinity of PET domains decreased. As a result, there was an optimum point where both interfacial adhesion and crystallinity were just adequate to form large degree of fibrillation, and hence to obtain the open-cell foams with large cell density and small cell size.

6.4 Conclusions

In this dissertation, the bubble nucleation and bubble growth at the interface of polymer blends were discussed. The copolymers generated at the interface facilitated the domain dispersion, decreased the interfacial tension and increased the interfacial adhesion. In the case of PET/PC blends, the copolymers also suppressed the crystallization behavior. The effects of interfacial properties on foaming processes are as follows:

(1) Heterogeneous bubble nucleation was favored by large interfacial area, but was impeded by small interfacial tension;

(2) Fibril structure between semicrystalline PET domains and PC matrix, which was formed in the process of bubble growth, was favored by strong interfacial adhesion and large crystallinity in PET domains;

Afterwards, both the heterogeneous bubble nucleation and fibrillation were utilized to enhance the bubble nucleation, so that open-cell foams of PET/PC blend with large cell density and small cell size could be obtained.

The open-cell foams with microcells and nanopores can absorb sound at low frequencies. This characteristic is superior to many other sound attenuation materials which can only block noise at high frequencies. The performance of sound attenuation of open-cell foams with microcells and nanopores is related with the foam morphology, like cell size, cell density, open-cell content, nanopore size, nanopore density, cell wall thickness, etc. How the microcell and nanopore morphology affect the sound attenuation can be an extending research, while the results in this dissertation can be utilized to obtain the desired open-cell foams.

LIST OF FIGURES

LIST OF FIGURES

LIST OF FIGURES

LIST OF FIGURES

LIST OF FIGURES

LIST OF FIGURES

LIST OF TABLES

ACKNOWLEDGEMENT

I would like express my very great appreciation to Professor Masahiro Ohshima at the Department of Chemical Engineering at Kyoto University. As an advisor, his mentorship and patient guidance have done me a great favor to finish this dissertation. As a scholar, his broad knowledge and positive scientific attitude has inspired me all the time during my Ph.D. study.

Furthermore, I would like to offer my special thanks to Dr. Shinsuke Nagamine, Associate Professor at Kyoto University and Dr. Kentaro Taki, Associate Professor at Yamagata University for their constructive advices and comments regarding on my experiments. Particularly, the assistance provided by Dr. Kentaro Taki was greatly appreciated; the research progress would not have been so well without his kind help.

In addition, I would like to thank Mr. Haruo Shikuma for his technical support of rheological test. The help provided by Ms. Maki Yamamoto was highly appreciated for enabling me to enjoy the life in Japan. I also wish to acknowledge the valuable friendship with Mr. Siwach Tengsuwan. The financial support provided by the Ministry of Education, Culture, Sports, Science &Technology (MEXT, Japan) was appreciated as well.

Moreover, my special thanks are extended to all the students who have graduated or are still studying at the Laboratory of Material Processing Engineering for their kind help to my work.

Last but not least, I wish to thank my parents and wife for their support and encouragement throughout my study.

LIST OF PUBLICATIONS

Chapter 2

Gong, P.; Ohshima, M. Effect of Interfacial Tension on the Cell Structure of Poly(methyl methacrylate)/Bisphenol A Polycarbonate Blends Foamed with CO_2, *Journal of Applied Polymer Science*, **2013**, accepted.

Chapter 3

Gong, P.; Ohshima, M. The Effect of Interfacial Miscibility on the Cell Morphology of Polyethylene Terephthalate/Bisphenol A Polycarbonate Blend Foams, *Journal of Polymer Science, Part B: Polymer Physics*, **2012**, 50, 1173-1180.

Chapter 4

Gong, P.; Ohshima, M. Nanoporous Structure on the Cell Wall of Polycarbonate Foams, submitted.

Chapter 5

Gong, P.; Ohshima, M. Open-cell Foams of Polyethylene Terephthalate/Bisphenol A Polycarbonate Blend, submitted.

LIST OF PUBLICATIONS

International Conferences

Gong, P.; Ohshima, M. Open-cell Polyethylene Terephthalate/Bisphenol A Polycarbonate Blend Foams, *Smart System Engineering 2013*, Yonezawa, Japan, Invited Speaker.

Gong, P.; Ohshima, M. The Effect of Blend Morphology and Interfacial Tension on Cell Structure of Physical Foaming with CO_2 of Polymer Blends, SPE's *FOAMS 2012*, Barcelona, Spain, Oral Presentation.

Gong, P.; Ohshima, M. Effect of Interfacial Tension on Poly(methyl methacrylate)/Bisphenol A Polycarbonate Blend Morphology and Foam Morphology, *Asian Workshop on Polymer Processing 2012*, Kyoto, Japan, Poster.

Gong, P.; Ohshima, M. Effect of Transesterification at Interface between Bisphenol A Polycarbonate and Polyethylene Terephthalate Domains on Micro/Nano Cellular Foam of their Blends, SPE's *FOAMS 2011*, New Jersey, USA, Oral Presentation and Poster.